EFFECT OF HEAT AND PLASMA TREATMENTS ON THE ELECTRICAL AND OPTICAL PROPERTIES OF COLLOIDAL INDIUM TIN OXIDE FILMS

A Dissertation
Presented to
The Academic Faculty

by
Salil Mohan Joshi

In Partial Fulfillment of the Requirements for the
Degree of Doctor of Philosophy in the
School of Materials Science and Engineering

Georgia Institute of Technology
August 2013

EFFECT OF HEAT AND PLASMA TREATMENTS ON THE ELECTRICAL AND OPTICAL PROPERTIES OF COLLOIDAL INDIUM TIN OXIDE FILMS

Approved by:

Dr. Rosario A. Gerhardt, Advisor
School of Materials Science and Engineering
Georgia Institute of Technology

Dr. Yulin Deng
School of Chemical and Biomolecular Engineering
Georgia Institute of Technology

Dr. W. Brent Carter
School of Materials Science and Engineering
Georgia Institute of Technology

Dr. Zhiqun Lin
School of Materials Science and Engineering
Georgia Institute of Technology

Dr. Samuel Graham
School of Materials Science and Engineering
Georgia Institute of Technology

Dr. Ilia Ivanov
Center for Nanophase Materials Sciences
Oak Ridge National Laboratory,
Oak Ridge, TN.

Date Approved: June 11th, 2013

Dedicated to my parents, Mohan Joshi and Pratibha Joshi; and to my wife, Gauri Joshi
for their unconditional love and support

Acknowledgements

First and foremost, I would like to express my appreciation to my advisor, Dr. Rosario Gerhardt for guiding me along my PhD journey. Dr. Gerhardt's guidance, constant encouragement and patience went a long way to helping me develop as a researcher. I would also like to thank Dr. Brent Carter, Dr. Samuel Graham, Dr. Yulin Deng, Dr. Ilia Ivanov and Dr. Zhiqun Lin for serving on my committee.

I am thankful for funding support from the Institute of Paper Science & Technology Alumni Association Scholarship Endowment Fund at Georgia Tech and partial support from the US Department of Energy under DE-FG 02-03-ER 46035. I am also thankful for access to the Nanotechnology Research Center (NRC) at Georgia Tech, Atlanta; as well as the various research facilities at the Oak Ridge National Laboratory, Oak Ridge TN.

I would like to thank Dr. Ilia Ivanov for helping me with optical characterization and spray coating at the Center for Nanophase Materials Sciences (CNMS) at Oak Ridge National Laboratory (ORNL). I would also like to thank Dr. Gregory Book for his help with plasma treatments and XPS characterization. I would also like to thank Dr. Walter Henderson (NRC) and Dr. Brent Carter for their help with XPS characterization and analysis. Thanks to Ms. Yolande Berta and Dr. Yong Ding for help with the TEM and HRTEM. Thanks to Dr. Adam Rondinone at CNMS, ORNL for help with GISAXS characterization. Thanks to Dr. Jie Xu at Georgia Tech Research Institute (GTRI), and Dr. Seth Marder in the School of Chemistry at Georgia Tech, for letting me use their UV-visible spectrophotometers.

I would like to thank Dr. Charlie Capozzi for helping me get started with the non-aqueous synthesis of ITO nanoparticles, Dr. Lex Nunnery for help with FTIR

characterization, Dr. Il Tae Kim and Sarang Deodhar for help with thermogravimetric analysis, Dr. Chunqing Peng for showing me how to use the AFM. I would also like to thank Dr. Charlie Capozzi and Dr. Cantwell Carson for helping locate and get the glove box shell from surplus, as well Dr. Phil Graham for very valuable guidance on how to repair the broken glove box, which was essential for synthesizing the ITO nanoparticles used in this research. Special thanks to Matthew Marchese for his skill with laser machining and unflagging enthusiasm to help me fabricate shadow masks for sputtering. I would also like to thank my past and present research group members – Charlie Capozzi, Chunqing Peng, Cantwell Carson, Siva Kumar Kelekanjeri, Brian Bertram, Ricky Whelchel, Tim Pruyn, Rachel Muhlbauer, Justin Brandt, Ryan Gussenhoven, Abigail Halim, and Waylon Puckett for helping make working in the research group such a fun and enjoyable experience.

I would also like to thank my friends Nivedita Ranade and Nikhil Ganu. You guys were not only awesome to hang out with, I also highly appreciate your help and support from the day I arrived in Atlanta. Last, but not the least, I can never thank my family – Aaee and Anna, Aaee and Baba, and Gauri enough for their unconditional love, support, encouragement and belief in me.

Table of Contents

List of Tables

List of Figures

Summary

The research presented in this dissertation explores the possibility of using colloidal indium tin oxide (ITO) nanoparticle solutions to direct write transparent conducting coatings (TCCs), as an alternative route for TCC fabrication. ITO nanoparticles with narrow size distribution of 5-7 nm were synthesized using a non-aqueous synthesis technique, and fabricated into films using spin coating on substrates made from glass and fused quartz. The as-coated films were very transparent (>95% transmittance), but highly resistive, with sheet resistances around 10^{13} Ω/sq. Pre-annealing plasma treatments were investigated in order to improve the electrical properties while avoiding high temperature treatments. Composite RIE treatment recipes consisting of alternating RIE treatments in O_2 plasma and in Ar plasma were able to reduce the sheet resistance of as spin coated ITO films by 4-5 orders of magnitude, from about 10^{13} Ω/sq in as-coated films to about 3×10^8 Ω/sq without any annealing. Plasma treatment, in combination with annealing treatments were able to decrease the sheet resistance by 8-9 orders of magnitude down to almost 10 kΩ/sq, equivalent to bulk resistivity of ~0.67 Ω.cm. Investigation into effectiveness of various RIE parameters in removing residual organics and in reducing the sheet resistance of colloidal ITO films suggested that while reactive ion annealing (RIE) pressure is an important parameter; parameters like plasma power, number of alternating O_2-Ar RIE cycles were also effective in reducing the residual organic content. Impedance spectroscopy analysis of the colloidal ITO films indicated the dominance of the various interfaces, such as grain boundaries, insulating secondary phases, charge traps, and others in determining the observed electrical properties.

Chapter 1:
Introduction

Electronic flat panel displays are widely used these days. The transparent circuits, which control each pixel in such displays, are very important in making those types of displays function. Panel display circuits are made possible by an important class of materials called transparent conductors. Transparent conductors are also very important in applications such as organic and conventional photovoltaic cells, energy efficient windows, etc. Indium tin oxide is the most widely used transparent conductor. As a result of the increased need for high quality transparent circuits, the demand for indium has skyrocketed in recent years. Due to the scarcity of indium, there is a need for significantly reducing indium waste during the fabrication of transparent circuits. In addition, the growing demand for flexible circuits and displays has made it important to fabricate high quality circuits on flexible and heat sensitive polymer substrates. The development of indium tin oxide nanoparticle-based inks and the understanding of films and circuits fabricated from them can usher in new methods of transparent circuit fabrication, such as inkjet printing, and those based on microcontact printing and nanoimprint lithography. This can lead to not only a lower consumption of indium and but also economical and high quality transparent circuits that can be fabricated on a variety of flexible substrates.

The current methods of deposition of indium tin oxide films involve techniques such as magnetron sputtering, spray pyrolysis and pulsed laser deposition techniques [1, 2]. These methods require substrates to be heated to high temperatures in order to impart coatings with high conductivity. In addition, the underlying line-of sight approach of these techniques makes them inherently not suitable for substrates with complex shapes. Most

flexible substrates are heat sensitive. Widely used flexible substrates such as polyethylene terephthalate (PET), and polyethylene naphthalate (PEN) cannot be used or processed at high temperatures. These melt around 250-260°C, and have usage temperature ratings of 105°C (PET) and 160°C (PEN) [3]. When conventional techniques such as sputtering, pulsed laser deposition are used to deposit ITO at a low temperature, coatings of a much inferior quality are produced, compared to those deposited at a high temperature [2]. A new approach to the production and deposition of transparent circuits is hence needed.

Crystalline colloidal nanoparticles of indium tin oxide can be readily synthesized by an organometallic one-pot technique, using inexpensive metal acetate precursors [4]. Inks made from crystalline TCO nanoparticles can be a good alternative means of achieving transparent conducting circuits. Techniques such as microcontact printing [5], nanoimprint lithography [6, 7] and inkjet printing [8, 9] can be used to print indium tin oxide inks onto a variety of substrates. Hence, it is important to develop a good understanding of how to control the optical and electrical behavior of the colloidal nanoparticles and the films and circuits fabricated from them. It is hoped that the proposed research will pave the way for fabricating inexpensive transparent circuits on a variety of substrates, while at the same time learning how to control the oxygen stoichiometry and resultant properties.

The overall objective of this research is to contribute to the understanding of the microstructural development in colloidal ITO based films, and the effect of heat treatment and other processing conditions on their optical and electrical properties. Indium tin oxide nanoparticles will be synthesized and deposited as films onto glass and fused quartz substrates by spin coating. The films will be subjected to various treatments such as ligand removal and heating in different atmospheres. These treatments can generally be expected

to affect the parameters such as the opto-electronic properties as well as the sintering and adhesion of the films to the substrate.

The organization of this dissertation document is as follows. A brief literature review covering the major concepts related to the work presented in this dissertation is given in chapter 2. Chapter 3 describes the general details about the synthesis of colloidal ITO nanoparticles, the fabrication and basic processing of colloidal ITO films, as well as the characterization techniques used, that were central to this work. Additional experimental details specific to the later chapters are described in the respective chapters. Chapter 4 describes and discusses in detail the synthesis of ITO nanoparticles, fabrication of ITO films, and their characterization. Chapter 5 discusses the effect of annealing at various temperatures and in different atmospheres on the properties of spin coated colloidal ITO films. Chapter 6 discusses the effect of various RIE and plasma treatments on the properties of ITO films, as well as post plasma treatment annealing. Chapter 7 discusses the use of impedance spectroscopy characterization method to help understand the electrical behavior of the colloidal ITO films as-coated, and after processing such as plasma treatment and annealing. Chapter 8 concludes the dissertation, and suggests some possible future ideas that could help take this research forward.

Chapter 2:
Literature Review

2.1 Transparent Conducting Oxides

Transparent conducting oxides (TCOs) are a group of materials that combine the seemingly contradictory properties of close-to-metallic conductivity with almost complete non-metallic transparency [1, 10]. The first report of a TCO was by Badekar in 1907 [11], when he reported that thin films of Cd became transparent on oxidizing, yet continued to be conducting. Since then, TCOs have entered the commercial mainstream in the form of transparent electrodes on flat panel displays and electromagnetic shielding in cathode ray tubes. These materials can also be used for thermal management in buildings such as in window glass coatings for activation of electrochromic coatings and for reflection of IR wavelengths as well as in thin film photovoltaic cells [2]. TCOs can have a range of optical and electrical properties depending on their composition, method of deposition, and any other processing that may have been done on them. A comparison of TCOs in terms of their average optical transmittance and sheet resistance is shown in Fig. 2.1, sourced from Chopra et al. [10]. Among the various TCOs shown in this figure, it can be seen that ITO has the best combination of properties in the form of high transmittance and low sheet resistance. Most TCOs achieve a combination of transparency and close-to-metallic conductivity because while they have a wide band gap which prohibits inter-band transitions in the visible range, intrinsic dopants like oxygen deficiencies or impurity dopants donate electrons to the conduction band (or holes to the valence band) and enhance the conductivity. An effective TCO should have high electrical conductivity combined with low absorption of visible light. The processing and material characteristics of the transparent conductors used in optoelectronic applications should be optimized to

maximize optical transmittance, while achieving minimum electrical resistivity, as needed by the application. Fig. 2.2 shows the general optical and electrical properties required of TCCs for various display applications.

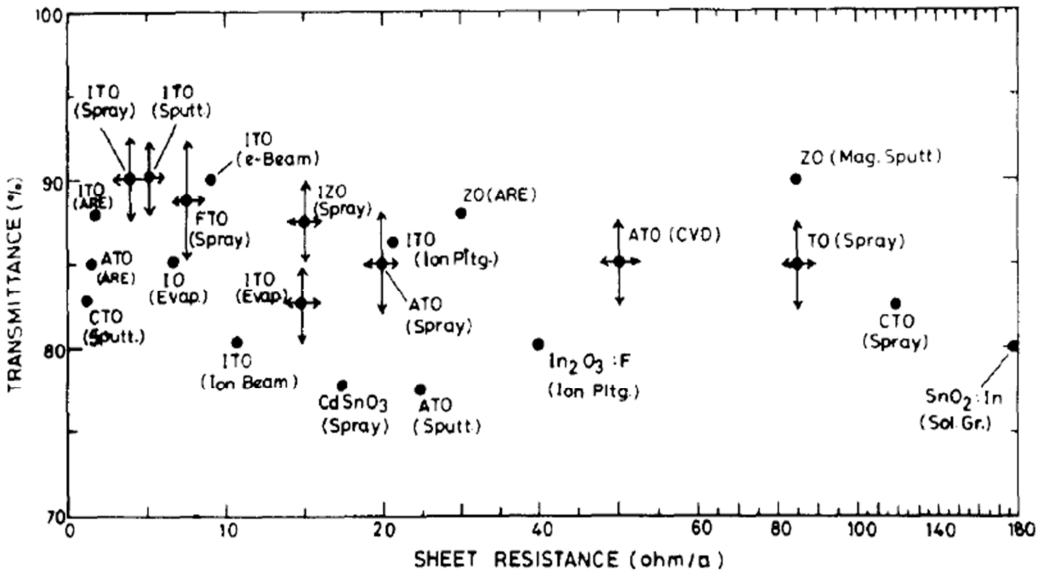

Fig. 2.1 Variation of sheet resistance and optical transmittance for different transparent conducting oxides [10]

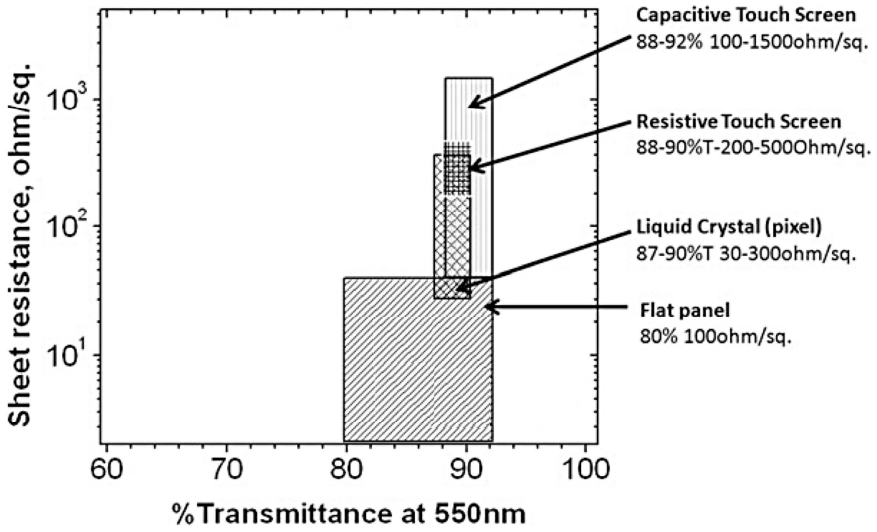

Fig. 2.2: Resistance–transmittance requirements for various display applications of transparent conductive coatings (from [12])

Various figures of merit (FOM) have been proposed to describe the properties of transparent conductive coatings (TCCs). These can often be very specific to an application. They could be expressed as a range of suitable properties or as a single number. Ivanov, et al. have discussed various FOMs applicable to TCCs in detail [12]. Some of them are presented below. Fraser, et al. [13] suggested a seemingly intuitive figure of merit given by:

$$\mathrm{FOM}_1 = \frac{T}{R_S} \qquad (2.1)$$

where T = optical transmittance, R_S= sheet resistance. This FOM is misleading because it attains a maximum at a transmittance of 37%, which would be impractical for most TCC applications. To circumvent this, Haacke [14] proposed the following modification to this definition:

$$\mathrm{FOM}_2 = \frac{T^x}{R_S}, \text{where } x > 1 \qquad (2.2)$$

Haacke selected $x = 10$ as appropriate because it could lead to $T = 90\%$ at the maximum FOM. Gordon [1] proposed a quantitative measure of the performance of TCO thin films to be the ratio of the electrical conductivity, σ, to the visible absorption coefficient, α,

$$\mathrm{FOM}_4 = \left(\frac{\sigma}{\alpha}\right) = -\left[\frac{1}{R_s \ln(T+R)}\right] \qquad (2.3)$$

in which R_s is the sheet resistance in ohms per square, T is the total visible transmittance and R is the total visible reflectance. TCOs ranking high on this criterion of merit (σ/α), i.e. $(1/\rho\alpha)$ can be expected to lie high up, and close to the Y-axis in Fig. 2.1. A theoretical upper limit for (σ/α), for the given wavelength λ, may be estimated from the transport theory of electrons in metals [15], given by:

$$\left(\frac{\sigma}{\alpha}\right)_{\max} = \frac{4\pi^2 \varepsilon_0 c^3 n (m^* \mu)^2}{\lambda^2 e^2} \qquad (2.4)$$

where ε_0 is the permittivity of free space, c is the speed of light in vacuum, n is the refractive index of the film, m^* is the effective mass of the conduction electrons, μ is the mobility, λ is

the wavelength of light, and *e* is the electronic charge [1]. Other FOMs described by Ivanov, et al. also deal with high frequency behavior and bendability of TCCs.

2.2 Indium Tin Oxide Crystal Structure

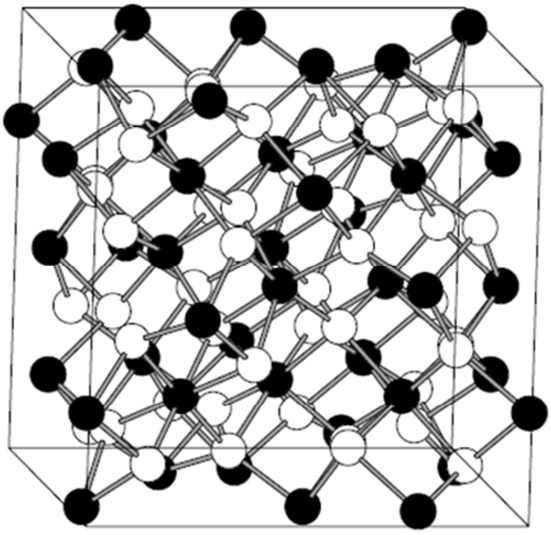

Fig. 2.3: In_2O_3 crystal structure: bixbyite unit cell ($In_{32}O_{48}$) [16]

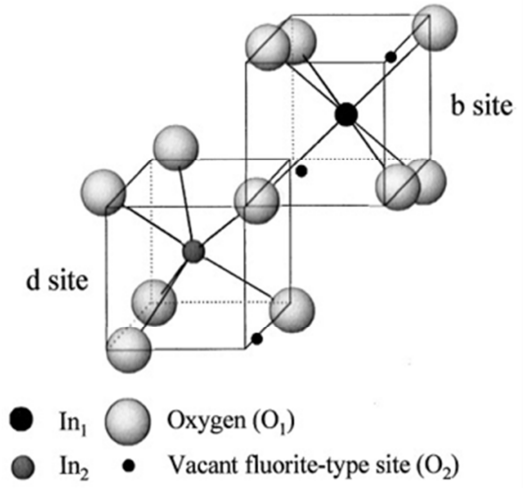

Fig. 2.4: Non-equivalent *b* and *d* sites in the In_2O_3 bixbyite structure [17]

Indium Oxide has a cubic bixbyite structure, which is a derivative of the fluorite structure. A schematic of the In_2O_3 structure is shown in Fig. 2.3. The unit cell contains 80

atoms, and has a lattice parameter of 10.117Å. Since In_2O_3 has only three-fourths of the anions as compared to the corresponding fluorite stoichiometry, only three-fourths of the anion sites are occupied in the In_2O_3 structure. This structure has two different six-fold coordinated cation sites, a symmetric site referred to as a *b* site; and a non-symmetric site, referred to as a *d* site (See Fig. 2.4). The 32 cations occupy 8 of the 16 *b* sites and 24 of the 48 *d* sites in the unit cell [18, 19]. This is similar to the fluorite structure where half of the 8-fold coordinated cation sites are occupied. The *b* sites in In_2O_3 are distorted octahedral sites surrounded by six equidistant O^{2-} anions 2.18 Å away, at the vertices of the cube, with vacancies at the two diagonally opposite vertices. The *d* sites have O^{2-} neighbors at three different distances near the corners of a cube with two vacancies along one of the face diagonals. When doped with SnO_2, it is widely accepted that the Sn^{4+} ions go into the In_2O_3 and substitute on the indium sites [18, 19]. Sn^{4+} ions show a preference for the symmetrical *b* sites [17, 20]. This substitution may be represented in the Kröger-Vink notation as follows:

$$2SnO_2 \rightarrow 2Sn_{In}^{\bullet} + 3O_O^{\times} + O_i''$$

2.3 Defects and Electronic Conductivity in Indium Tin Oxide

The defect structures of ITO have been studied and modeled by Frank and Köstlin [18], González et al. [19] and others [17, 21-24]. They have suggested the presence of Sn-O clusters which can be either reducible or non-reducible. The reducible cluster, $(2Sn_{In}^{\bullet}O_i'')^{\times}$, also referred to as the 2:1 cluster based on the atomic ratio in it, has two non-adjacent Sn^{4+} ions and an oxygen interstitial anion. It is a loosely bound cluster [19]. Non-reducibility in Sn-O clusters arises from the aggregation and proximity of tin cations around oxygen interstitials. As more tin cations surround an oxygen interstitial, as in 3:1 Sn-O clusters, the harder it becomes to remove the O_i from the bixbyite lattice [19]. The dominant charge

carrier generation mechanism in ITO is the removal of oxygen interstitials [17], which occurs due to the reduction of the reducible 2:1 clusters. This may also be thought of as the "activation" of the donor species.

$2In_{In}^{\times} + 2SnO_2 \rightarrow (2Sn_{In}^{\bullet}O_i'')^{\times} + In_2O_3$ … formation of the reducible cluster

$2(2Sn_{In}^{\bullet}O_i'')^{\times} \rightarrow O_2(g) + 4Sn_{In}^{\bullet} + 4e'$ … reduction of the Sn-O cluster, releasing electrons.

Once all donor species are "activated", the charge carrier concentration does not change much with further reduction until the onset of significant oxygen-vacancy formation under highly reducing conditions:

$$O_O^{\times} \rightleftharpoons \frac{1}{2}O_2(g) + V_O^{\bullet\bullet} + 2e'$$

Oxidizing conditions decrease the carrier concentration, whatever the tin content [17]. Frank and Köstlin [18] suggested that an increase in oxygen partial pressure leads to the formation of the non-reducible fluorite type clusters.

The exact nature of the band structure of indium oxide has not yet been conclusively established [25, 26]. Pure indium oxide has a wide band gap [27] of 3.6 eV (also quoted as 3.75 eV [28] and 3.84 eV [29] elsewhere). Hence, it has a very low concentration of free electrons at ambient conditions. Doping with Sn can increase the charge carrier concentration [18]. Doping with Sn, or the presence of oxygen vacancies as above, cause shallow donor or impurity states close to the host (In_2O_3) conduction band [28]. On doping with a higher concentration of dopants, a degenerate gas of electrons is created. This causes ITO to have high electronic conductivity, as well as metal-like reflection in the far-infrared region, while keeping the band gap of the native host largely unchanged. ITO can thus stay transparent in the visible region. The real band gap is decreased on doping with tin due to the many-body effects. However, due to the partial filling up of the conduction band, the

effective band gap observable through optical spectroscopy is actually increased. This is known as the Burnstein-Moss (BM) shift [21]. This is illustrated in Fig. 2.5(a) and (b).

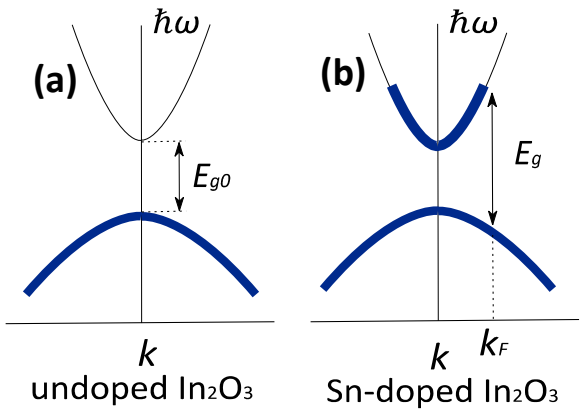

Fig. 2.5 (a): Band structure of undoped In_2O_3 in the vicinity of the band gap, (b): Effect of Sn doping - reduction in band gap & increase in effective band gap (after [21]).

Although the charge carrier concentration does increase with an increase in the level of Sn doping, the carrier concentration has been found to be maximum at 4-6 at. % Sn, and decreases beyond this limit [17] as shown in Fig. 2.6. This may be related to the solid solubility limits of SnO_2 in In_2O_3. The solid solubility of tin in In_2O_3 has been reported to be in the range of 7 ± 2 atomic percent Sn [18, 30]. See Fig. 2.7 for the calculated binary phase diagram [31]. Nadaud et al. proposed that the observed decrease in the carrier density with increase in tin content beyond 6-8 at. % could be due to the formation of electrically neutral $In_4Sn_3O_{12}$-like configurations within the indium oxide network [17]. Warschkow et al. proposed that increasing the tin content may start increasing the proximity of 2:1 Sn-O clusters, which combine to form non-reducible 3:1 clusters [23]. This is illustrated in the schematic in Fig. 2.8.

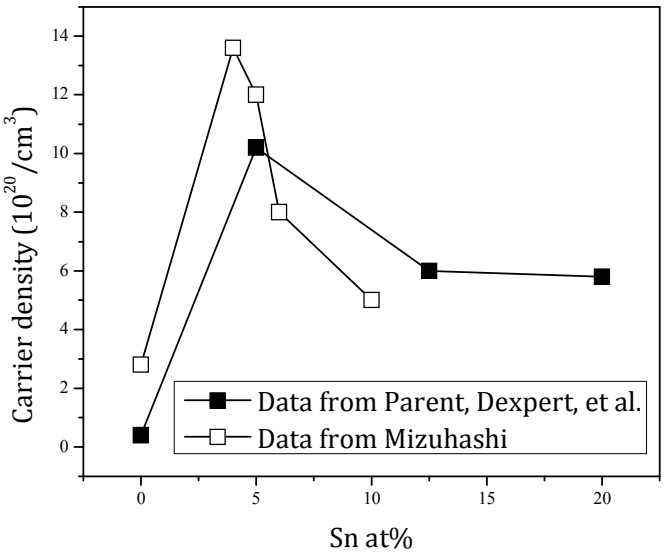

Fig. 2.6: Carrier density (*N*) versus Sn content in ITO thin films mentioned in the literature (after chart in [17], data: Mizuhashi [32], Parent et al. [33])

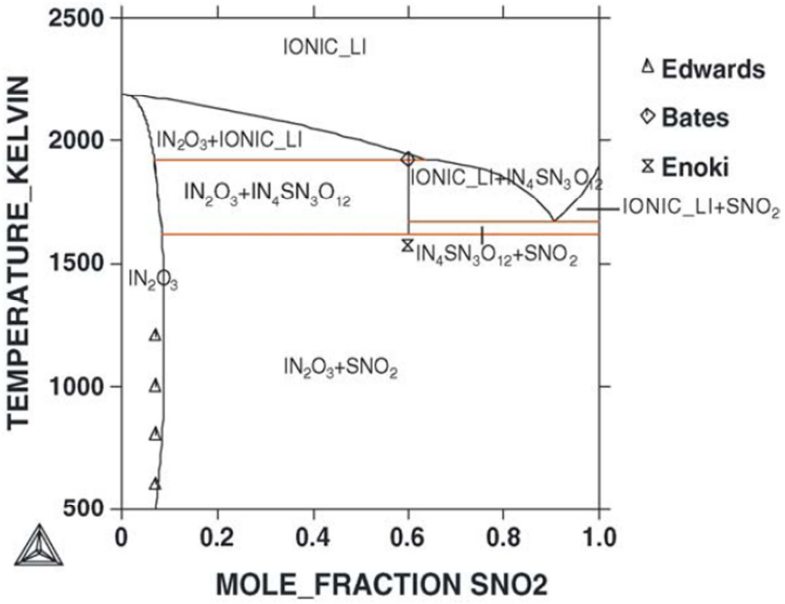

Fig. 2.7: Calculated In_2O_3-SnO_2 phase diagram [31]

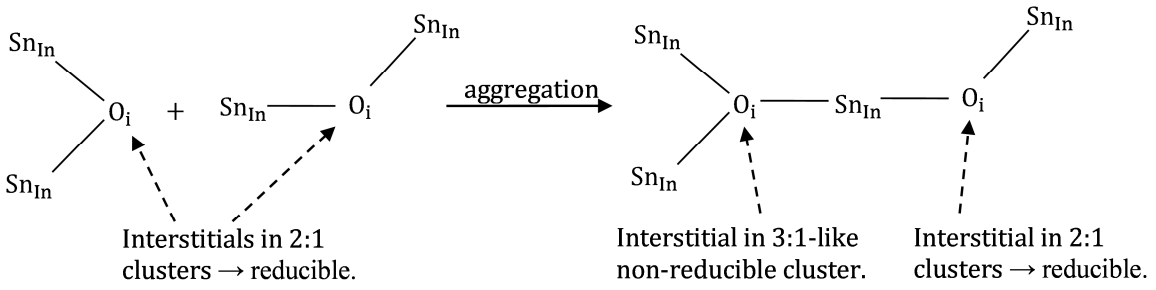

Fig. 2.8: Schematic of aggregation reaction of two reducible 2:1 clusters to form a 3:1 cluster. One of the local O_i environments resembles a 3:1 cluster and is expected to be non-reducible [23]

2.4 Electrical Transport in Materials

The conductivity of a material, σ, is given by $\sigma = \sum_i (n_i|q_i|\mu_i)$, where n_i = charge carrier concentration, q_i = carrier charge, μ_i = mobility of that charge carrier in that medium. The charge carrier mobility, in turn, is related to the effective mass, m^* and the relaxation time, τ by the relation, $\mu_i = q_i\tau_i/m_i^*$. The transport in polycrystalline materials is much more complex compared to that in single crystals [34]. Transparent conducting oxides like ITO are degenerately doped, leading to a Fermi level within the conduction band. TCOs are very similar to metals in the respect that the carrier concentration is nearly independent of the temperature. Thus, the electron scattering processes are also similar to those in metals. These include residual resistivity due to impurities and dislocations, phonon scattering, substitutional impurity scattering, grain boundary scattering, surface/interface scattering, and percolative transport [34].

Ionized impurity scattering is caused by ionized dopant ions, and it dominates for carrier concentrations above 10^{19}cm^{-3} [35]. Scattering due to neutral shallow impurities is not significant in TCOs. This is because the shallow donors in TCO materials exhibit ionization energies around 50 meV, and as a result, the concentration of neutral donors is very low at room temperature [35]. Polycrystalline materials will generally have

contributions to the overall impedance of the material coming from grain boundaries and other crystal defects in addition to those from the grain bulk. The specific grain boundary resistivity of conducting materials need not be similar to that of the bulk grain. Often, it can be several orders of magnitude higher [36], and can lead to increasing the overall resistivity by as much as three orders of magnitude [37]. In addition, surface scattering can be dominant, especially in thin films, where the mean free path may be comparable to the film thickness.

Grain boundaries and grain interfaces lead to electronic defects in the band gap of semiconductors. Majority charge carriers can get trapped or depleted at these grain boundary defect states. This leads to a charge build-up at the grain boundaries and a compensating opposite charge distributed towards the inside of the grain. This charge separation leads to a potential barrier Φ_0 to charge carrier movement at the grain boundary. This potential barrier has a Schottky barrier character. This is called the space charge effect and can contribute to the grain boundary impedance [37-41]. As a result of this potential barrier, the resistance of the grain boundary may be expressed as [41]:

$$R_{GB} = R_0 \exp\left(\frac{\Phi_0}{kT}\right) \qquad (2.5)$$

where R_0 = bulk grain resistance. In discontinuous metallic films of a typical metal with work function of ~4-5 eV, where the conducting phase is in the form of islands separated by free space or a non-conducting matrix; electronic transport is dominated by thermionic and Schottky emission for separations $d > 100$Å [42]. Tunneling is the dominant mechanism for $d \sim 20 - 50$Å. If instead of free space, there is a dielectric matrix between the particles, then the barrier height for tunneling is much less. This is because the barrier height is the difference between the work function of the metal and the electron affinity of the dielectric, and the transmission coefficient is enhanced [42].

2.5 Current TCO Deposition Techniques and Their Shortcomings

Transparent conducting oxides (TCOs) are employed as thin films or layers for most applications. The properties of a TCO film not only depend on its chemical composition, but also the manner in which the layer was made [43]. The use of spray pyrolysis for the commercial deposition of TCOs like ITO and tin oxide has been around for more than half a century. In the recent decades, chemical vapor deposition (CVD) has been adopted for depositing fluorine doped tin oxide. Commercial deposition of ITO is typically carried out on glass substrates for applications such as flat panel displays or thin film solar cells, by pulsed laser, dc magnetron sputter systems, or by electron beam evaporation[2]. These techniques need the substrates to be heated to a high temperature during deposition, as well as undergo a high temperature post annealing to achieve crystallization and conductivity enhancement in the ITO films [44, 45], as low substrate temperatures can result in the deposition of amorphous ITO with inferior electro-optical properties [46]. The low substrate temperature can also reduce the activation efficiency of the tin dopant, thus reducing the carrier density and electron mobility through ionized impurity scattering [2]. Typical resistivities obtained for such films are five times higher than those that can be achieved on glass substrates currently used in the flat panel displays [47, 48]. Hence the substrates also need to be heat resistant, which means that using these techniques for flexible, heat sensitive substrates is difficult. Temperature considerations apart, sputtered ITO films deposited on flexible substrates like polyethylene terephthalate (PET) have been shown to be very susceptible to cracking at low strains (<2%) [49, 50]. Hence, the applicability of the current techniques to flexible substrates is limited.

Alternative liquid phase approaches such as sol-gel synthesis [51], combined with spin coating or dip coating may accommodate complex shaped substrates; but they still have a problem due to the amorphous nature of the as-deposited layers, which necessitate

subsequent heat treatments to achieve fully crystalline films [52]. This problem can be solved by using a wet chemical deposition of dispersions containing crystalline ITO nanoparticles [52-54]. It is possible to disperse ITO nanoparticles in a suitable medium and fabricate circuits or coatings using techniques such as inkjet printing [8, 9], Langmuir-Blodgett films deposition [55, 56], microcontact printing [5] or nanoimprint lithography [6]. Nanoparticles having a narrow size distribution may be expected to assemble into a more efficient close-packing than particles having a random size distribution [57]. In addition, because of the nano-scale size of the particles, we may expect the films and circuits fabricated using crystalline nanoparticles to sinter at fairly low temperatures. Thus, crystalline nanoparticles may be considered an attractive route to fabricating conducting films and transparent circuits even on flexible and heat sensitive substrates such as films made from PEN (polyethylene naphthalate) and cellophane.

2.6 Synthesis of Nanoparticles

2.6.1 General Methods of Synthesis

Nanoparticle synthesis can be divided broadly into gas phase synthesis and wet synthesis methods. Kruis et al. [58] have reviewed the synthesis of nanoparticles in the gas phase. Most of these methods are based on homogeneous nucleation in the gas phase and subsequent condensation to form nanoparticles, such as pulsed laser vaporization [59]. A wet chemical “bottom-up” approach to nanoparticle synthesis (as opposed to a “top-down” lithographic method of whittling away nanoparticles from a bulk solid or film) can be used to obtain high quality semiconductor nanocrystals which can have a narrow size distribution [60, 61]. Wet methods include arrested precipitation methods like inverse micelles based methods [62, 63], and sol-gel based and hydrolysis methods [64-66]. Wet chemical methods usually involve the use of polymeric stabilizer ligands. These polymeric

ligands attach to the surface of colloidal particles and prevent agglomeration due to steric interactions with the ligands on other particles. Colloidal dispersions stabilized in this manner can have high colloid concentrations, are relatively electrolyte insensitive, and can accommodate multiple types of colloids in the dispersion. Interaction between the solvent and the polymeric stabilizers can affect the conformation of the polymer chains and hence the effectiveness of the stabilizer to an extent. Polymeric stabilizers offer an additional advantage in the synthesis of nanoparticles in narrowing the size distribution by forming a diffusion barrier to the growth species, resulting in a diffusion limited growth of nuclei. Steric stabilization can be combined with electrostatic stabilization, which is also referred to as electrosteric stabilization, when polyelectrolytes are used as stabilizing agents [67].

2.6.2 Non-aqueous nanoparticle synthesis

Wet chemistry is a popular route to synthesizing nanoparticles. Murray, Norris and Bawendi described the synthesis of cadmium chalcogenides from organometallic precursors by a “hot injection method”. This involves the injection of the precursors dissolved in trioctylphosphine (TOP) into a high-boiling, coordinating organic solvent, trioctylphosphine oxide (TOPO) at 300°C [57, 68], which causes a sudden burst of nucleation of nanoparticles. The nanoparticles grow in a diffusion controlled manner due to the steric diffusion barrier formed by the coordinating TOPO molecules, resulting in a narrow size distribution of nanoparticles [67].

Murray et al. have also proposed an alternative, simpler synthetic approach [57]. This involves mixing the reagents in a vessel at a relatively low temperature to preclude any appreciable reaction. A controlled ramp of the solution temperature accelerates the decomposition of the reagents to produce the requisite supersaturation, which is then relieved by a burst of nucleation. The slow, diffusion limited growth allows the nanocrystals

to anneal and form nearly defect-free lattices, identical to the bulk lattice, especially if high boiling solvents like octadecene are used. After the desired amount of growth, the nanocrystals can be separated from the growth solution by adding a non-solvent, and can then be re-dissolved in a suitable organic solvent to form stable colloidal suspensions [69].

There was a rapid response to the hot injection method first published by Murray et al. [68], and there were many adaptations, which were summarized by Vanmaekelbergh and coworkers [69]. Peng and coworkers [70-72] have since devised a method to synthesize monodisperse, crystalline In_2O_3 nanoparticles. Indium carboxylate precursor and myristic acid (MA) as an optional free ligand are dissolved in a high-boiling, non-coordinating solvent like in 1-octadecene (ODE). 1-octadecyl alcohol (OA) or 1-octadecyl amine (ODA) can be optionally used as activators. Tin dopant can be added in the form of a tin carboxylate salt to the solution. The use of a non-coordinating solvent here permits a much finer tuning of the ligand concentration. The particle size and shape can be controlled based on various synthesis parameters like the use and proportion of MA, activator, mode of reaction – direct heating versus hot injection, heating program, etc. This is illustrated in Fig. 2.9, which was taken from a paper published by Narayanaswamy et al. [70]. For example, the use and proportion of ligands like myristic acid (MA) can be used to control the shape of the nanoparticles and nanoparticle agglomeration into nano-flowers. Choi et al. have synthesized ITO nanoparticles by a similar method, starting from acetylacetonate precursors in oleylamine [73].

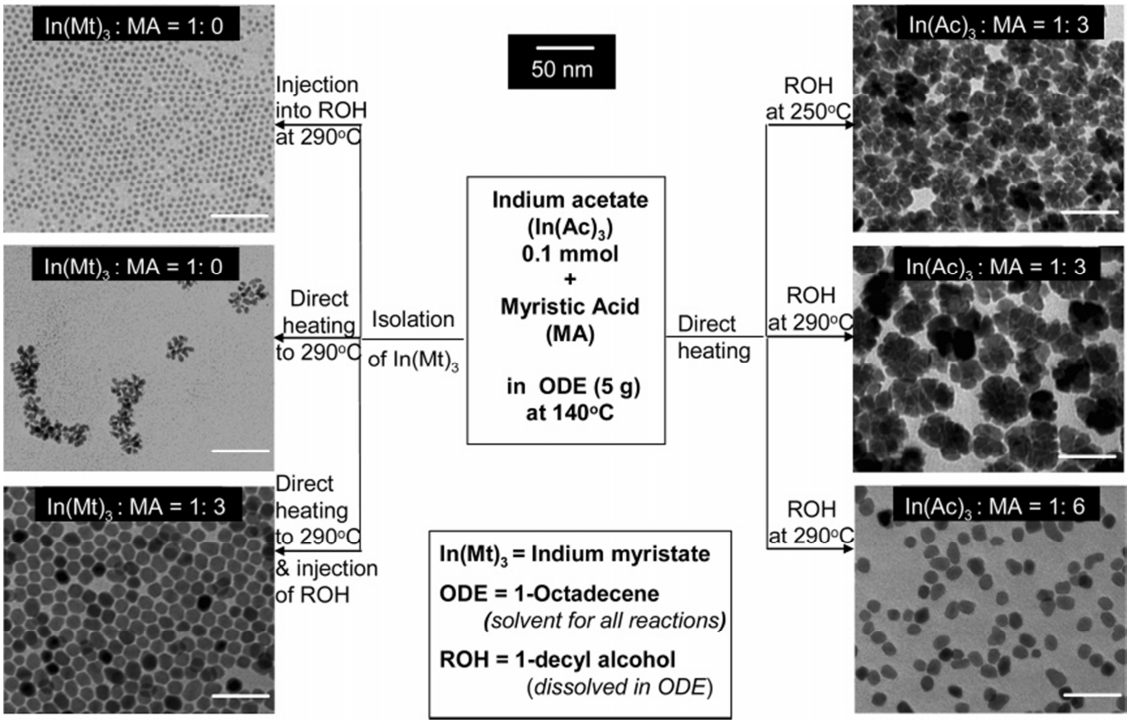

Fig. 2.9: Variation in the morphology of ITO nanoparticles synthesized by the myristate esterification method, as a function of various synthesis parameters [70]

2.7 Impedance Spectroscopy

The general approach to measuring electrical properties in the dc mode involves applying an electrical stimulus such as potential difference or current to a sample, and measuring the response, such as the current or the potential difference. These measurements are often done with the implicit assumption that a steady state has been reached; or after waiting for a sufficient time to let the system approach a steady state. Thus, such measurements either assume that properties of the electrode-material system are time-invariant [74], or these measurements ignore the transient behavior that usually accompany the application of the electrical stimulus. A multitude of fundamental microscopic processes take place when a system is electrically stimulated; the sum of which forms the electrical response [74]. These processes can include the transport of charge carriers (mobile electrons, holes or ions) through conductors, transfer of charge carriers at interfaces, movement and alignment of electrical dipoles, electrochemical reactions that involve the creation, recombination or the change in the oxidation state of ionic species. The transport processes are further modified by defects and band structure details. More information about these processes can be obtained by characterization through impedance spectroscopy. Impedance spectroscopy (IS), in its most commonly used form, involves the determination of the complex impedance (Z^*) of the system by measuring the current (I), voltage (V) and the phase angle (θ) over a wide frequency range. The complex impedance is defined as follows [75]:

$$Z^* = \frac{V(\omega)}{I(\omega)} = Z' + jZ'' = |Z^*| \angle \theta \qquad (2.6)$$

where $V(\omega) = V_m \sin(\omega t)$, $I(\omega) = I_m \sin(\omega t + \theta)$, $\omega = 2\pi f$, $|Z^*|$ = impedance magnitude, and θ = phase difference between the current and the voltage.

The complex impedance can be visualized in the form of a frequency implicit polar plot, with the imaginary part of the impedance on the Y-axis and the real part of the impedance on the X-axis. It is customary to plot the Y-axis in the reverse direction, such that the negative values lie above the X-axis. These polar plots are called Cole-Cole plots or Nyquist plots. The shape of the Cole-Cole plot often gives very visual clues about the electrical behavior of the system. An example of a Cole-Cole plot is shown in Fig. 2.10. It shows the impedance of a parallel RC circuit, which consists of a resistor R and a capacitor C connected in parallel (shown in inset in Fig. 2.10), calculated over the frequency range of 1 mHz – 1 GHz, has been plotted in it. A semicircle can be seen in the first quadrant of that plot. Incidentally, this is a common feature in many impedance spectra, which indicates that at least a part of their impedance behavior has a resistive-capacitive component to it.

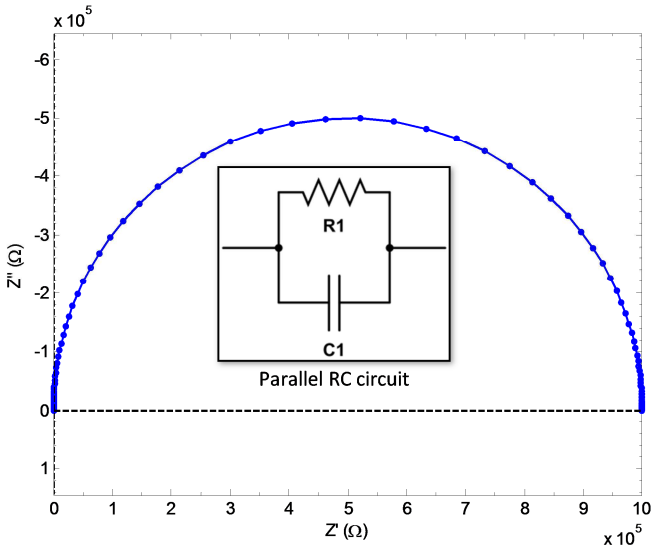

Fig. 2.10: Cole-Cole (Nyquist) plot of impedance of a parallel RC circuit (R = 1 MΩ, C = 1 pF), calculated over the frequency range 1 mHz – 1 GHz

The complex impedance can also be presented by plotting it in the form of plots of the frequency explicit plots, in which, the real and imaginary parts of the impedance or /and the magnitude and the phase angle of the impedance are plotted against frequency in the

log scale. The Bode plots of the impedance of the parallel RC circuit described in Fig. 2.10 are shown in Fig. 2.11, showing (a) impedance magnitude, (b) real part of impedance, (c) impedance phase angle, and (d) imaginary part of impedance. Impedance Bode plots are often presented as a pair of Bode plots of impedance magnitude and phase angle, or as a pair of Bode plots of the real and imaginary parts of impedance. Presenting both the pairs of the Bode plots is not necessarily redundant because very often it is possible to get information about different aspects of the impedance spectra from either of them, especially for more complex spectra. In the Bode plot of impedance magnitude shown in Fig. 2.11 (a), for the parallel RC circuit described above, the high frequency portion essentially consists of an inclined straight line. This decrease in the impedance magnitude with frequency is a signature of capacitive behavior. At lower frequencies, the curves flatten out to a plateau. This indicates a transition to a resistive-dominant behavior, because an impedance magnitude independent of frequency is indicative of resistive behavior. The value of the impedance magnitude that these Bode plots plateau into represents the dc resistance of the material. The real part of impedance is shown in a Bode plot in Fig. 2.11 (b). For the parallel RC circuit being discussed, the variation of the real part of impedance with frequency is similar, though not identical, to that of the impedance magnitude, shown in Fig. 2.11 (a). It must be noted that other types of circuits can have impedance spectra, in which the real part of the impedance behaves very differently from the impedance magnitude. Fig. 2.11 (b) is plotted with its Y-axis in the linear scale. It can be seen that the real part of impedance has a very low value at high frequencies, and it transitions over to a high value of 1 MΩ corresponding to the value of the resistor, at low frequencies.

The nature of impedance behavior can also be seen clearly in the Bode plots of the impedance phase angle which is shown in Fig. 2.11 (c) and in the Bode plots of the imaginary part of impedance, shown in Fig. 2.11 (d). Fig. 2.11 (c) shows that the phase

angles are at around –90° at high frequencies. A phase angle of –90° indicates purely capacitive behavior. Fig. 2.11 (c) shows that for the impedance data being considered, the phase angle increases from –90°, going from higher to lower frequencies, and relaxes to zero at low frequencies. This indicates a resistive behavior at low frequencies.

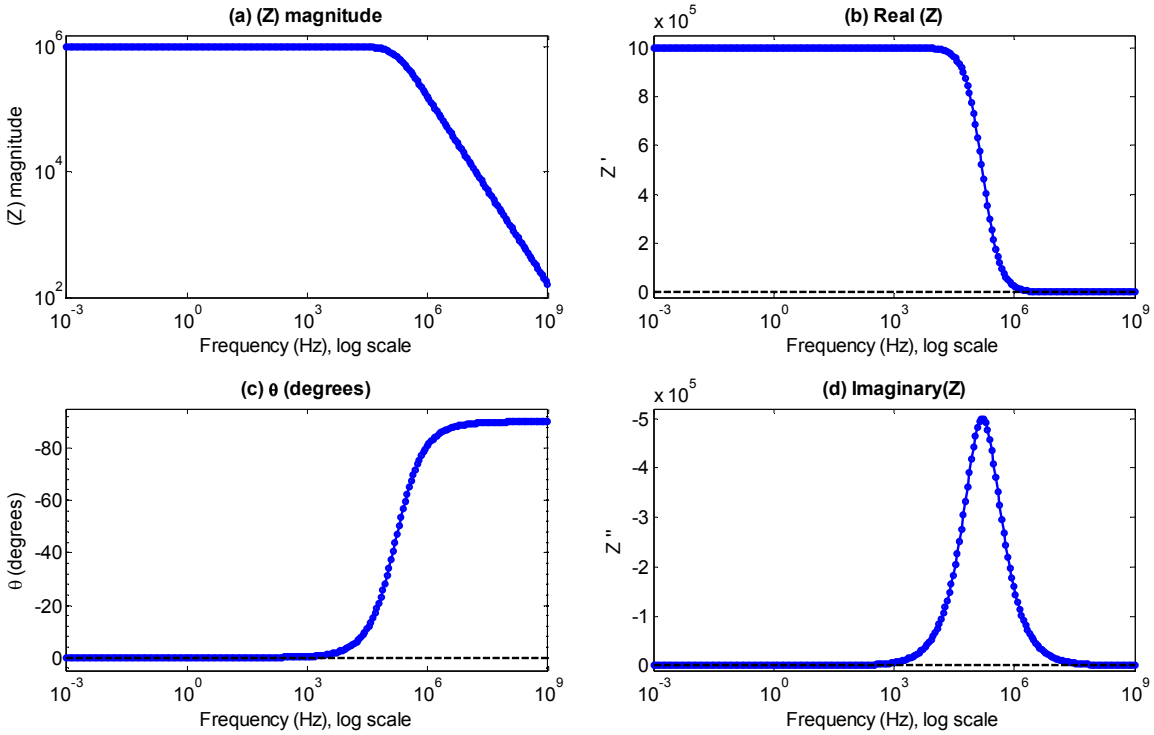

Fig. 2.11: Bode plots of impedance of a parallel RC circuit (R = 1 MΩ, C = 1 pF), showing (a) magnitude impedance, (b) real part of impedance, (c) impedance phase angle, (d) imaginary part of impedance, as a function of frequency

The Bode plot of phase angle shows that most of the shift from capacitive to resistive behavior occurs over a certain frequency window. This shift is related to the relaxation time constant of the RC element. The relaxation time constant is a measure of how quickly the system can "relax" to a steady state following electrical stimulation. In case of the parallel RC element, the relaxation time constant is essentially a measure of how quickly the capacitor can charge or discharge through the resistor. The Bode plot of the imaginary part of impedance shows a local maximum or a local minimum at a frequency

called the frequency of relaxation, as seen in Fig. 2.11 (d). The relaxation frequency also corresponds to the point of inflection of the Bode plot of the real part of impedance, shown in Fig. 2.11 (b). The relaxation time constant is related to the frequency of relaxation, f_{relax}, as shown in Eqn. 2.1 .

$$\tau = \frac{1}{\omega} = \frac{1}{2\pi f_{\text{relax}}} \qquad \text{Eqn. 2.1}$$

A common method to analyze impedance spectra is to model equivalent circuits to fit the data [74-77]. These may contain discrete electronic elements like resistors, capacitors, and inductors, or an infinite series like Warburg elements; or distributed elements. The equivalent circuits thus modeled can give us an insight into the electrical transport processes occurring within the material. One needs to be careful while fitting circuits and assigning physical interpretations to it because it is possible to have different circuits that have the exact same impedance at all frequencies [74].

2.8 Direct write fabrication of transparent conducting oxide films

Several authors have reported research on direct-write fabrication of transparent conducting oxide films and patterns in the literature, as opposed to techniques like sputtering and e-beam evaporation, which are used commercially [2]. The reported lowest sheet resistance achieved has varied over a big range. Most of the papers tried to tackle the problem by dispersing ITO nanoparticles that are available commercially, or those that were synthesized and separated in powder form prior to fabricating films [78-82]. Cho, et al. [80] dispersed ITO nanopowder using dispersing agents like 2,4-pentanedione, or titanate coupling agents like isopropyl tri(N-ethylenediamino) ethyl titanate. Upon curing at 180°C, sheet resistances of 2.4-3 kΩ/sq were reported for films with titanate coupling agents. The authors suggested that titanium doping of ITO contributed to the improvement in conductivity. They also reported that larger particle size of ITO decreased ITO sheet

resistance due to reduction of contact resistance between aggregates, but increased visible light scattering. Reindl et al. dispersed commercially available ITO nanoparticles in ethanol using trioxydecanoic acid (TODS) [79] as dispersing agent. Upon thermal treatment at 250°C in air, they reported dc conductivity as low as 10^{-1} to $10^{-2}\Omega^{-1}\text{cm}^{-1}$. However, since the reported electrical properties were all measured at 2-10 Hz between inter-digitated electrodes with a spacing of 200 μm, these results are questionable. It is possible that the reported results have a significant RC component, and the actual dc conductivities could be much lower. Jeong, et al. [78] reported ITO films inkjet-printed from ITO dispersion annealed at 450°C to have sheet resistance of 202 Ω/sq. Aegerter, et al. [81] dispersed ITO nanoparticles with ethylene glycol, alkoxy silanes and photo-curing agents. They reported a sheet resistance of ~800 Ω/sq after a series of treatments involving UV curing, and annealing in air and followed by annealing in forming gas. Hong, et al. [82] inkjet-printed ITO films using ITO dispersions and annealed them at various temperatures up to 600°C in air and in N_2. They reported sheet resistance down to 455 Ω/sq for films annealed at 600°C.

Other approaches that eschew starting from ITO nanoparticles, such as sol-gel coatings and spray coatings have also been reported. Beaurain et al. [83] made ITO films using the sol-gel method from indium and tin chlorides with 2,4-pentanedione in ethanol by multiple step dip coating with a 260°C heat treatment between two dip coating steps. Final annealing at 300-500°C resulted in films with sheet resistances between 137-727 Ω/sq. Gouskov, et al. [84] used the spray coating method to fabricate ITO coatings using indium and tin chlorides with substrate temperatures in the range of 300-450°C. They reported sheet resistance of 26 Ω/sq for 0.2 μm thick ITO coating. Munir et al. [85] fabricated ITO films by electrospinning from chloride precursors with PVP in EtOH, DMF solvent on steel mesh. Upon calcination at 500°C in ambient conditions, films with sheet resistance of around 10^6 Ω/sq were obtained.

Many of the results reported above needed high temperature annealing to achieve acceptable electrical properties. This makes those methods unsuitable for applications where the substrates are not heat-resistant, such as polymer substrates like PET and PEN, which may be used in applications like flexible and portable displays or very large format displays. Commercially available ITO nanopowder often has a wide size distribution. This is evident from the TEM image of Sigma-Aldrich ITO nanopowder shown in Fig. 2.12 [86].

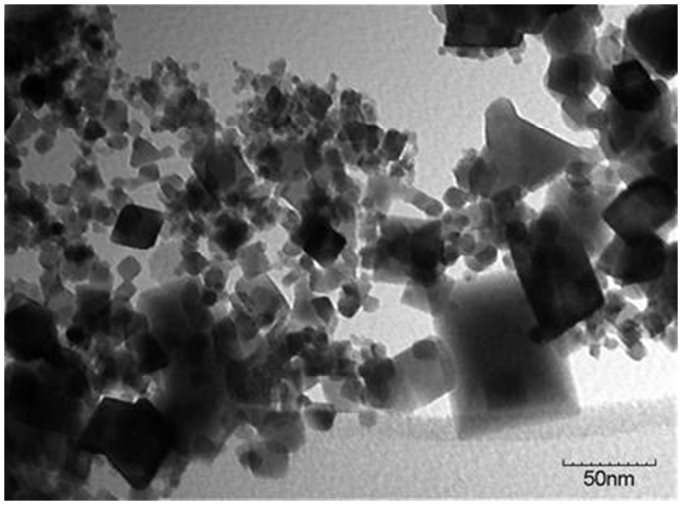

Fig. 2.12: TEM image of Sigma-Aldrich ITO nanopowder [86]

This can potentially result in films which have very non-optimal packing, as well as high roughness, which can result in inferior electrical properties, as well as increased light scattering. In addition, if the particle size is not small enough, the nanoparticles may be unsuitable for use in inkjet printers because of the potential for clogging the print head orifices. Hence, it would be advantageous to synthesize ITO nanoparticles through colloidal synthesis, using a method which can yield nanoparticles with a narrow size distribution. It would also be advantageous to make the ITO solution directly during the synthesis process rather than doing a two-step process of synthesizing the nanoparticles first, followed by dispersing them in solution and fabricating films from them [78, 81-83, 87-89]. This is not only because it saves an additional step of re-dispersing the nanoparticles, but also because

exposure of the nanoparticle surface to ambient atmosphere during storage can potentially contaminate the nanoparticles due to dust, moisture and adsorbed gases. The research presented in the following chapters describes the work done to prepare ITO solutions through colloidal synthesis, fabricate ITO films, and to explore the effect of various processing methods on the properties of the ITO films. This was done with an aim that this research may help develop processing techniques to fabricate good quality ITO films without needing to use very high temperature processing; and therefore be able to fabricate patterned circuits on flexible substrates.

Chapter 3:
Experimental Procedures

This chapter gives the general details about the synthesis of colloidal ITO nanoparticles, the fabrication and basic processing of colloidal ITO films, as well as the characterization techniques used. However, it does not include all the experimental procedures. Some of the experimental procedures, which may be applicable to specific chapters only, will be described in those chapters.

3.1 Colloidal ITO Nanoparticles

3.1.1 Synthesis

Fig. 3.1 shows a schematic diagram of the set-up used for the synthesis of colloidal ITO. It consisted of a three-necked round bottomed flask, in which the synthesis was performed, placed on a heating mantle attached to a variable power source; and a magnetic stirrer. The flask was attached to a vacuum pump tank to allow for degassing and to an argon tank to maintain an argon atmosphere during the synthesis. Fig. 3.2 shows the flowchart of the steps involved. Colloidal indium tin oxide nanoparticles were synthesized [90] by the esterification of long chain carboxylic acid salts of indium and tin by a long chain alcohol. This was done by mixing appropriate amounts of indium and tin acetate precursors, stored under argon, with myristic acid (tetradecanoic acid) and 1-octadecanol in a high boiling point solvent, 1-octadecene. The solution was degassed under vacuum at room temperature and at 120-130°C. It was then heated to 300°C to form a solution of ITO nanoparticles. This solution was cooled to about 280°C, and the ITO nanoparticles were annealed in situ at this temperature for a duration of 30 minutes to 1 hour. After cooling the

solution, the nanoparticles were separated by standard polar-non polar solvent techniques [91], and dispersed in a non-polar solvent like hexane, chloroform or toluene.

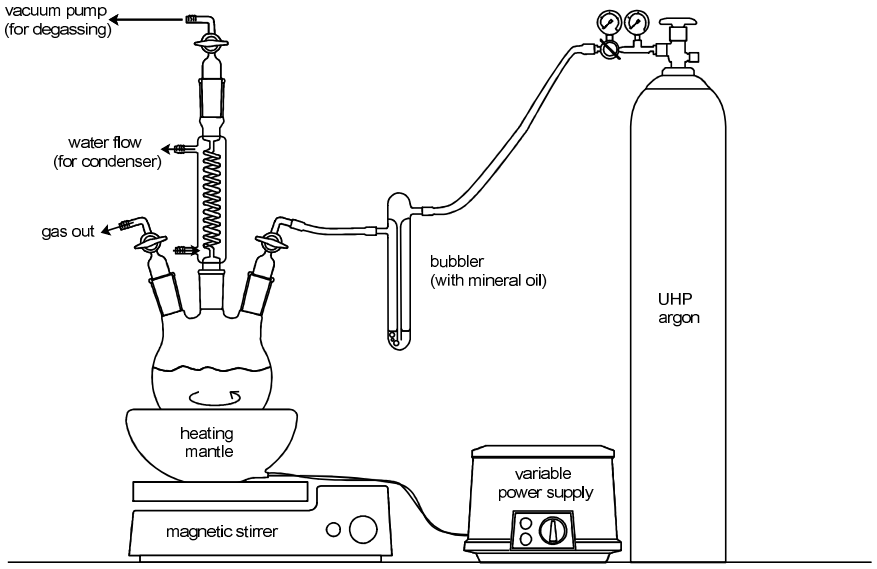

Fig. 3.1: Schematic illustration of the set-up used for colloidal synthesis

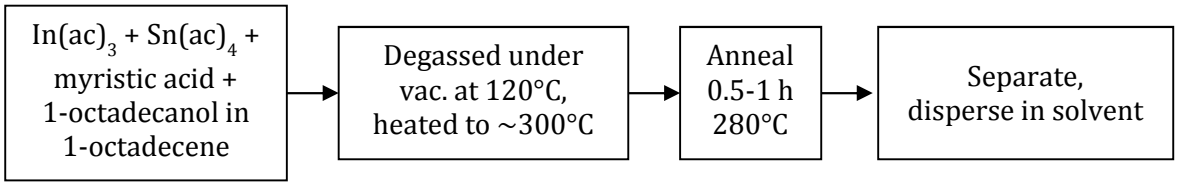

Fig. 3.2: Flowchart showing the steps involved in non-aqueous synthesis of ITO nanoparticles

3.1.2 Characterization of ITO nanoparticles

3.1.2.1 Transmission Electron Microscopy (TEM)

ITO nanoparticles were observed under the JEOL 100CX II transmission electron microscope (TEM) using an accelerating voltage of 100 kV. The samples were prepared by depositing diluted as-prepared solutions on lacey carbon film coated copper grids and letting them dry completely. High resolution TEM (HRTEM) imaging of the ITO nanoparticles was done using the JEOL 4000EX, using an accelerating voltage of 350 kV. The

samples were prepared in the manner described for JEOL 100CX II TEM, but with the addition that the copper grid was baked overnight at 70°C to ensure complete removal of the solvent.

3.1.2.2 X-Ray Diffraction (XRD)

The synthesis of ITO was confirmed by X-ray diffraction (XRD), done on an X'Pert Systems PRO Alpha-1 diffractometer, using Cu Kα1 incident X-ray radiation. The as-prepared colloidal ITO solution was dropped onto a Si (510) zero-background substrate (vendor: The Gem Dugout) and air-dried prior to the XRD analysis.

3.2 Spin-Coated Colloidal ITO Films

3.2.1 Fabrication

Films were fabricated from the ITO nanoparticle solution by spin coating, using a Cee 200 spin coater (shown in Fig. 3.3). Glass and fused quartz microscope slides were cut into 0.5" × 0.5" square pieces for use as substrates. These were cleaned in acetone and isopropanol prior to spin coating. A piece of Scotch tape, which was a little larger than the substrate was stuck to the back side of the substrate in order to prevent the ITO solution from curling back over the edge of the substrate at the corners of the square and getting on the other side of the substrate. The spin coating was done by pipetting out 33 µl of the colloidal ITO solution onto the cleaned substrate. The spin coater was accelerated at 333 rpm/s to 1000 rpm and spun for 27 s; and then accelerated at 1000 rpm/s to 5000 rpm and spun for 25 s. Three repetitions of this process were done for each film to build up the thickness of the film up to about 200 nm.

Fig. 3.3: Cee 200 Spin coater

3.2.2 Characterization of ITO films

3.2.2.1 Atomic Force Microscopy (AFM)

The surface topography of the colloidal ITO films was investigated by atomic force microscopy in the non-contact mode (NC-AFM). It was done on a Park Systems XE-100E atomic force microscope, using ACTA probes (Nanoscience Instruments Inc.). The instrument is placed on a TS-150 vibration isolation system from Table Stable inside a standard acoustic enclosure from Park Systems, as shown in Fig. 3.4 (a). Fig. 3.4 (b) shows a schematic of the non-contact mode of atomic force microscopy. The method involves a cantilever vibrating at its resonant frequency. It has a sharp, downward facing tip, which is rastered across the sample surface, keeping a very small distance between the mean position of the vibrating tip and the surface. The surface height variations are sensed through changes in the surface van der Waal's forces affecting the tip, which are manifested in changing its effective resonant frequency. The AFM system senses this, and moves the tip up and down in sync with the topography, and thus measures it.

The ACTA AFM probes have a length of 125 μm, with a spring constant of 40 N/m, and a resonant frequency of 300 kHz. The AFM tip radius is less than 10 nm (typical tip radius ≈ 6 nm). "Large scale" scans 1 μm wide and larger, were done using the high XY voltage and high Z voltage modes. "Small scale" scans 500 nm, and 200 nm wide were done in the more sensitive low XY voltage and low Z voltage modes in order to get as much detailed information about the local topography as was possible.

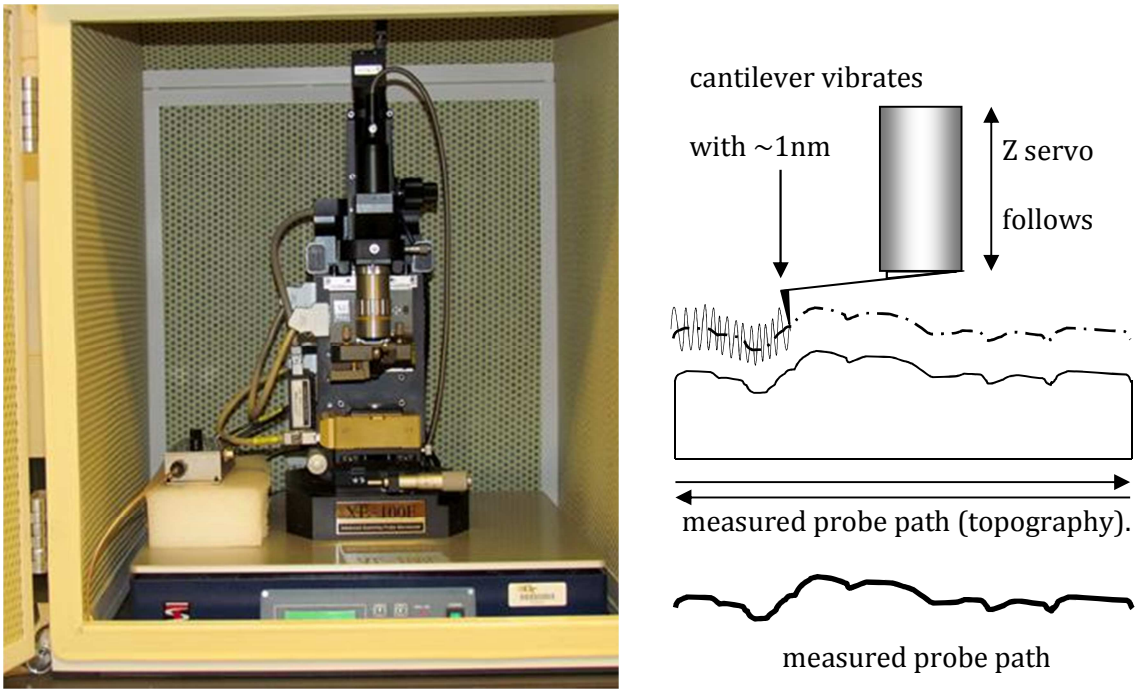

Fig. 3.4: (a) Park Systems XE-100E AFM
(b) Schematic of a non-contact mode AFM

3.2.2.2 X-Ray Diffraction (XRD)

X-ray diffraction scans were done on non-plasma-treated films as a function of annealing temperature, on an X'Pert Systems PRO Alpha-1 diffractometer, using Cu Kα1 incident X-ray radiation. These scans were done on a PanAnalytical X'Pert PRO MPD system in the standard Bragg-Brentano geometry [92, 93]. The set-up is shown in Fig. 3.5 (a), and the details of the Bragg-Brentano geometry are shown in Fig. 3.5 (b). Since these films were

very thin, composed of nanoparticles, and were deposited on amorphous substrates, the X-ray diffraction peaks were very weak, and the pattern (not shown) was dominated by scattering from the amorphous substrate. Hence, more detailed X-ray diffraction scans were done on these films in the vicinity of the strongest peak (222) at 30.585°, in the range 25°-40°, and crystallite size was calculated using the Scherrer relation [93].

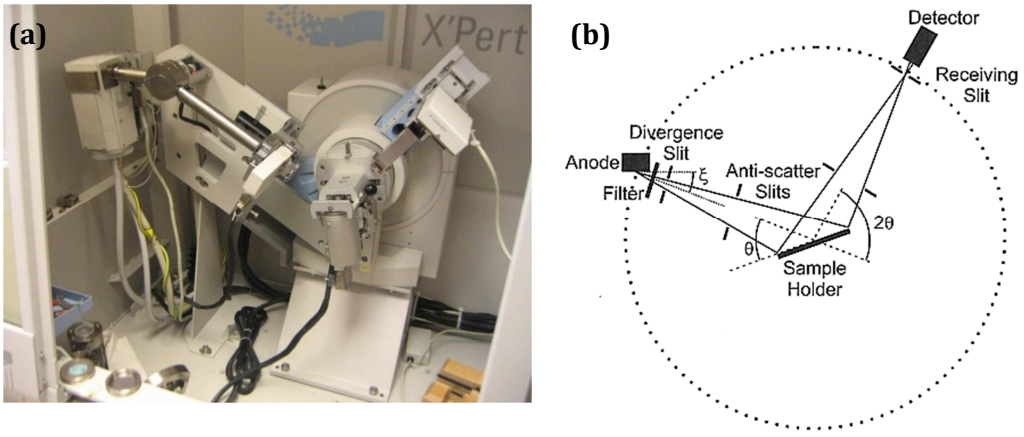

Fig. 3.5: (a): X'Pert Systems PRO Alpha-1 X-Ray Diffractometer in a Bragg-Brentano configuration [94], (b): Schematic of Bragg-Brentano geometry [92]

3.2.2.3 Impedance Spectroscopy

The electrical characterization of the colloidal ITO films was done by impedance spectroscopy [75], performed using a four-point probe set-up with 62.5 mils (1.5875 mm) tip spacing and a tip radius of 1.6 mils (40.64 μm). The equipment used was a Solartron 1260 Impedance Analyzer in conjunction with a Solartron 1296 dielectric interface at frequencies ranging from 0.1 Hz – 1 MHz. This set-up allowed us to look at the variation in the "in-plane" electrical properties at different locations on the film.

Fig. 3.6: Solartron 1260 attached to Solartron 1296 dielectric interface

Fig. 3.7: Four point probe head being used for measurement on a coated substrate

3.2.2.4 Optical Characterization

The optical transmittance of the films was characterized by UV-visible absorption spectroscopy on a Cary 5000 spectrophotometer, using a clean non-coated substrate – fused quartz or glass, as the case may be, as the baseline. The percent transmittance in the visible region was calculated by taking an average of the transmittance over the wavelength window of 400-700 nm.

Chapter 4:
Colloidal ITO Nanoparticles and Spin-Coated ITO Films

4.1 ITO nanoparticles

4.1.1 Synthesis Procedure and Observations

Colloidal indium tin oxide nanoparticles with tin content equivalent to approximately 18 weight percent SnO_2 were synthesized [90] by a non-aqueous method from acetate precursors. 1.6602 mmol indium (III) acetate (Sigma Aldrich), 0.3398 mmol tin (II) acetate (Alfa Aesar), 6 mmol myristic acid (Sigma Aldrich) and 6 mmol 1-octadecanol (Sigma Aldrich) were taken in ~28 ml of a high boiling point, non-polar solvent, 1-octadecene (Sigma Aldrich), in a reaction flask. These reagents and solvent had been stored in a nitrogen filled glove box. The solution was degassed under vacuum at ~120°C to remove traces of moisture and dissolved air. This process was continued for about 20-30 minutes, until there was no evolution of any bubbles observed. It was very important to remove all traces of moisture to prevent premature hydrolysis of the reagents. During this process, the mixture of reagents swirling in the flask also changed from a milky white to a nearly clear transparent solution, indicating a complete dissolution of the reagents in the high boiling point solvent, 1-octadecene. After this, the solution was heated to 300°C under a flow of ultra-high purity (UHP) argon gas.

As the temperature of the solution increased with heating, the color of the solution gradually changed from a faint yellow at temperatures exceeding 220°C to orange to brownish-red. At around 275°C, the solution turned very dark – almost black, and settled into a greenish-black color at temperatures beyond 290°C. This color change is shown in Fig. 4.1. The solution was heated to about 300°C, and then cooled to 280°C, where the

nanoparticles in the solution were allowed to be annealed for a duration of 30 min to an hour. The solution was then cooled and some chloroform was added to facilitate the extraction of nanoparticles. The as-prepared dispersion of ITO nanoparticles in hexane contains ITO nanoparticles stabilized by myristic acid ligands [95] via steric stabilization. The ITO nanoparticles were precipitated using standard polar/non-polar solvent techniques [91]. The extraction was done by adding a polar solvent like acetone, miscible in 1-octadecene and in chloroform to the cooled solution described above. This causes the nanoparticles covered by the non-polar myristic acid ligands (because of the alkyl groups facing outward) to agglomerate and precipitate. They were then separated by centrifugation, and were dispersed in hexane. The solution thus prepared contains ITO nanoparticles dispersed in the solvent, sterically stabilized by a capping layer of myristic acid ligands. Fig. 4.2 shows a schematic of the sterically stabilized nanoparticles.

Fig. 4.1: Change in color of the solution during synthesis, going from colorless, shades of yellow, orange and brown to dark greenish-black

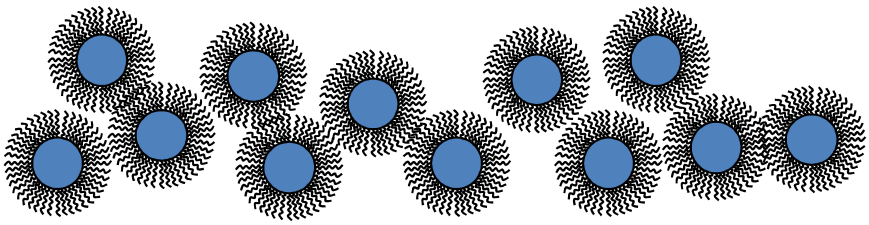

Fig. 4.2: Schematic representation of sterically stabilized ITO nanoparticles [96]

4.1.2 Mechanism of Synthesis

Narayanaswamy et al. [95] have discussed the mechanism of the above synthesis. Hydrolysis and esterification (due to reaction with alcohol) have been identified as the possible pathways. On heating, the indium and tin acetates with myristic acid are partially converted to myristates [95] as shown below:

$$\mathrm{In(CH_3COO)_3} + x\mathrm{RCOOH} \rightarrow \mathrm{In(CH3COO)_{3-x}(RCOO)_x} + x\mathrm{CH_3COOH_{(g)}} \uparrow \ldots [x \approx 2]$$

This partial conversion to myristates has been deemed necessary because direct reactions with acetates at high temperatures have been found to be rather complex. The partially converted myristates then undergo esterification with 1-octadecanol to form indium oxide, as indicated by the reactions below.

$$\mathrm{In(CH_3COO)_{3-x}(RCOO)_x} + \mathrm{H_2O} \rightleftharpoons \mathrm{In_2O_3} + \mathrm{RCOOH_{(g)}} \uparrow$$

$$\mathrm{In(CH_3COO)_{3-x}(RCOO)_x} + \mathrm{R'OH} \rightarrow \mathrm{In_2O_3} + \mathrm{RCOOR'} + \mathrm{H_2O}$$

The excess myristic acid binds to the surface of the ITO nanocrystals as capping ligands. They not only sterically impede agglomeration, and thus keep the nanoparticles dispersed, they also regulate the rate of growth of the nanocrystals during synthesis, and thus helping the nanocrystals obtain a narrow size distribution, as well as reduce the number of crystal defects. In-situ annealing done during the synthesis process also helps to create nearly defect free crystalline particles.

4.1.3 Characterization: Results and Discussion

4.1.3.1 Ageing and Color Change

The as-synthesized colloidal ITO solution is dark, olive green in color. It has been found to slowly change color over time to eventually become blue over a period of 2-4 weeks. Ageing the solution at an elevated temperature of around 50°C inside a sealed vial to minimize solvent evaporation has been shown to reduce the time for this color change to

around 1-2 days or less. An example of this color change has been presented in Fig. 4.3. This could be attributed to the gradual activation of dopants (tin) and the resulting increase in the number of charge carriers [18].

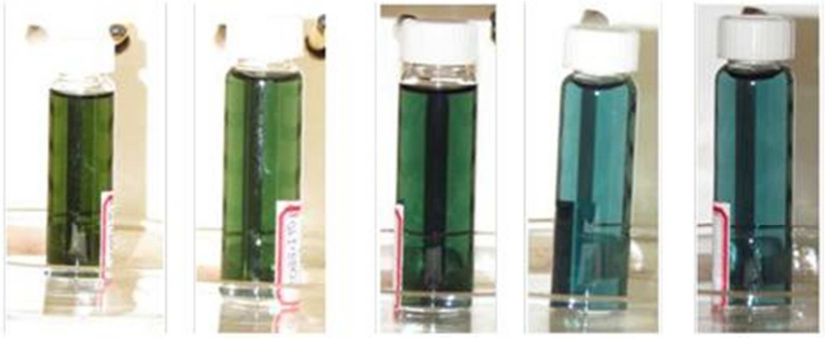

Fig. 4.3: ITO solution, and typical change of color with ageing

4.1.3.2 Transmission Electron Microscopy

Fig. 4.4 shows the TEM image of the as-prepared colloidal ITO nanoparticles [90], with an inset picture of the blue-green colored dispersion of ITO nanoparticles in hexane. It can be seen from the TEM image that the ITO nanoparticles are spheroidal in shape, unagglomerated, and have a narrow size distribution, in the range of 5-7 nm across. Fig. 4.5 shows a high resolution TEM (HRTEM) of ITO nanoparticles. Lattice planes, with a spacing of 2.97-2.98 Å are visible. Based on the lattice spacing, one can conclude that they are (222) planes.

4.1.3.3 X-Ray Diffraction

A comparison of the XRD pattern of the nanoparticles taken on a zero background Si (510) substrate, with that of commercially available ITO nanopowder (Sigma-Aldrich) is shown in Fig. 4.6. This figure confirms that the ITO nanoparticles synthesized by our method are crystalline in the as-synthesized form and do not need annealing to become crystalline [4].

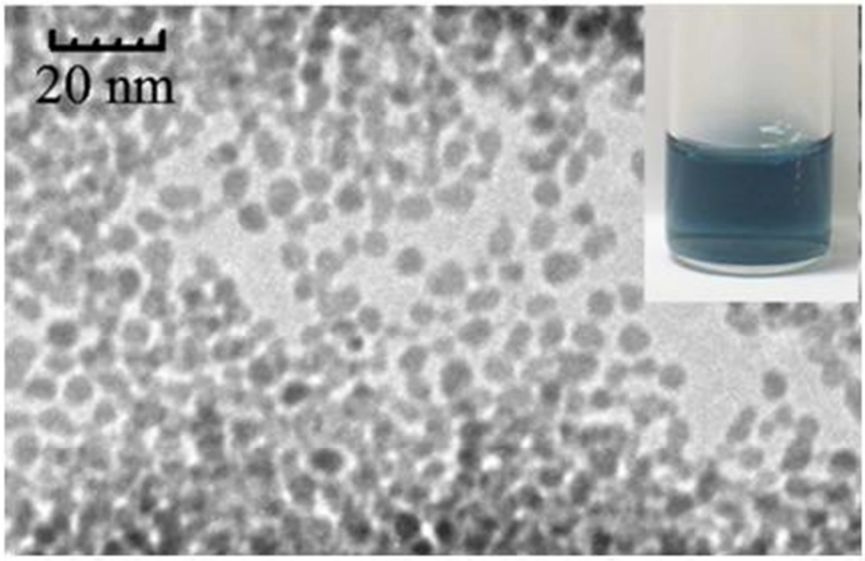

Fig. 4.4: TEM image of colloidal ITO nanoparticles [90]

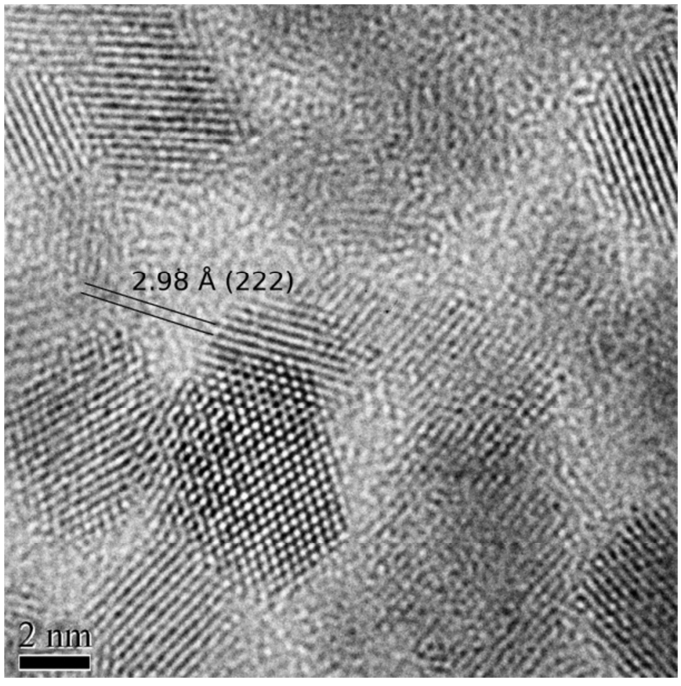

Fig. 4.5: HRTEM image of colloidal ITO nanoparticles

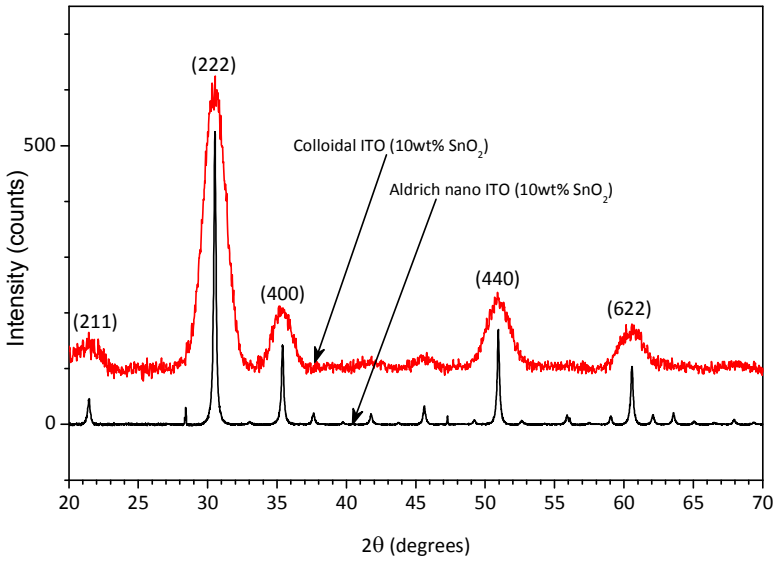

Fig. 4.6: XRD pattern of as-synthesized colloidal ITO compared with that of commercial ITO [90] (Sigma Aldrich ITO nanopowder)

4.2 Spin-Coated Colloidal ITO Films

4.2.1 Characterization: Results and Discussion

4.2.1.1 Appearance

Fig. 4.7 shows the appearance of a colloidal ITO coated glass substrate, in the as-spin coated form. It can be seen that the as spin-coated ITO films are fairly clear and transparent. A small region parallel to the substrate edge was seen to have a variation in the film thickness, which may be attributed to the variation of centrifugal force along the substrate edge, with it being the highest at the corner; and due to the tendency of the liquid to curl back at the lip onto the back side. As mentioned earlier, unwanted deposition occurring in this manner was prevented by masking the back side of the substrate with a piece of Scotch tape. The central portion of the film was uniform, and all the characterization was done in this region.

Fig. 4.7: As-spin coated colloidal ITO film on glass substrate

4.2.1.2 Atomic Force Microscopy (AFM)

Fig. 4.8 shows a 200 nm × 200 nm non-contact AFM topography image of a colloidal ITO film in the as-deposited state. The color of every pixel in the image indicates the relative height variation in the film. The color scale is shown on the left of the image. The local height variations, across two horizontal lines (red and green, as shown on the image) are also shown graphically on the right. It can be seen that, on a local scale, the films are very smooth, with roughness amplitudes (R_a) less than 1.5 nm. When topological features are comparable in size to the diameter of the AFM tip, convolution of the tip shape with the surface topography can cause distortions in the AFM scans [97]. Since the colloidal ITO films under consideration consist of nanoparticles 5-7 nm in diameter, and the AFM probe tip has a radius of curvature in the range 6-10 nm or more, the apparent particle size in the AFM scans, as seen in the XY plane, may be appearing larger than they actually are.

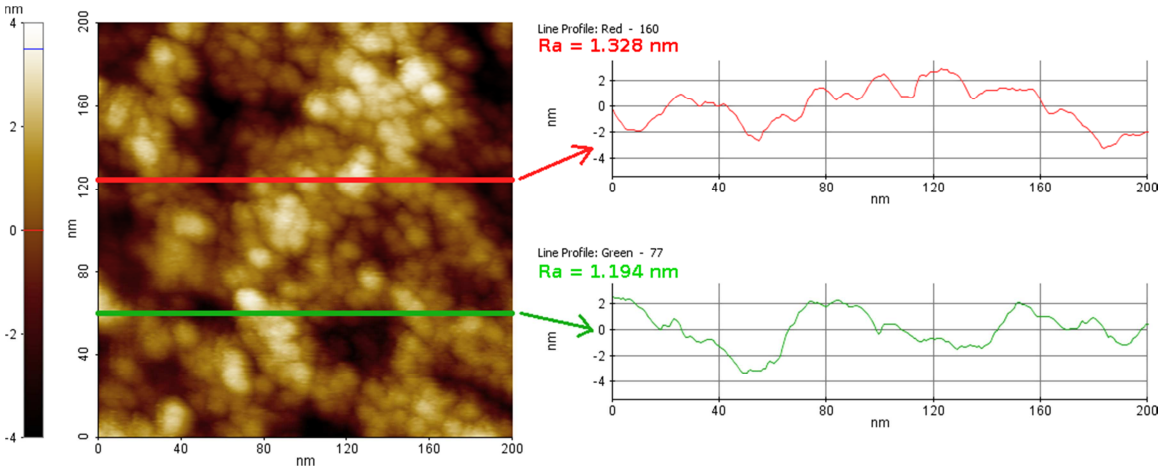

Fig. 4.8: Non-contact AFM image of as-coated colloidal ITO film with height profiles along the two lines shown in the image

Fig. 4.9 shows an optical micrograph of an as-coated colloidal ITO film. This "macroscopic" view of the film shows some variations in the film thickness in the form of variations in color resulting from the interference of incident light. These striations and cell-like structures are known to occur during spin coating of thin films due to evaporation driven surface tension effects [98].

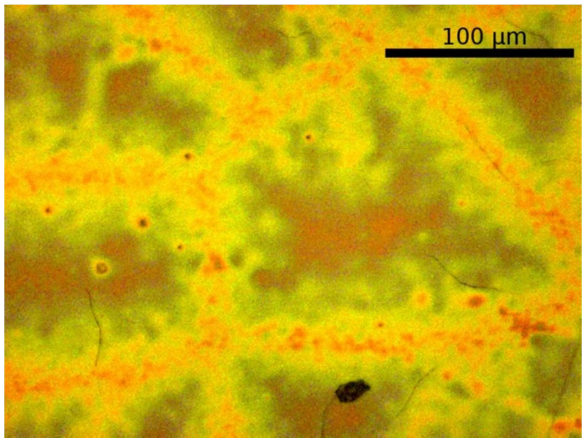

Fig. 4.9: Image of as-coated colloidal ITO film under optical microscope

The film thickness was measured at various locations in the "thick" and "thin" parts by scoring the film to reveal the substrate (Fig. 4.10 (a)), and measuring the step-height profile using non-contact AFM. The NC-AFM images at "thick" and "thin" areas near the

scratch edge and the corresponding step-height profiles across two horizontal lines (red and green, as shown on the image) are shown in Fig. 4.10 (b), (c). The maximum measured thickness was ~300 nm, and at other places, the film thickness was ~200-250 nm. The film morphology described above was seen to be representative of the spin coated films in this study.

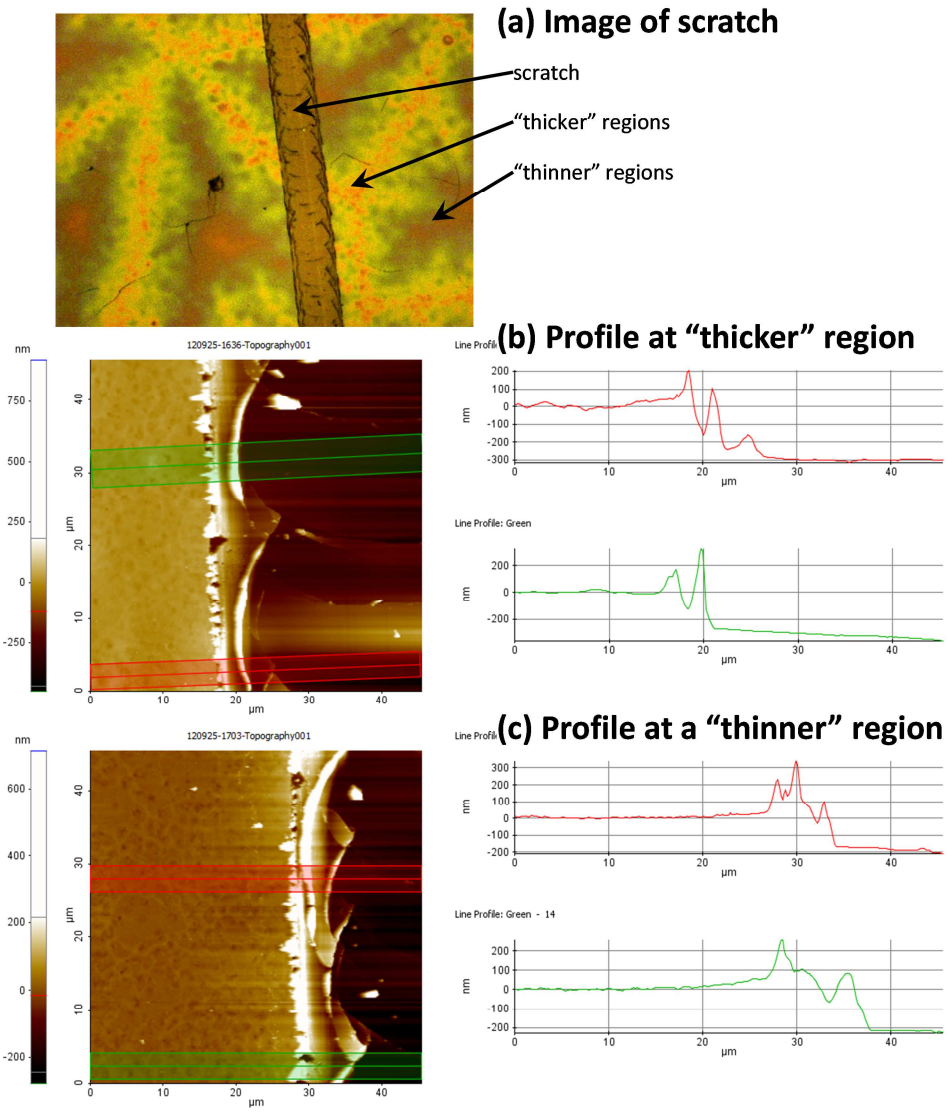

Fig. 4.10: (a) Optical Image of ITO film with a scratch to measure step-height, (b) step height profile as measured by NC-AFM in "thick" region, (c) step height profile as measured by NC-AFM in "thin" region

4.2.1.3 Electrical Characterization

Fig. 4.11 shows a Bode plot of the real part of impedance as measured in-plane, using impedance spectroscopy method, which was described in chapter 3. When the impedance magnitude plot is independent of frequency and appears flat, it corresponds to low impedance phase angles. Such behavior is indicative of a film which behaves like a pure resistor in that frequency range, with a minimal reactive component; while fast changing impedance magnitude or phase angle is representative of a capacitive or inductive response [75]. The plot of impedance magnitude, shown in Fig. 4.11, approximates a sloped, straight line over most of the frequency range used. It is indicative of a very insulating and capacitive behavior.

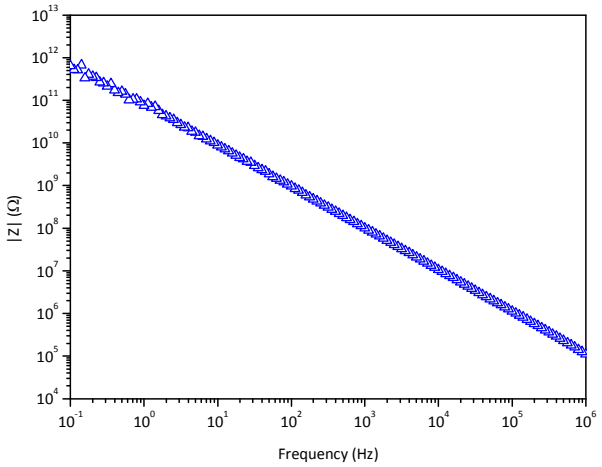

Fig. 4.11: Bode Plot of the impedance magnitude of as coated colloidal ITO film

The DC resistance of the films was estimated by averaging the impedance magnitude for frequencies less than 0.4 Hz, where the value of the phase angle θ was sufficiently small. For highly insulating samples, the impedance phase angle did not reduce sufficiently close to zero at 0.4 Hz. In such cases, the DC resistance was estimated by extrapolating the impedance magnitude to the frequency where the phase angle was extrapolated to zero. This approach was taken instead of extending impedance

spectroscopy measurements to very low frequencies to allow the phase angle to approach zero. This was necessary because instrument limitations tended to make the extremely low frequency data too noisy to be useful. This approach is illustrated in Fig. 4.12. The sheet resistance of the film was calculated from the DC resistance as estimated above, using the following expression:

$$R_s = \frac{\pi R}{\ln\left(\frac{s-r}{r}\right)} \qquad \text{Eqn. 4.1}$$

where, R = measured/estimated dc resistance, s = distance between the electrodes/probes.

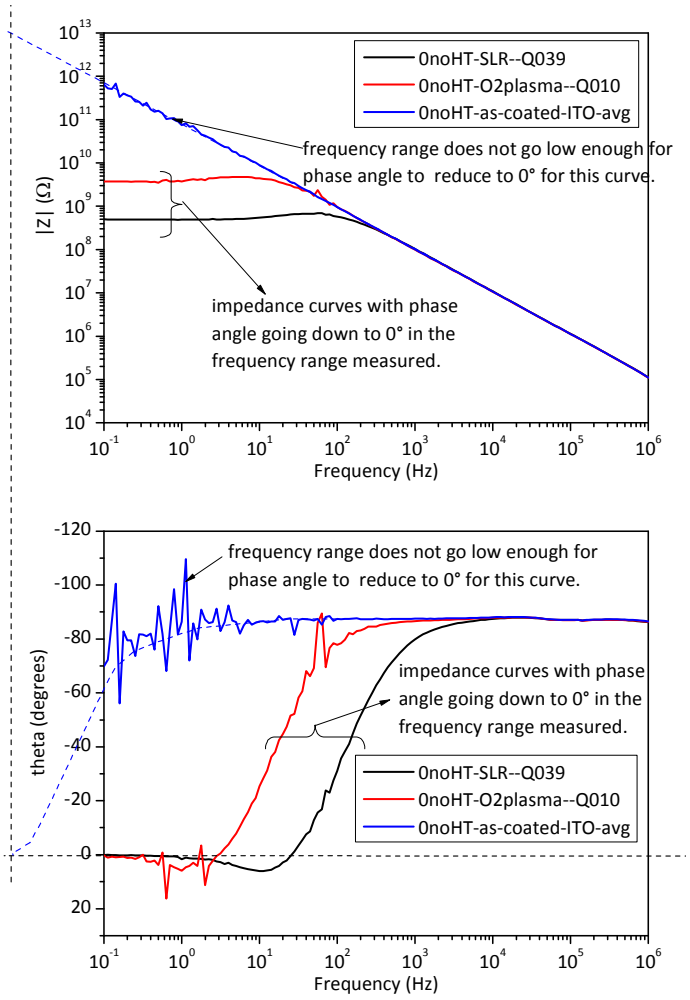

Fig. 4.12: Estimation of *Z'* for insulating samples

4.2.1.4 Optical Properties

Fig. 4.13 shows a chart of the percent transmittance of an as-spin coated ITO film. This measurement was done with a 100% baseline corresponding to an uncoated substrate. It can be seen that the transmittance is very high (~95%) throughout the visible wavelengths (400-700 nm).

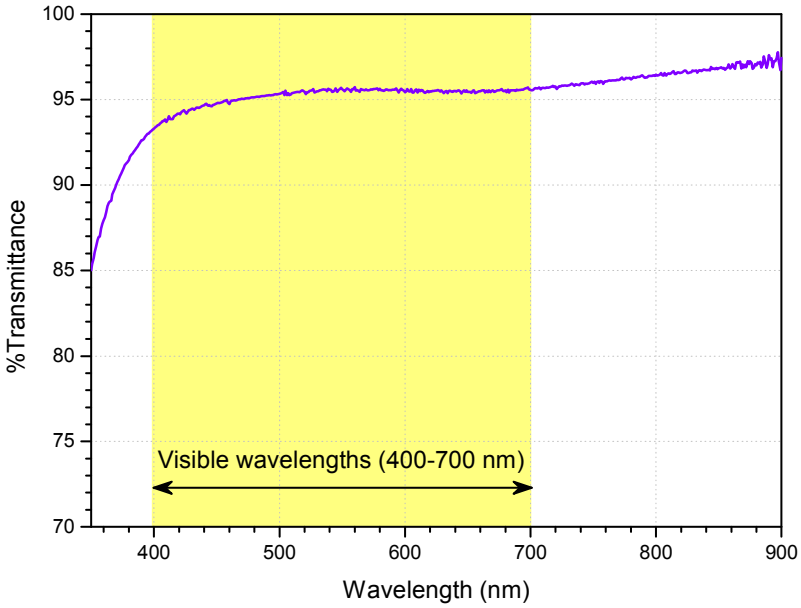

Fig. 4.13: Percent transmittance of as-coated colloidal ITO film on glass slide (w.r.t uncoated glass slide reference)

4.2.2 Discussion: Insulating Nature of Colloidal ITO film

Fig. 4.14 shows a schematic of the structure of an as-coated colloidal ITO film. The ITO nanoparticles are covered by stabilizing, organic capping ligands. Although the ITO nanoparticles themselves are good electron conductors, the passivating ligands on their surface and inter-particle porosity result in poor electrical contacts between the nanoparticles when they are deposited in the form of a film. As a result, carrier transport between the nanoparticles is impeded, which causes the as-coated films of colloidal ITO

have very high resistivity[90], as was seen in the electrical characterization described in Fig. 4.11.

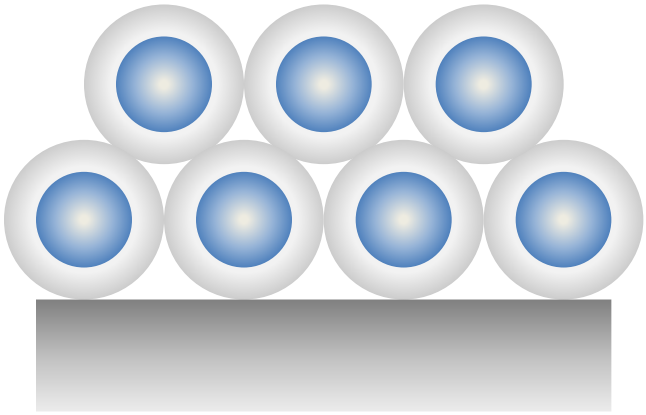

Fig. 4.14: Schematic of the probable structure of the as-coated colloidal ITO film

Chapter 5:
Effect of Annealing on Colloidal ITO Films

5.1 Introduction

As described in chapter 4, the electrical resistivity of the as-coated ITO films is very high. In part, this is because of the presence of organic ligands present on the surface of ITO nanoparticles, which partially contributes to insufficient inter-particle contact, and as a result, impedes current flow. In the absence of these organic ligands, although the electrical resistivity would be significantly better, electrical transport between ITO nanoparticles would still be hindered by the miniscule area of contact expected between the adjoining spheroidal nanoparticles. A straightforward way to remove the insulating organics and improve inter-particle contact through necking and sintering is to anneal the films at a high temperature. This chapter describes the experiments performed to investigate the effect of annealing on the properties of colloidal ITO films.

5.2 Experimental Procedure

5.2.1 Colloidal ITO Films

Colloidal ITO films were fabricated on glass and fused silica substrates (0.5" × 0.5") by spin coating as described in chapter 3. Table 5.1 lists the films fabricated, arranged by the substrates used, as well as by the annealing temperatures and atmospheres used.

Table 5.1: Spin-coated colloidal ITO films used in the annealing study

Annealing Temperature [°C]	Glass substrate		Fused quartz substrate	
	Ar anneal	Air anneal	Ar anneal	Air anneal
No anneal	g049		Q049	
150	g047	g040	Q036	Q017
300	g017	g016	Q035	Q009
450	g042	g021	Q014	Q032
600	---	---	Q054	Q028
750	---	---	Q055	Q053

5.2.2 Annealing Treatments

Annealing of colloidal ITO films was done in a controlled atmosphere, using an alumina tube furnace, at various temperatures: 150°C, 300°C, 450°C, 600°C and 750°C for 48 minutes. A heating and cooling ramp rate of 3°C/min was used. A schematic of the set-up used is shown in Fig. 5.1. The heavy insulation of the furnace sometimes resulted in a rate of cooling slower than the programmed 3°C/min at temperatures below ~300°C. The annealing was done in an atmosphere of ultra-zero grade commercial air (Airgas) or UHP grade argon (Airgas) flowing through the furnace tube.

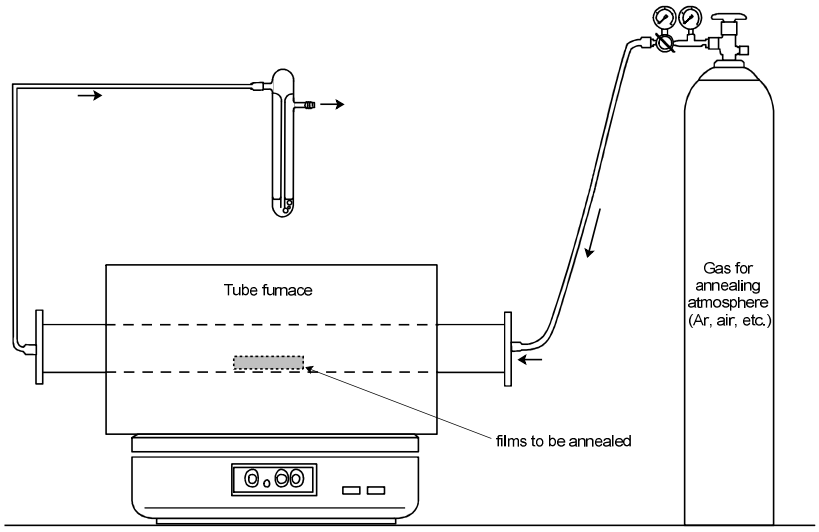

Fig. 5.1: Annealing Set-up

5.3 Characterization of Spin-Coated Films

The as-coated, as well as annealed films prepared in this way were characterized in terms of their physical appearance, and by various techniques. The optical transmittance was measured by UV-visible spectroscopy. The topology was characterized by non-contact AFM. These techniques were described in chapter 3. Similarly, the in-plane electrical properties of the films were determined by using impedance spectroscopy based techniques as described in chapter 3. The relevant results will be discussed later in this chapter. The other characterization techniques used on these films are described below.

5.3.1 X-Ray Diffraction

Annealing treatments, in addition to degrading the organics in the ITO films, can also potentially cause sintering and grain growth in the films because of the elevated temperatures and the nano-size of the crystallites. Although NC-AFM was used to characterize the film topography, an additional measure of the particle size was obtained by Scherrer analysis of X-ray diffraction scans of the ITO films.

X-ray diffraction scans were done on spin-coated ITO films – as-coated, and also after annealing, as a function of annealing temperature using an X'Pert Systems PRO Alpha-1 diffractometer. Cu Kα1 was used as the incident X-ray radiation. A representative X-ray diffraction pattern of a colloidal ITO film annealed at 750°C in argon is shown in Fig. 5.2. It can be seen that the X-ray diffraction peaks are very weak, and the pattern is dominated by scattering from the amorphous substrate. This is because these films were very thin, composed of nanoparticles, and were deposited on amorphous substrates. Hence, more detailed X-ray diffraction scans were done on these films in the vicinity of the strongest peak (222) at 30.585°, in the range 25°-40°, and crystallite size was calculated using the Scherrer relation [93]:

$$t = \frac{0.9\lambda}{B\cos\theta} \qquad (5.1)$$

where t = crystallite size, B = full width at half maximum (FWHM), λ = X-ray wavelength used, θ = Bragg angle.

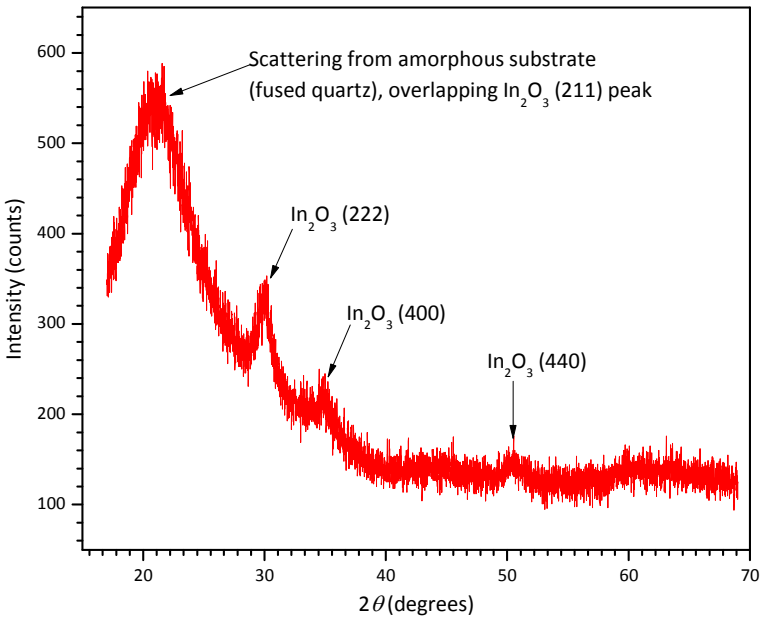

Fig. 5.2: XRD pattern of colloidal ITO film on fused quartz, annealed at 750°C in argon

5.3.2 Thermogravimetric Analysis (TGA)

The weight loss caused by the degradation of residual organics in the dried colloidal ITO was analyzed by thermo-gravimetric analysis (TGA) [96]. This was done in UHP argon and commercial air atmospheres. It is important to do this characterization to understand the changes that may occur in films fabricated out of ITO nanoparticles as a result of being annealed in the respective gas atmospheres. In order to circumvent the difficulty of determining an accurate initial weight due to the non-trivial rate of evaporation of the hexane solvent in ambient conditions, the TGA sample pan was filled with ITO solution and dried by placing it on a controlled temperature hot plate maintained at approximately 90°C. TGA was done on a Q50 thermogravimetric analyzer from TA Instruments, using a sample purge gas flow of 10 ml/min, and a temperature ramp rate of 5°C/min up to a temperature of 750°C.

5.3.3 X-Ray Photoelectron Spectroscopy (XPS)

X-ray photoelectron spectroscopy (XPS) depth profile scans were conducted on ITO films as a function of annealing temperature to compare the degree of removal of residual organics with annealing. In addition to an overall scan, detailed XPS scans were done for carbon 1s (C 1*s*), indium 3d (In3*d*) and tin 3d (Sn3*d*). A comparison of the carbon 1s scans was done to determine the relative amounts of residual organics on the films, and thus compare the ligand removal effectiveness of the annealing treatments. The In3*d* and the Sn3*d* scans help confirm that the X-ray beam was focused, that we were still scanning the ITO surface, and to confirm that each of the C1*s* scans can be considered valid.

These XPS scans were done on a Thermo Scientific K-Alpha XPS system. The X-ray source used for the XPS was an Al K-α micro-focused monochromator, with a spot size of 200 μm. Pass energy of 50 eV, dwell time of 50 ms and an energy step size of 0.1 eV were

used for the carbon 1s scans. In addition to a surface scan, 8 more scans were done after etching away some of the material to expose the material underneath by argon sputtering. Etching for the depth profile was done for 10 seconds for each step, resulting in a total etch time of 80 seconds for the final XPS scan. The etching was done on a raster size of approximately 1 mm × 2 mm, with a current of ~2 μA of Ar^+ ions with energy of 3000 eV. The relative amounts of residual organics in the interior of the films was determined by comparing the C1*s* scans after etching for 80 s.

5.3.4 Raman Spectroscopy

The effect of heat-induced degradation of the residual organics in the ITO films during annealing was also investigated by Raman spectroscopy on films annealed at 300°C and 600°C in ultra-zero grade commercial air or UHP grade argon. It was done on a Thermo Scientific DXR Raman microscope (shown in Fig. 5.3) [99], using a laser of wavelength 532 nm. Since the films that were annealed in air and in argon were characterized in separate batches, Raman spectroscopy of the as-coated film was repeated to ascertain reproducibility.

Fig. 5.3: DXR Raman Microscope - Thermo Scientific (Image Source: [99])

5.4 Results and Discussion

5.4.1 Physical Appearance

Fig. 5.4 shows the visual appearance of the coated films in the as-coated condition as well as after annealing at various temperatures from 150°C through 450°C in argon and in air. It can be seen that the as-deposited films are very transparent, and stay transparent after most annealing treatments, except for the film annealed at 300°C in argon, which shows noticeable darkening.

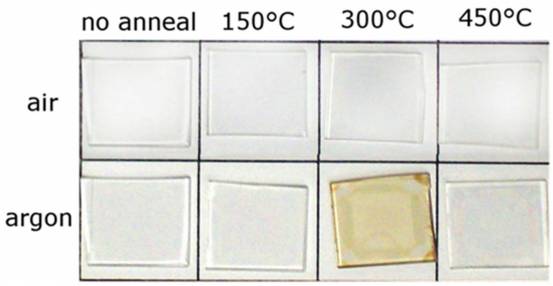

Fig. 5.4: Optical photographs showing the visual appearance of colloidal ITO films [96] as a result of annealing at different temperatures in air and in argon. The size of substrates shown is approximately 12.7 × 12.7 mm (0.5" × 0.5") square [96]

5.4.2 Optical Transmittance in the Visible Range

Fig. 5.5(a) and (b) depict representative scans of the percent transmittance of films over the visible spectrum for ITO films annealed at different temperatures in argon and in air respectively. Most of the ITO films are very transparent through the visible region, and a small decrease in transmittance can be observed at the blue-UV end of the spectrum, which starts approaching the optical band gap of ITO. The film annealed at 300°C in argon, absorbed significantly in the visible region, corresponding to its dark appearance.

Fig. 5.6 displays the percent optical transmittance averaged over the visible wavelengths (400-700 nm) for the films, as a function of annealing temperature and atmosphere. Although the optical transmittance in the visible region is high in the as-coated

colloidal ITO films, as well as after most of the annealing treatments, the average optical transmittance in the visible region was significantly reduced in the colloidal ITO film annealed at 300°C in argon, and to a less extent in the colloidal ITO film annealed at 450°C in argon. This may be attributed to the incomplete pyrolysis of the organics, which resulted in charring of the organics, which was manifested particularly in the 300°C, argon annealed film as a darker, brown colored film (see Fig. 5.4).

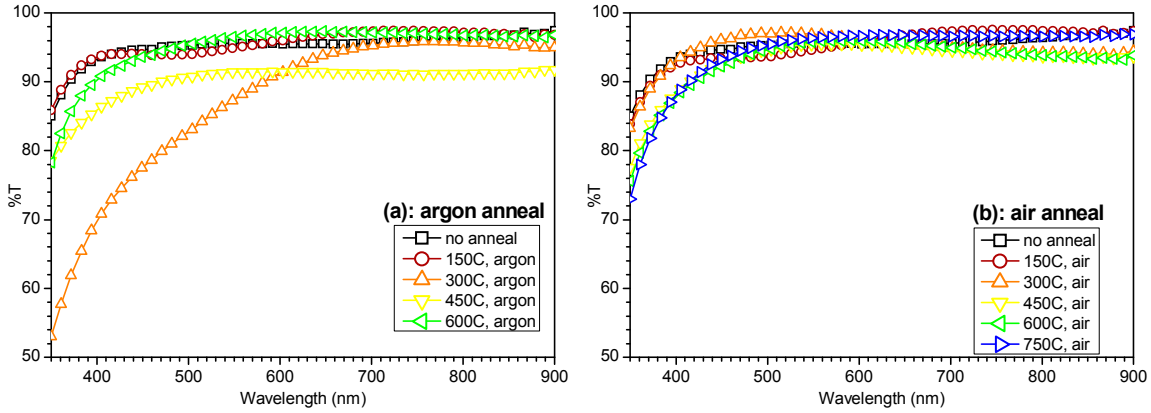

Fig. 5.5: Variation of percent transmittance over the visible spectrum of colloidal ITO films for different annealing temperatures in air and in argon [96]

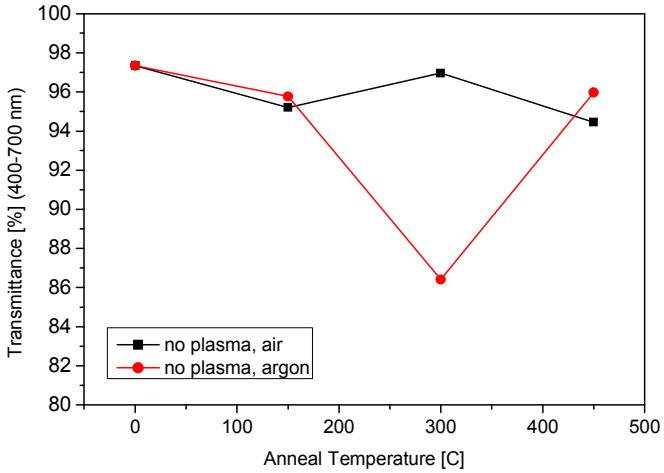

Fig. 5.6: Average optical transmittance of colloidal ITO films in the visible region (400-700 nm) as a function of annealing conditions [96]

5.4.3 Atomic Force Microscopy

Fig. 5.7 (a)-(e) show non-contact AFM topography scans [90] (200 nm × 200 nm) of colloidal ITO films as a function of annealing treatment temperature in air. A discussion of the non-contact AFM image of an as-coated colloidal ITO film is presented in detail in chapter 4. The sizes of the nanoparticles are smaller than what is imaged in the XY plane because of the convolution of the AFM tip shape, as described earlier. However, the Z-scale is representative of the height variations, and they give us an idea of the particle size too. The as-coated films are very smooth on the local scale (200 nm × 200 nm), with some reticular non-uniformity observed on a relatively larger scale (~300 μm × ~225 μm), as shown in Fig. 4.9. The AFM scans do not show any appreciable microstructural evolution with increase in annealing temperature. Apart from a slight increase in grain size, seen in the film annealed at 750°C, there is no significant grain growth observed.

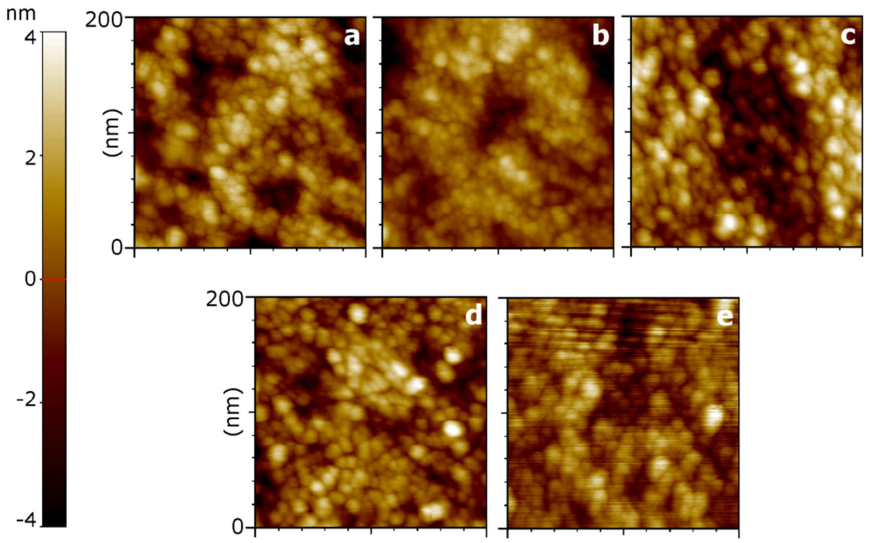

Fig. 5.7: 200 nm × 200 nm NC-AFM scans of colloidal ITO films on quartz vs. annealing in air (a: no anneal, b: 150°C, c: 300°C, d: 450°C, e: 750°C) (Common Z-axis color scale shown. Scale markings on AFM images = 20 nm) [90]

5.4.4 X-Ray Diffraction

Fig. 5.8 (a) shows a comparison of the (222) peak in the XRD pattern of colloidal ITO films deposited on fused quartz, in the as-coated condition, and after annealing at various temperatures from 150°C to 750°C [90]. This peak is the strongest peak in the diffraction pattern of ITO. The peaks in each sample have been plotted after background removal and quintic smoothing on a convolution range of 25 data points; and followed by normalization to the maximum peak height. Fig. 5.8 (b) shows the calculated crystallite sizes, based on the Scherrer equation. No appreciable sharpening of the peaks is seen, indicating that no significant grain growth was caused by annealing even at temperatures as high as 750°C. This is reflected in the calculated crystallite sizes, corroborating the observation from the AFM scans that there was no significant grain growth in the annealed films.

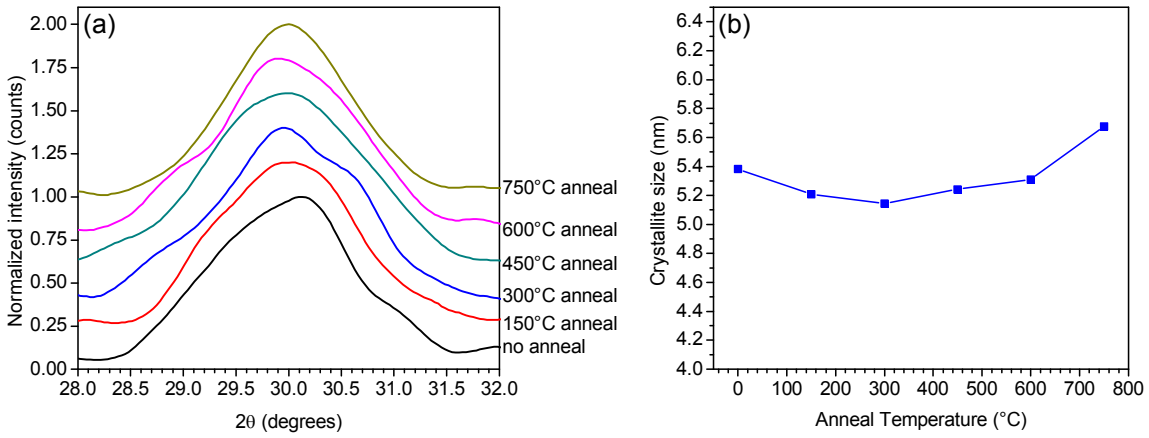

Fig. 5.8: (a) X-ray diffraction scans [90], after background removal and smoothing, of colloidal films annealed in air taken in the vicinity of the strongest peak (222), (b) Crystallite size calculated using the Scherrer relation

5.4.5 X-ray Photoelectron Spectroscopy (XPS)

Fig. 5.9 shows the XPS spectra for the carbon 1s peaks from the interior of colloidal ITO films after 80 seconds of etching as a function of annealing temperature in air. It can be seen that the C1s XPS peaks are the highest for as coated (no anneal) film. The height of the

C1s peak decreased with annealing, and it pretty much disappeared for annealing temperatures above 300°C. A quantitative estimate of the elemental composition in atomic percent was determined based on the integral of the XPS peaks above the background [100]. The elemental composition was calculated based on the normalized peak area divided by the sum total of the peak areas of the elements being considered. As a result, presenting the elemental composition as a fraction of the total sum, when the sum total itself is varying can be misleading. The plasma treatments and annealing was not expected to cause any change in the absolute amount of indium in the films. Hence, in order to more accurately depict the changes in the amount of the elements being characterized, they are presented as a ratio of the atomic percent of the element, as calculated by the program, to the atomic percent of indium, as calculated by the program.

The variation of the content of carbon, oxygen, as a ratio of the indium content, as a function of temperature of annealing in air in the interior of the colloidal ITO films at depths achieved by etching for cumulative durations of 50 s and 80 s, is presented in Fig. 5.10 (a)-(d). It is clear from Fig. 5.10 (a) that annealing at temperatures above 300°C was able to remove a very significant portion of the residual organics, as indicated by a steep reduction in the carbon content with increase in annealing temperature. Fig. 5.10 (b) also shows that there was a significant increase in the oxygen content with an increase in the annealing temperature. This may be expected as annealing in air might cause some of the oxygen vacancies in ITO to be filled, thus increasing the oxygen content.

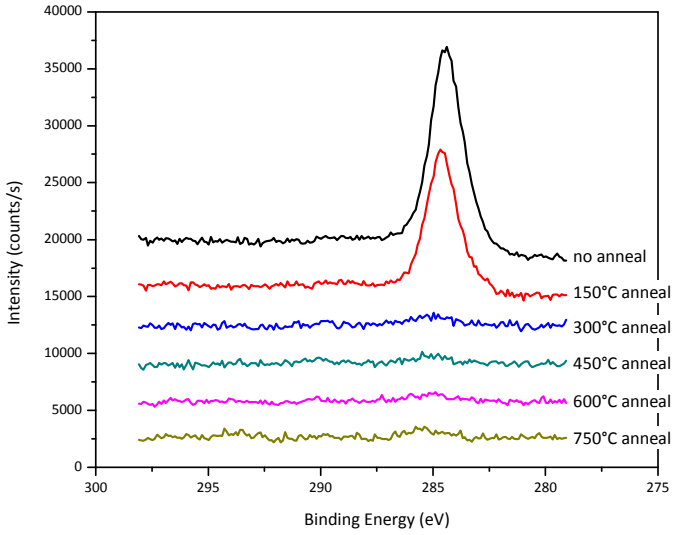

Fig. 5.9: Comparison of carbon 1s XPS after 80 seconds etching for colloidal ITO films annealed at different temperatures in air [90]

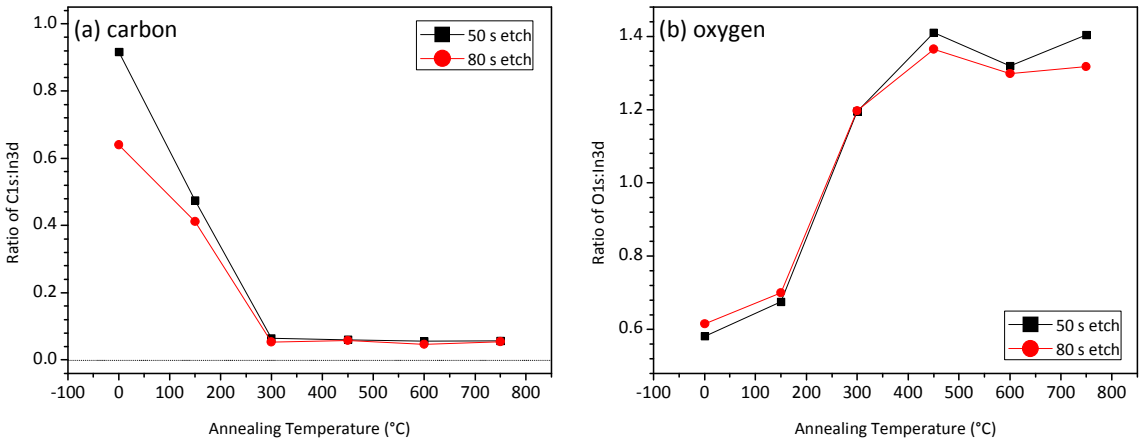

Fig. 5.10: A quantitative estimation of the variation of the elements (a) carbon, and (b) oxygen as a ratio of indium content (which is expected to be constant), within colloidal ITO films at a depth achieved by achieved by etching for 50 s and 80 s, as a function of the annealing temperature in air

5.4.6 Thermogravimetric Analysis (TGA)

The percent weight loss of dried colloidal ITO, as determined by the thermogravimetric analysis, is shown in Fig. 5.11 (a); and the corresponding rate of weight loss is shown in Fig. 5.11 (b) in both air and argon atmospheres [96]. The weight loss can

primarily be correlated to the degradation and removal of any residual solvent and organics from the colloidal ITO.

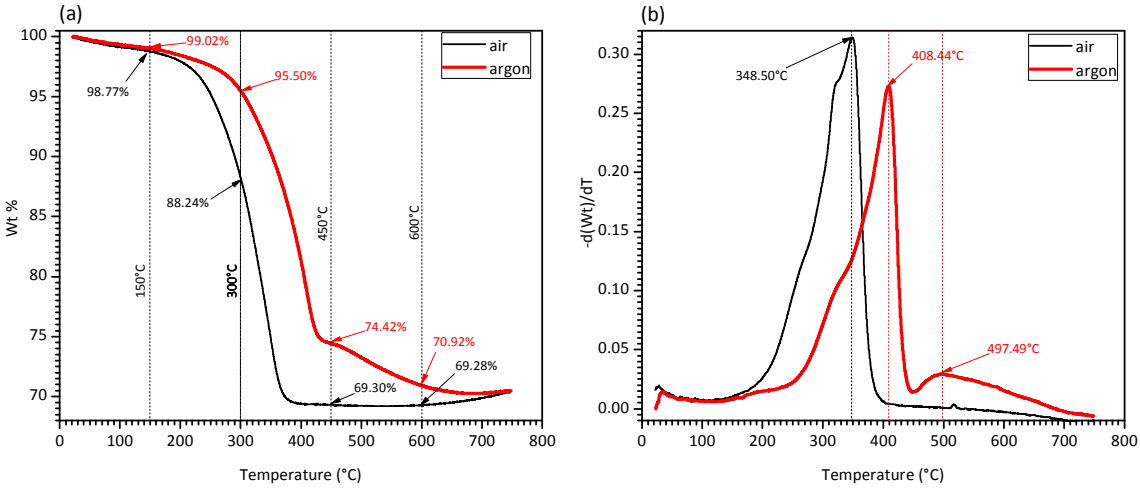

Fig. 5.11: Thermogravimetric analysis (TGA) on colloidal ITO nanoparticles after solvent removal at 90°C: (a): percent change in weight with temperature, (b): derivative of weight change with temperature [96]

At temperatures greater than 150°C, the weight loss in air is observed to be significantly higher than the corresponding weight loss upon heating in argon. The weight loss in air seems to occur in a single step, with the maximum rate of weight loss occurring at around 348.5°C, leading to a total maximum weight loss of about 30%. The weight loss upon heating in air seems to reach completion at temperatures between 350-400°C. In contrast, the weight loss upon heating in argon seems to reach completion at temperatures around 750°C. The slight uptick in the weight corresponding to a little more than 1%, seen at temperatures above 600°C in either atmosphere, could very likely be the result of an instrument error. Although the total maximum weight loss upon heating in argon is approximately identical to that in air – around 30% (see Fig. 5.11 (a)); it seems to occur in two stages, with peak rate of weight loss at 408.44°C and 497.49°C respectively (see Fig. 5.11 (b)). This indicates that annealing in argon, at temperatures greater than 600-700°C would be needed to completely remove the residual organics from patterns and films

fabricated from this colloidal ITO solution. The removal of organics could be attained at much lower temperatures while annealing in air, as described above.

5.4.7 Raman Spectroscopy

In order to get a measure of the organics present in the ITO film at different stages of the annealing heat treatments, Raman Spectroscopy experiments were conducted on selected samples. Fig. 5.12 (a), (b) show a comparison of Raman spectra of the as-coated colloidal ITO films with the spectrum of an uncoated substrate (fused silica), as well as spectra of the various organic reagents and solvents (tin acetate, indium acetate, 1-octadecene, hexane, myristic acid), that were used in the synthesis of the colloidal ITO solution, and could be potentially present in small amounts.

The spectra of the organic compounds were obtained in image or pdf format from the Spectral Database for Organic Compounds SDBS [101], maintained by the National Institute of Advanced Industrial Science and Technology (AIST), Japan, and product Raman spectra from Sigma Aldrich Chemical Company [102]. These were converted to digital form using an open-source software, Plot Digitizer [103]. The smaller Raman shifts, below 1100 cm^{-1} are dominated by scattering from the fused silica substrate, and what appears to be Rayleigh scattering that was not completely filtered out. The peaks in the 2800-3000 cm^{-1} correspond to scattering from the $-CH_2$ and $-CH_3$ bonds [104]; and are common to most organic compounds. These peaks are prominent in the Raman spectra of the as-coated films. Myristic acid is not only expected to be present as passivating ligands on the surface of the nanoparticles, but also in the form of some excess free myristic acid that could not be completely removed during extraction. The spectra indicate possible peaks from 1-octadecene, which was used during the synthesis [4, 90] as a high boiling point, non-polar solvent. It was subsequently removed by precipitating the nanoparticles using standard

polar/non-polar solvent techniques [91]. However, the presence of Raman peaks indicates that perhaps some residual 1-octadecene may have persisted. This is significant because 1-octadecene has a boiling point of 315°C [105]; and the residual amounts of 1-octadecene would not have been able to be removed by the lower temperature treatments.

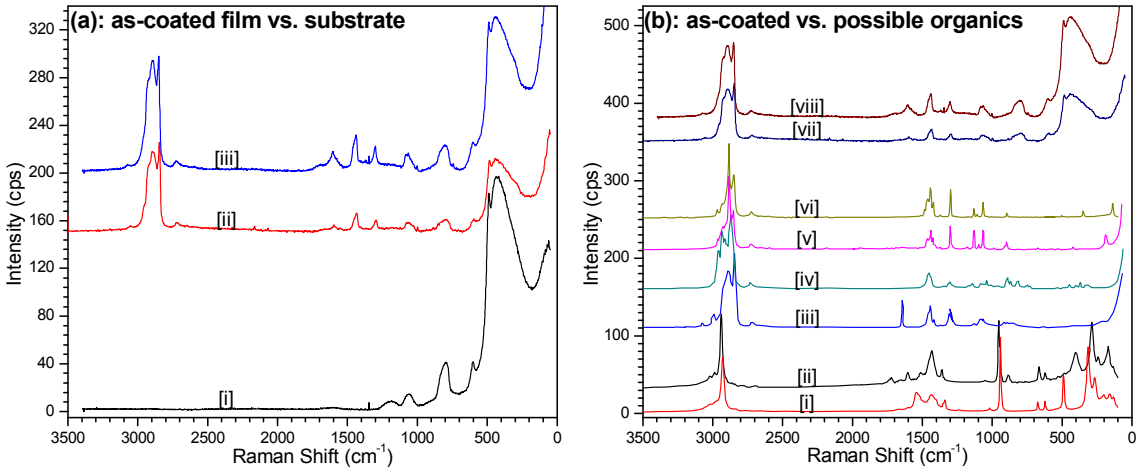

Fig. 5.12: Comparison of Raman spectra of non-annealed colloidal ITO films with (a) substrate, (b): possible organic compounds present residually in the as-prepared colloidal ITO solution. Spectra in (a) are : (i) fused silica substrate, (ii) non-annealed 1, (iii) non-annealed 2. Spectra in (b) are: (i) tin acetate, (ii) indium acetate hydrate, (iii) 1-octadecene, (iv) hexane, (v) myristic acid, (vi) 1-octadecanol, (vii) as-coated-1, (viii) as-coated-2 [96]

Fig. 5.13 (a), (b) present a comparison of Raman spectra of films annealed at 300°C and 600°C in air and argon respectively with that of as-coated colloidal ITO film. It can be seen that the peaks corresponding to $-CH_2$ and $-CH_3$ progressively decrease with an increase in annealing temperature. A comparison of the Raman spectra of films annealed at 300°C in air and in argon indicates a stark difference [96]. The film annealed in air shows significantly lower signals from organics as compared to the film annealed in argon, which not only shows a broad peak in the 2800-3200 cm^{-1} range, which corresponds to $-CH_2$ and $-CH_3$, but also broad peaks in the 1200-1800 cm^{-1} range, which indicates the presence of amorphous carbon [106, 107].

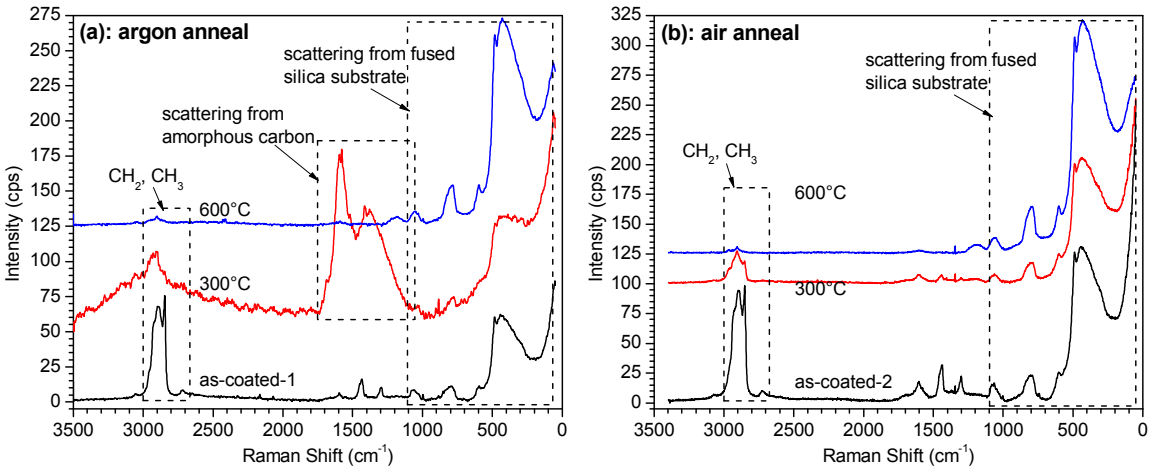

Fig. 5.13: Comparison of Raman spectra of as-coated colloidal ITO films with those of (a): ITO films annealed in argon at 300°C and 600°C, (b): ITO films annealed in air at 300°C and 600°C [96]

The Raman spectra of films annealed in either atmosphere at 600°C appear very similar. (See Fig. 5.13 (a) and (b).) Apart from very faint scattering signal from CH_2 and CH_3 groups, the Raman spectra show very little signal from any organics. These spectra are dominated by scattering from the fused silica substrate. This corroborates with the TGA result that upon heating to 600°C and beyond in either air or in argon, most of the residual organics are removed.

5.4.8 Electrical Characterization

As described in chapter 3, impedance spectroscopy was used to measure the electrical response of the ITO thin films. Representative Bode plots depicting the variation of impedance magnitude and the impedance phase angle as a function of frequency are shown in Fig. 5.14 for colloidal ITO films annealed at various temperatures in air (Fig. 5.14 (a)) and argon atmospheres (Fig. 5.14 (b)) respectively. It can be seen that the as-coated ITO film, and the films annealed at 150°C are very resistive. The films get less resistive with increasing annealing temperatures, showing about eight orders of magnitude decrease and the appearance of a plateau on the $|Z^*|$ vs. f graph, plotted using a log-log scale.

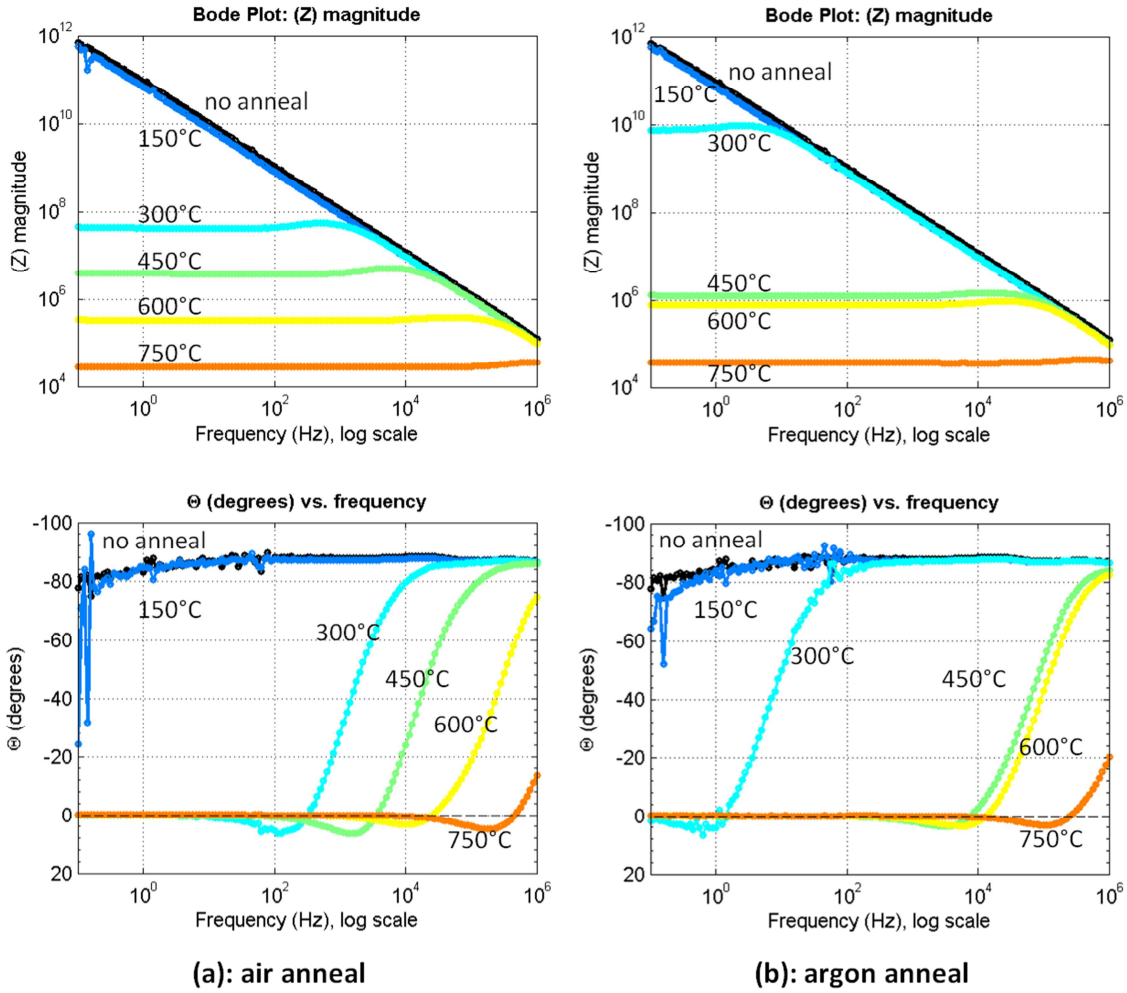

Fig. 5.14: Representative Bode plots showing a comparison [96] of the impedance magnitude and phase angles for colloidal ITO films annealed at different temperatures in (a) air, (b) argon

The phase angle (θ) indicates the overall nature of the electrical behavior at a particular signal frequency [75]. A phase angle close to zero indicates a dominantly resistive behavior, a phase angle between zero and –90° indicates a resistive-capacitive (RC) behavior, with the behavior being purely capacitive when the phase angle is –90°. Similarly, a phase angle between zero and +90° indicates a resistive-inductive (RL) behavior, with the behavior being purely inductive at a phase angle of +90°. It can be seen from the plots of phase angle vs. frequency in Fig. 5.14 (a) and (b) that the general behavior of the colloidal ITO films could be described as almost purely capacitive at high frequencies, transitioning

through RC behavior, a short frequency window of RL behavior in the mid-frequency range, and settling into a purely resistive behavior at low frequencies.

It can also be seen that with increasing annealing temperatures, not only does the dc impedance magnitude decrease by many orders of magnitude, the transition from a capacitive to a resistive behavior occurs at relatively high frequencies. One can argue that since the capacitive impedance varies inversely with the signal frequency, charge transfer is dominated by the capacitive mode for those frequencies where the capacitive impedance is significantly less than the resistance. Hence, for films with lower dc impedance magnitude, the transition from capacitive to resistive behavior occurs at higher frequencies and vice versa.

Fig. 5.15 displays the variation of the sheet resistance of the colloidal films deposited onto fused quartz and glass substrates, as a function of annealing. It can be seen that the resistivity is a strong function of the annealing temperature. Irrespective of the annealing atmosphere or the substrate, the film resistivity dropped by more than eight orders of magnitude after annealing at 750°C. The annealing atmosphere and the substrate were also found to affect changes in resistivity, although to a relatively smaller extent.

It can be seen that annealing at 300°C in the oxidizing atmosphere of air is more effective than annealing at 300°C in the argon atmosphere in reducing the film resistivity. According to the accepted defect model of ITO [19, 108, 109], reducing treatments increase carrier concentration by increasing the oxygen vacancy concentration, while oxidizing treatments reduce carrier concentration by decreasing the oxygen vacancy concentration. However, the fact that a 300°C anneal in air is more effective at reducing the film resistivity than a 300°C anneal in argon suggests that air annealing results in more efficient removal of the residual organics upon heating in air, as compared to heating in argon that may be

responsible for this discrepancy. The TGA and Raman spectroscopy results, which were discussed in the previous sub-sections, support this conclusion. Thus, the variation in the resistivity of the colloidal ITO films was seen to be primarily dominated by two parameters: ligand removal treatment and the annealing temperature. The changes in carrier concentration that may have been caused by the choice of annealing atmosphere were far outweighed by the improvement of the electrical contact between the nanoparticles, i.e. a decrease in electron scattering.

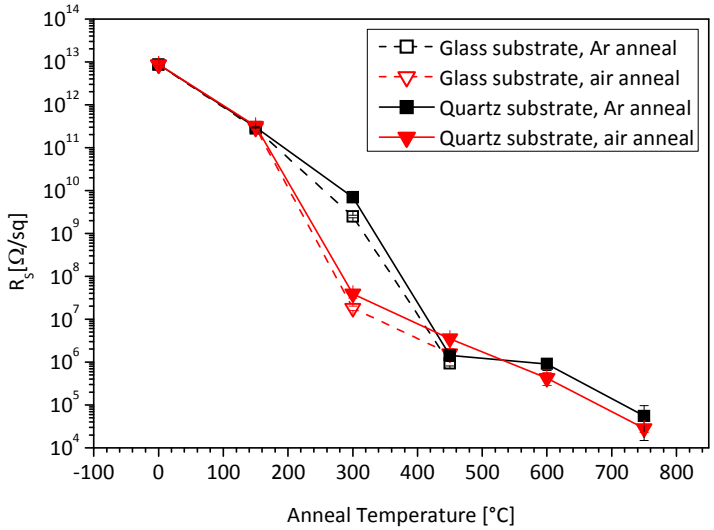

Fig. 5.15: Sheet resistance of colloidal ITO films as a function of annealing temperature, annealing atmosphere and film substrate [96]

A comparison of the plots of the sheet resistance of the ITO films with respect to the substrates used suggests that the nature of the substrate also affects the resistivity of the films somewhat. For films annealed at temperatures of 300°C and higher, the films on glass substrates have lower resistivity than films on quartz substrates. This may be attributed to the big difference in the thermal expansion coefficients of ITO, which has an expansion coefficient of 8.5×10^{-6}/°C [110], and fused quartz, which has an expansion coefficient of 0.55×10^{-6} /°C [111]. This difference in the expansion coefficients could have resulted in

the development of micro-cracks upon heating and cooling. The effect of the nature of the substrate on the electrical properties of ITO films is presented in more detail in the appendix, in a study involving cold-sputtered films [112].

5.4.9 Discussion

Fig. 5.16 (a) shows a schematic of an as-deposited colloidal ITO film made from nanoparticles. The presence of insulating organics and voids in the ITO film suggests that the spin coated ITO thin films can be considered as a composite consisting of conducting ITO nanoparticle islands embedded in an insulating phase of organics and voids. Annealing at a temperature that is less than the temperature needed for a complete removal of organics would naturally result in only a partial removal of the organics, at best. This is especially manifested in the colloidal films annealed in argon at 300°C. Raman characterization indicates the presence of significant amounts of amorphous carbon, which was likely produced as a result of incomplete pyrolysis of the organics. The resulting microstructure can be schematically represented by Fig. 5.16 (b), which shows some limited electrical contact between the nanoparticles, but at the same time, separation of the nanoparticles by an amorphous organic or a partially pyrolyzed carbonaceous phase. This microstructure not only results in high resistivity, but also a significantly reduced transmittance in the visible region. In comparison, the films annealed at 300°C in air have a greater extent of carbon removal, as evidenced from the TGA and Raman characterization. This resulted in the resistivity being more than 2-3 orders of magnitude lower than for films annealed at the same temperature in argon, as seen previously in Fig. 5.15.

As can be inferred from the TGA data, the removal of organic content increases with an increase in the annealing temperature, during annealing in either atmosphere. The removal of the organics and reduction of porosity through the densification process has the

effect of increasing the proportion of the conducting phase in this "composite" film. Fig. 5.16 (c) shows a schematic of the expected microstructure of the colloidal film, when all or most of the organics have been removed. In this case, the ITO nanoparticles would be in contact with each other; and resulting in a much lower resistivity than when organic phases are present in a significant proportion to hinder electrical percolation. Although the ITO nanoparticles are in contact with each other, the sheet resistance of the film is not reduced all the way close to that of bulk ITO. For comparison, commercially available sputtered ITO films of comparable thickness may have a sheet resistance of 30-60 Ω/sq [113]. The difference in the sheet resistance in our colloidal ITO films is likely due to non-ideal contact between the nanoparticles and due to the increased scattering due to the nano-sized crystallites.

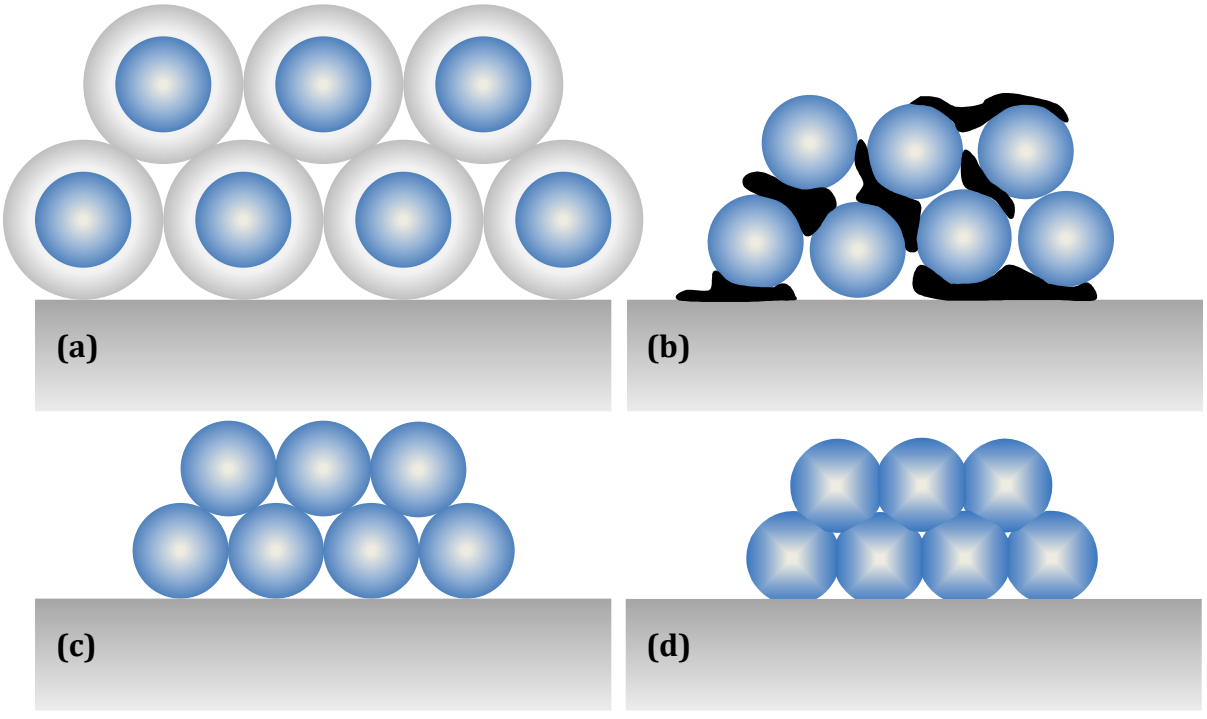

Fig. 5.16: Schematic of microstructural changes in the colloidal ITO films with annealing (not to scale) (modified from [96]):(a) colloidal ITO particles covered with passivating organics in the as-coated film, (b) colloidal particles with partially pyrolyzed organics (observed during argon annealing), (c) colloidal particles with organics removed, (d) partially sintered colloidal particles

Low temperature annealing is expected to result in very little sintering between the nanoparticles resulting in a non-optimal contact between them. This is supported by the previously discussed Scherrer particle size analysis [90], which showed that the nanoparticles do not change size at all in the temperature range studied, except for the very minor changes after the 750°C treatment. The nano-porosities that are present between the nanoparticles act as an insulating phase, and therefore limit the charge transfer between the conducting ITO nanoparticles. Annealing at higher temperatures is expected to cause some densification resulting from necking between the particles. This is schematically represented in Fig. 5.16 (d). Thus, annealing at even higher temperatures results in a lowering of resistivity due to progressive densification of the nanoparticulate film.

As a result of all these factors, the sheet resistance vs. annealing temperature curve shows 8-9 orders of magnitude reduction in resistivity over the temperature range studied, which are comparable to percolation curves as a function of the volume fraction of conductive phase in composites such as metal-polymer composites and others [114]. In fact, for both, the air and argon annealed ITO spin-coated films, the sheet resistance achieved was on the order of 10^4 Ω/sq, which was arrived at via oxidation and pyrolysis respectively. This was supported by the Raman spectra and TGA which indicated that the removal of organics is more efficient at lower temperatures in the oxidative atmosphere of air as compared to the low oxygen partial pressure atmosphere of argon. Although annealing in the low oxygen partial pressure of argon might have marginally increased the carrier concentration by the process described earlier, the reduction of scattering as a result of removal of organics and partial densification has a far more dominant effect in reducing the resistivity of the colloidal ITO films.

5.5 Conclusions

Although ITO is a good electrical conductor, colloidal ITO films are very resistive in the as-deposited condition due to the lack of good inter-particle contact as a result of the presence of a coating of stabilizing organic phases that are very insulating. Annealing at a high temperature is the simplest way to decrease or remove these organics and also help induce coalescence and densification. Annealing at high temperatures can significantly decrease the sheet resistance of colloidal ITO thin films by over 8-9 orders of magnitude by establishing electrical percolating paths between the nanoparticles and also by reducing electron scattering via inter-particle necking and densification. However, sufficiently low resistivity to be practical for flexible electronic applications cannot be achieved by conventional low temperature annealing alone and other treatments must be considered.

Chapter 6:
Effect of Plasma Processing

6.1 Introduction

It was shown in chapter 5 that oxidation in air was more effective at reducing the residual organics, and also lowered the ITO film resistivity at relatively lower temperatures than pyrolyzing the organics in an inert atmosphere. This suggests that it might be possible to remove the residual organics in the films at a lower temperature or at room temperature by using more reactive oxidizing species, such as those present in oxygen plasma. This idea is supported by some preliminary work done by Gehl, et al. [115] on discontinuous regions of organic capped nanoparticle monolayers, which shows that it may be possible to remove the organic capping layers from such nanoparticle layers using plasma processing. Since it was not possible to do plasma treatments with concurrent heating due to equipment limitations, the effect of plasma treatments done at room temperature, and the effect of plasma treatments done with and without subsequent annealing were studied. Colloidal ITO films were fabricated as described in chapter 3. This chapter describes the procedure and the effects of various plasma treatments (reactive ion etching, RIE) done with and without annealing treatments on the colloidal ITO films.

6.2 Plasma Study 1: Initial exploratory experiments

6.2.1 Plasma Treatments

Two plasma treatment recipes were tried out in the first part of the study – one was a standard ashing recipe using an oxygen plasma cleaner, which is commonly used to remove residual photoresists. This was compared with a second, customized recipe

intended to gently remove the organic layers and prevent ITO stoichiometry from becoming too oxygen rich in the process. The two ligand removal treatments utilized were as follows:

(i) **O_2 plasma cleaning:** O_2 plasma treatment was done using YES-R1 oxygen plasma cleaner for 6 minutes at a pressure of 1.6 Torr, using a power of 670-690 W. The maximum temperature generated during this treatment was estimated using temperature recording labels (Palmer Wahl Instrumentation Group), and was determined to have been between 65-93°C.

(ii) **O_2–Ar RIE x5:** Alternating treatments of reactive ion etching (RIE) in oxygen and argon atmospheres were conducted using a Plasma-Therm Reactive Ion Etcher. Five repetitions of this treatment were done. The oxygen plasma cycle was done at 40 W, 500 mTorr for 5 minutes; and the argon plasma cycle was done at 30 W, 500 mTorr for 1 minute. The plasma did not strike in the last oxygen plasma cycle, essentially resulting in 4 sets of alternating oxygen and argon plasma cycles followed by an additional argon plasma cycle. The plasma treatment parameters for this treatment were chosen so that relatively high gas pressure and low plasma power were used during the treatment, in order to keep the etching non directional and to allow the reactive species in the plasma to be able to reach the ligand covered surfaces of the nanoparticles in the lower layers. In addition, it was also expected that the changes in the ITO oxygen stoichiometry caused by the oxygen plasma, which could result in a decrease in carrier concentration, would be partially reversed by periodically having a small argon plasma cycle, rather than having a single continuous O_2 RIE cycle. Five cycles of RIE in oxygen followed by RIE in argon were used to compensate for the fact that RIE was being done at low power.

6.2.2 Post-plasma treatment annealing

In addition to studying the effect of plasma treatments described above, the effect of subsequent annealing in air and argon atmospheres were also studied. The annealing of colloidal ITO films was done as described in chapter 5 using an alumina tube furnace, at various temperatures: 150°C, 300°C, 450°C, 600°C and 750°C for 48 minutes. The annealing was done in an atmosphere of ultra-zero grade commercial air (Airgas) or UHP grade argon (Airgas) flowing through the furnace tube.

6.2.3 Characterization

The films fabricated and processed in the manner described above were characterized in terms of their physical appearance, and by the following techniques. The in-plane electrical properties of the films were determined using impedance spectroscopy based techniques described in chapter 3. X-ray photoelectron spectroscopy (XPS) depth profile scans were also conducted on these ITO films to compare the ligand removal effectiveness of the plasma treatments used. The procedure for doing XPS depth profile scans was described in chapter 5.

6.2.4 Results and Discussion

6.2.4.1 Appearance

The appearance of the colloidal ITO films fabricated and processed as described above is shown in Fig. 6.1. The as-prepared films, as well as the annealed films are all transparent and crack free. Colloidal films annealed in argon at 300°C are an exception to this, irrespective of whether or not they were subjected to any the ligand removal pre-treatments or not. As described in chapter 5, the browning that occurs in some of these films indicates incomplete pyrolysis, and that the plasma treatments described above were not able to completely remove the residual organics in the films.

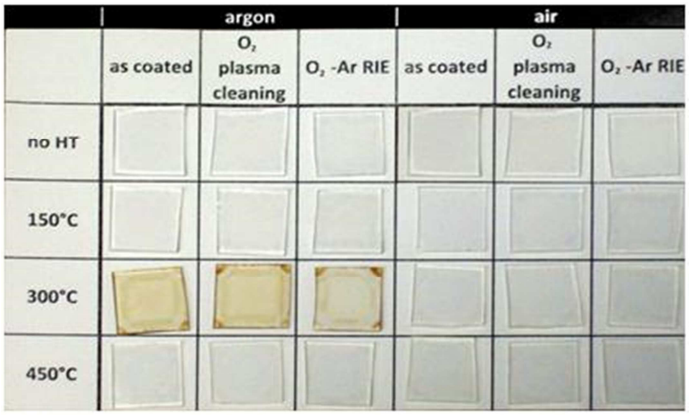

Fig. 6.1: Visual appearance of spin coated colloidal ITO films vs. heat treatment and/or plasma treatment [90]

6.2.4.2 X-ray Photoelectron Spectroscopy (XPS)

Fig. 6.2 shows the variation of carbon 1*s* XPS spectra with various etch times for ITO films in the spin coated state, and after the two plasma treatments described above. Since all the films are similar in composition, in that they primarily contain ITO, we can assume equal sputtering etch rates for all the films. Thus, for these samples, equal etch times correspond to equal depths in the film undergoing XPS characterization. It can be seen that for all films, the C1*s* signal seems to be stronger at the surface; and it levels off to a relatively steady peak height in the interior. The stronger C1*s* signals on the surface could be attributed to the adsorption of various species on the film surface that may have happened during storage. A comparison of the residual carbon content in the interior of these films is more apparent on comparing the carbon 1*s* XPS spectra after 80 seconds of etching for the conditions evaluated is shown in Fig. 6.3. A strong carbon 1*s* peak can be seen in the XPS spectrum of the as-coated colloidal ITO film, indicating the presence of organic ligands. The films subjected to the plasma treatments had significantly reduced peaks, indicating removal of organics. For quantitative comparison, the atomic percent of carbon and oxygen was determined based on the integral of the respective XPS signals [100], and presented as a ratio of indium content, as discussed in chapter 5.

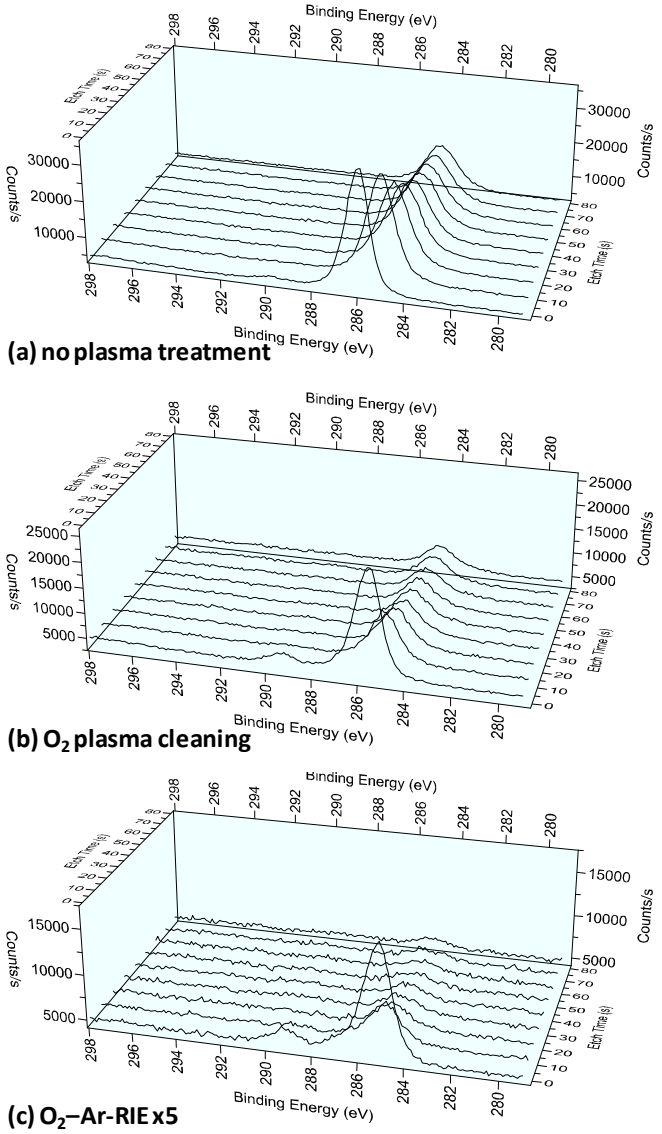

Fig. 6.2: Variation of carbon 1*s* XPS spectra with various etch times for ITO films (plasma study 1): (a) as spin coated (no plasma treatment), (b) after O_2 plasma cleaning (ashing), (c) after O_2–Ar RIE x5 plasma treatment. (Note the difference in scale on the Y-axis.)

A comparison of the carbon and oxygen content as a ratio of indium content, at a couple of depths in the film achieved by etching for a cumulative 50 s and 80 s is presented in Fig. 6.4. It can be seen that the plasma treatments caused a significant decrease in the amount of carbon in the interior of the films, with the composite plasma treatment (O_2–Ar RIE x5) being more effective than O_2 plasma cleaning alone in removing the residual

organics. However, neither of the plasma treatments reported here was able to completely remove all of the residual organics from the films. Further optimization of the plasma treatment is necessary to therefore completely remove the residual organics from such films.

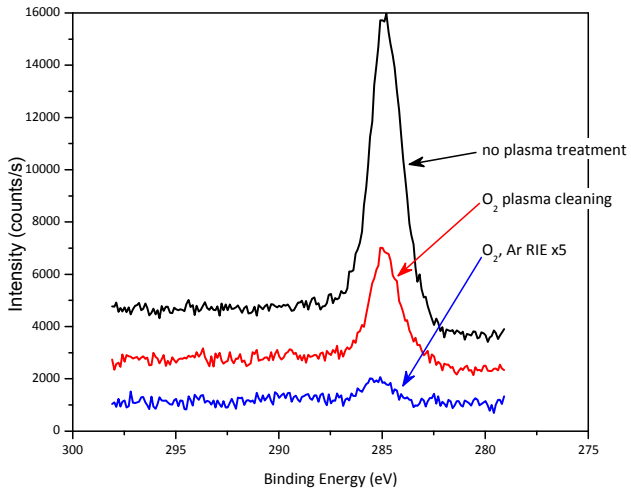

Fig. 6.3: Comparison of carbon 1*s* X-ray photoelectron spectra after 80 seconds etching as a function of plasma treatment on colloidal ITO films [90]

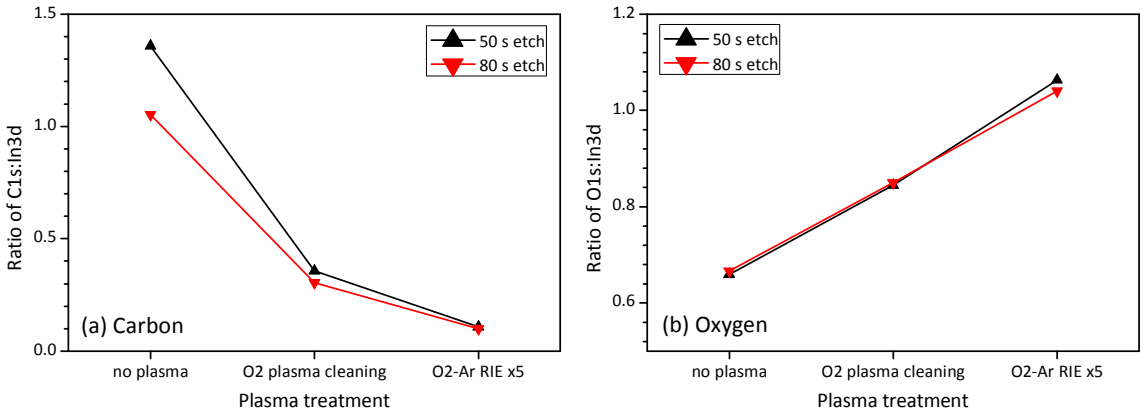

Fig. 6.4: Comparison of carbon and oxygen content as a ratio of indium content, in the interior of colloidal ITO films (depths achieved by etching for a cumulative 50 s and 80 s), as a function of the plasma treatment used

6.2.4.3 Electrical Properties

Fig. 6.5 (a)-(d) show representative Bode plots depicting the variation of impedance magnitude and phase angle (θ), as well as the real (Z') and imaginary (Z'') parts of impedance over the measured range of 0.1 Hz – 10^6 Hz. The impedance behavior in general was similar to those described in chapter 5. The films show a prominent RC behavior at high frequencies, as manifested in the negative phase angles. They transition through a small frequency window of RL behavior, which is seen as a small window of positive phase angles, before settling into a resistive behavior at low frequencies, which is indicated by near zero phase angles. The Bode plot of the imaginary part of impedance also reflects this behavior. The impedance magnitude and the real part of impedance steadily increase with decreasing frequency, and flatten out at lower frequencies.

The film sheet resistance was calculated from the magnitude of low frequency impedance, as described in chapter 4. The variation of sheet resistance of the film after the two plasma treatments described has been compared in Fig. 6.6 with that of the as-coated ITO film. As discussed in chapters 4 and 5, the as-coated films are highly insulating due to poor inter-particle contact and due to the insulating organic capping layer surrounding each nanoparticle, which essentially results in a composite microstructure consisting of discontinuous conducting ITO islands distributed in a continuous insulating phase, as depicted in Fig. 5.16 (a). A complete or a partial removal of the organic coating can be expected to result in percolation [114] of the conducting phase; and thus result in a significant decrease in resistivity. Oxygen plasma cleaning was able to reduce the sheet resistance of the films by almost four orders of magnitude without any external heating. The more complex O_2-Ar RIE x5 treatment was able to reduce the sheet resistance even further – from a very high 10^{13} Ω/sq for the as-deposited films to less than 10^8 Ω/sq. This is consistent with the XPS results presented in the previous sub-section, which show that the

two plasma treatments significantly reduced the carbon content, which can be directly correlated to the residual organics content. Furthermore, the Ar-O_2 RIE x5 treatment decreased the carbon content to a greater extent than the O_2 plasma cleaning (ashing). In addition, since the O_2 plasma cleaning, done by itself, is very oxidizing in nature, it could have potentially resulted in a decrease in the oxygen vacancy concentration. According to the current understanding of the defect structure of ITO, which has been studied and modeled by Frank and Köstlin [18], González et al. [19] and others [17, 21-24], this can result in a decrease in the carrier concentration and lead to higher sheet resistance.

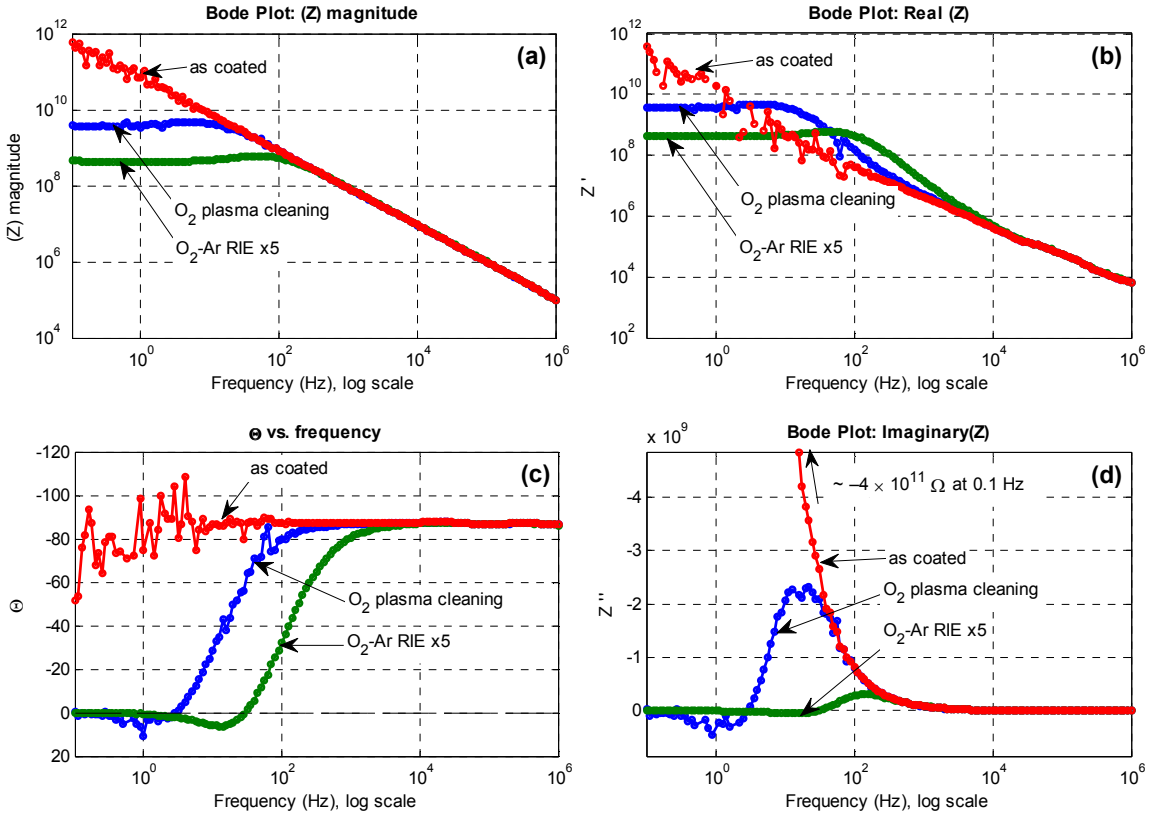

Fig. 6.5: Representative Bode plots (plasma study 1) showing variation with measurement frequency for (a) impedance magnitude, $|Z^*|$, (b) real part of impedance, Z', (c) impedance phase angle, θ, (d) imaginary part of impedance, Z''

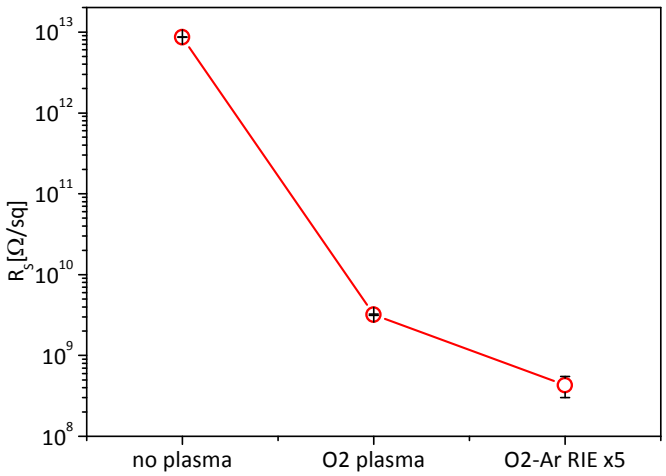

Fig. 6.6: Comparison of sheet resistance of ITO films after plasma treatment (plasma study 1) to that of as-coated ITO films

Fig. 6.7 (a)–(d) show a comparison of the sheet resistance with and without plasma treatment followed by post-annealing as a function of annealing temperature, for films deposited on glass and fused quartz substrates, as well as for air and argon annealing atmospheres. The behavior of the ITO films on glass and fused quartz substrates was nearly identical, but differences could be discerned for films annealed in air versus those annealed in argon. These graphs show that plasma treatment prior to annealing helps to further reduce the film resistivity to lower values by multiple orders of magnitude than in similarly annealed samples, but without plasma pre-treatment. However, this significant reduction in resistivity is only observed for non-annealed films and for films annealed to 150°C in air, and for films annealed at 150°C and 300°C in argon. For films annealed at temperatures higher than these in the respective atmospheres, the difference in the resistivities was not as significant – less than an order of magnitude. In general, the films subjected to oxygen plasma cleaning had a slightly higher resistivity than the non-plasma treated films, whereas the films treated with the O_2–Ar RIE x5 treatment had even lower resistivity than the non-plasma treated films.

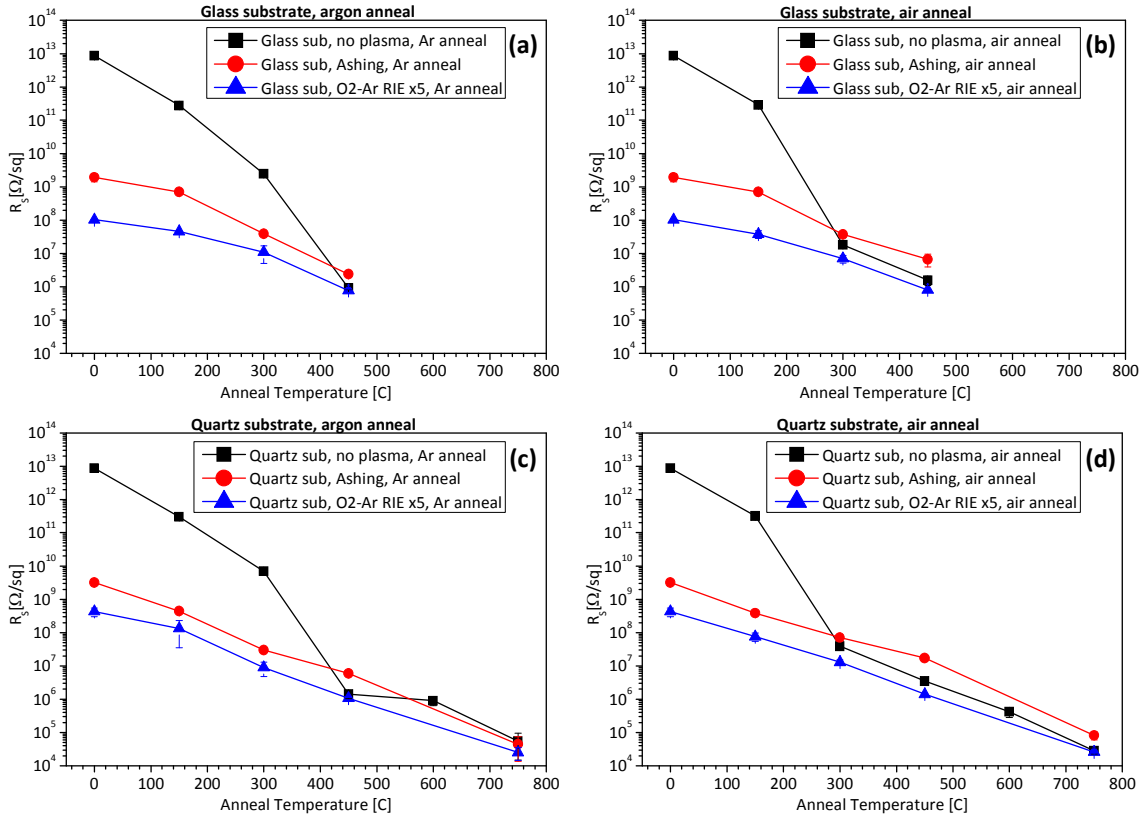

Fig. 6.7: Variation of sheet resistance of colloidal ITO films with annealing temperature, for ITO films with and without plasma treatments: (a) on glass substrate, argon annealing, (b) glass substrate, air annealing, (c) fused quartz substrate, argon annealing, (d) fused quartz substrate, air annealing

The results of TGA and Raman spectroscopy of dried colloidal ITO nanoparticles, done in air and argon atmospheres were presented in chapter 5. On comparing these results with the variation of sheet resistance shown in Fig. 6.7 (a)-(d), it can be deduced that for the annealing conditions listed above, which did not show a significant reduction in resistivity with a pre-annealing plasma treatment, the annealing by itself is able to remove all or most of the residual organics content by itself; whereas for the annealing conditions which showed a significant resistivity reduction with a pre-annealing plasma treatment, annealing by itself is not able to remove sufficient amount of residual organics from the ITO films. This

underscores the importance of removal of the residual organics in order to reduce the sheet resistance of the ITO films.

6.3 Plasma Study 2: Effect of recipe parameters

The discussion in the previous section showed that the multi-cycle treatment in oxygen and argon plasma described above was significantly more effective than the ashing treatment in reducing the proportion of residual organics in the colloidal films, as well as reducing the film resistivity at relatively low temperatures. Hence, in order to investigate the effect of various parameters of the plasma treatment recipe, parameters such as oxygen and argon partial pressures, plasma power and number of cycles was varied. This was investigated using a matrix of seven plasma treatment recipes. A series of colloidal ITO films were spin-coated on glass substrates, and were subjected to various plasma treatment recipes, consisting of alternating RIE treatments in oxygen and argon. The general form of the plasma treatment recipes used in this study is shown in Fig. 6.8.

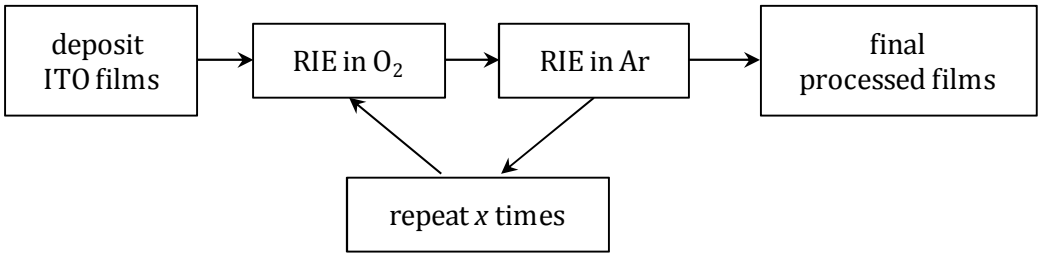

Fig. 6.8: General plasma treatment recipe used in Plasma Study 2

The parameters used in the specific recipes utilized are outlined in Table 6.1. Recipe #1 was chosen to have parameters identical to the O_2–Ar RIE x5 plasma treatment in plasma study 1. However, during O_2-Ar RIE x5 treatment described in plasma study 1, plasma had not struck during the last O_2 RIE cycle. So, essentially, recipe #1 had an additional O_2 RIE cycle as compared to the O_2–Ar RIE x5 treatment described earlier.

Table 6.1: Plasma treatment matrix (Plasma Study 2)

Recipe	O_2 pressure (mTorr)	O_2 power	O_2 time (minutes)	Ar pressure (mTorr)	Ar power	Ar time (minutes)	No. of cycles
#1	500	40	5	500	30	1	5
#2	250	40	5	250	30	1	5
#3	250	80	5	250	30	1	5
#4	500	40	5	500	30	1	20
#5	250	40	5	250	30	1	20
#6	250	80	5	250	30	1	20
#7	250	80	5	250	30	1	10

6.3.1 Characterization

The characterization of the films fabricated and processed in the manner described above was done by XPS depth profile scans and by impedance spectroscopy. These techniques and the method for the calculation of film sheet resistance from the impedance data have been described in previous chapters.

6.3.2 Results and Discussion

6.3.2.1 X-ray Photoelectron Spectroscopy (XPS)

The effectiveness of the plasma treatments in removing the residual organics was characterized by comparing the carbon 1*s* XPS signals from the interior of the film. XPS depth profile scans were performed on the films as described in chapter 5, except that the etching for depth profile was done in steps of 15 s. Nine etch levels were scanned, which makes a total of 135 s of etching for the deepest level. The relative amounts of residual organics in the interior of the films were determined by comparing the C1*s* scans after etching for 75 s. These are presented in Fig. 6.9. It can be seen that the film without any plasma treatment shows a prominent peak corresponding to C1*s*, while all the plasma

treated films do not display any C1*s* peak at all. The XPS scans for In3*d* and Sn3*d* done at the same time show distinct peaks at the expected binding energies for each of these films. For an example of this, see Fig. 6.10, where a comparison of the C1*s* and In3*d* depth profile scans for colloidal ITO films after undergoing plasma treatment recipe #1 is shown. Hence, the low XPS signal for C1s cannot be explained by a possible case of non-optimal focusing or incorrect XPS technique. However, on comparing the C1*s* scan of recipe #1 in Fig. 6.9 with the C1*s* of the O_2–Ar RIE x5 in Fig. 6.2 (c), we see a disparity because although the two treatments were very similar, the C1*s* scans are not the same. We see a weak C1*s* peak for O_2–Ar RIE x5 in Fig. 6.2 (c), whereas in Fig. 6.10, no C1*s* is seen for recipe #1. As shown later, electrical characterization allowed us to distinguish between the effectiveness in removing residual organics for the different recipes used in plasma study 2. Since the XPS characterization for these samples could only be done after an unintended lengthy waiting period, a possible degradation of the film could be partially responsible for this discrepancy. XPS characterization is discussed in more detail in the next section.

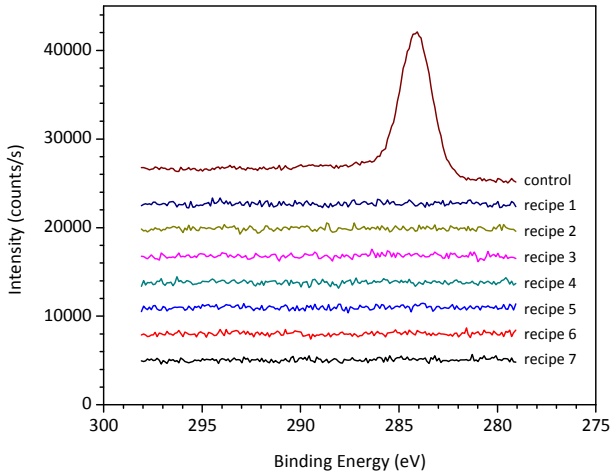

Fig. 6.9: Comparison (plasma study 2) of carbon 1*s* X-ray photoelectron spectra after 75 seconds etching as a function of plasma treatment on colloidal ITO films

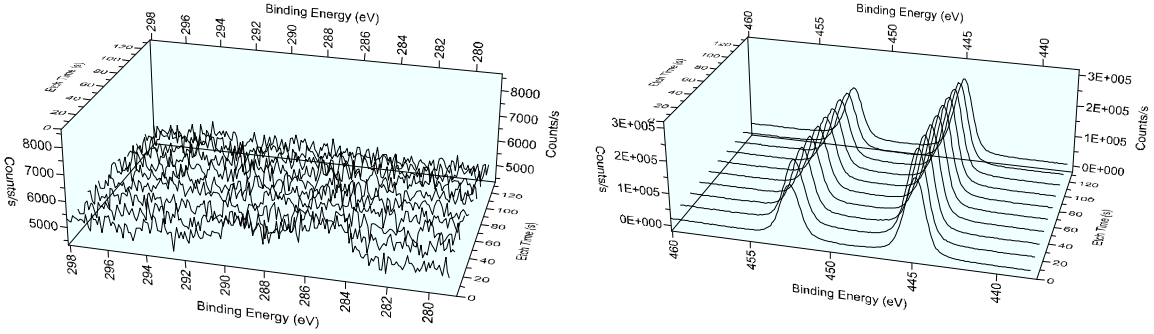

(a) C1*s* scan **(b) In3*d* scan**

Fig. 6.10: Comparison of the XPS depth profile scans for C1*s* and In3*d*, taken at the same location, of colloidal ITO film plasma treated with recipe #1

6.3.2.2 Electrical Properties

Fig. 6.11 (a) shows representative Bode plots of the impedance magnitude ($|Z^*|$ vs. f on the log-log plot), of the colloidal ITO films in plasma study 2. Fig. 6.11 (b)-(d) present representative Nyquist plots (polar plots of complex impedance, i.e. Z'' vs. Z') for the same films. Three separate plots, using different scales are shown because of the big differences in the measured impedance values. It can immediately be seen that recipe #1 and recipe #4 resulted in the maximum reduction of resistances as compared to the response of the as spin-coated film. Most of these Nyquist plots show some RC and RL behavior similar to the impedance spectra presented in previous chapters. The impedance spectra will be discussed and analyzed in more detail in the next chapter.

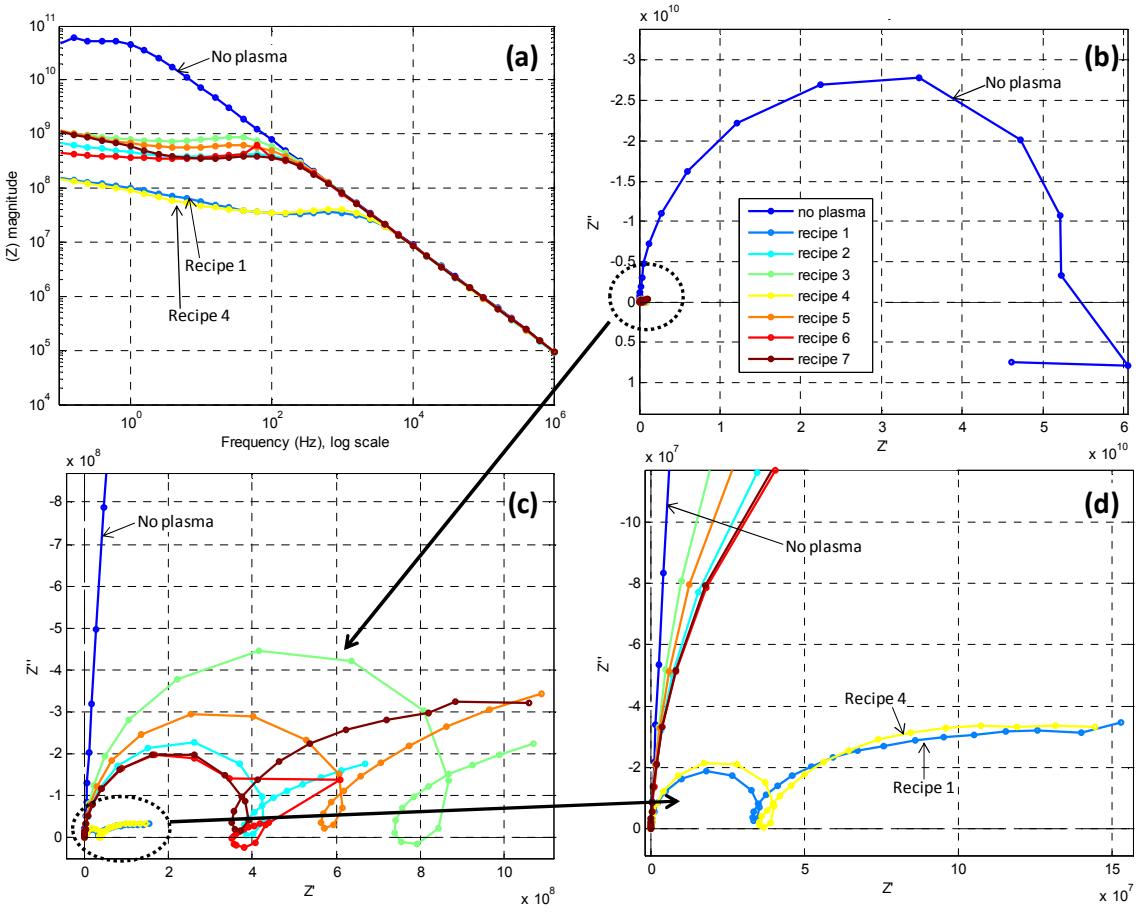

Fig. 6.11: (a) Bode plots of impedance magnitude for films in plasma Study 2, (b)-(d) Nyquist plots of impedance for films in plasma Study 2, shown at different magnifications to highlight the differences between the different recipes

Fig. 6.12 shows the variation of the sheet resistance of colloidal ITO films with the number of alternating oxygen and argon RIE cycles. It can be seen that beyond 5 cycles, the number of cycles did not make any difference to the sheet resistance. It should also be noted that there is not much difference in the curves for RIE done at 250 mTorr at 40W and 80W. In the range of plasma power studied, and for the other parameters mentioned earlier, the plasma power also does not seem to have a significant effect on the sheet resistance of the plasma treated film. However, for the same plasma power and number of cycles, plasma pressure seems to have a significant effect. The effect of pressure is more clearly presented in Fig. 6.13, which shows the variation of the sheet resistance of the ITO films as a function

of the plasma pressures used during RIE. The ionization efficiency in an electric field induced plasma, such as in a non-magnetron sputtering machine, or during RIE has been shown to vary almost linearly with pressure [116]. This, together with the fact that at higher pressure, there are more molecules (or atoms in case of noble gases) per unit volume that could be ionized, suggests that the concentration of active species per unit volume in a plasma increases very significantly with an increase in pressure. Additionally, the relatively shorter mean free path at higher pressures also helps the active species diffuse through the inter-particle gaps down to the capped nanoparticles in the lower layers of the film, which would result in a more thorough ligand removal throughout the thickness of the film. For the general plasma treatment recipe, consisting of alternating RIE in oxygen and argon used in this study, suggests that pressure may be a very important factor in determining the ligand removal efficiency of this multi-cycle process.

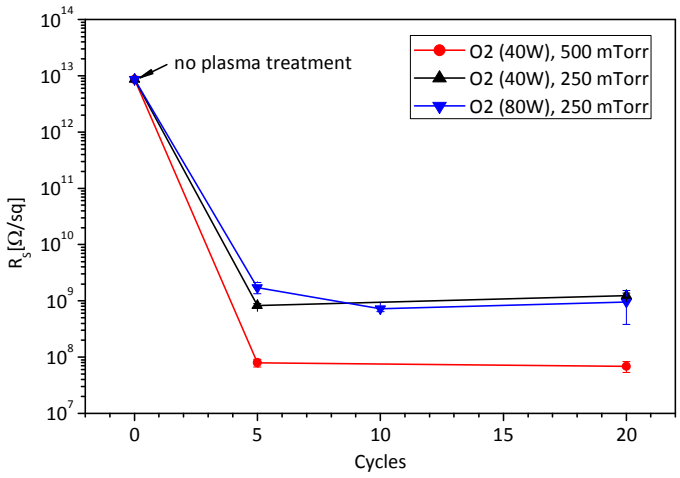

Fig. 6.12: Variation of sheet resistance of colloidal ITO films with number of plasma cycles (Plasma Study 2)

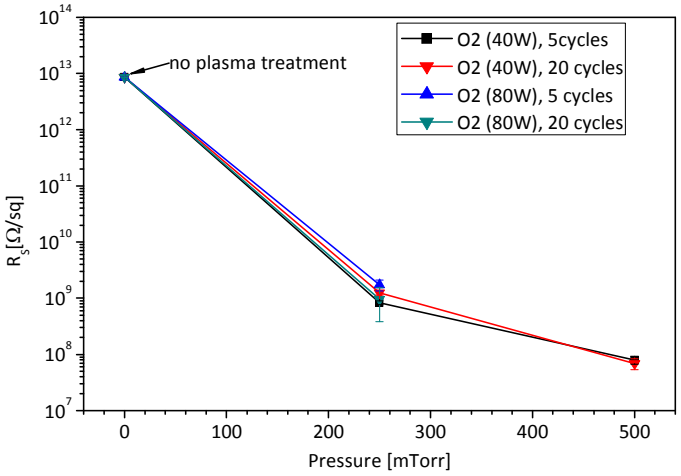

Fig. 6.13: Variation of sheet resistance of colloidal ITO films with gas pressure during RIE (Plasma Study 2)

6.4 Plasma Study 3: Effect of recipe parameters – II

The previous study indicated that pressure may be an important factor affecting the extent of ligand removal and reduction in sheet resistance during the plasma processing of the colloidal ITO films. To study this in more detail, a new matrix of plasma treatments was done on additional colloidal ITO films. Colloidal ITO was synthesized as described in chapter 3, by heating a solution of indium and tin acetates with myristic acid and 1-octadecanol in a high boiling point solvent, 1-octadecene, after degassing the solution to remove any dissolved moisture in it. In the previous studies, this step was followed by letting the solutions age for 2-3 weeks, during which the color of the solution gradually changed from blackish-olive green to turquoise-blue, as discussed in section 3.1.1. After this, colloidal ITO was precipitated by polar-non-polar separation, and dispersed in hexane. For the purpose of study, the colloidal ITO was synthesized as above. But after precipitating the ITO with polar-non-polar separation, the ITO was dispersed back in fresh 1-octadecanol, because it has a very low vapor pressure. Due to time limitations, the ITO solution was subjected to accelerated ageing by keeping this solution in a closed vial at 50°C for two days. After this,

colloidal ITO was again precipitated out by polar-non polar separation, and dispersed in hexane as before. This additional step also helped further remove some excess, suspended, insoluble organics from the solution.

ITO films were fabricated for this set of experiments by spin coating onto 1" × 1" glass substrates, made from regular glass microscope slides. The spin coating procedure used a modified recipe. 150 µl of colloidal ITO solution was pipetted on a clean glass substrate mounted on the spin coater. The spin coater was then accelerated at 200 rpm/s to 2000 rpm and spun for 20 s; and then accelerated at 1000 rpm/s to 5000 rpm and spun for 26 s. The as-spin coated films were then subjected to ligand removal plasma treatments consisting of alternating cycles of RIE in oxygen and in argon at different pressures, using an Oxford Plasmalab 80 Plus RIE machine, shown in Fig. 6.14.

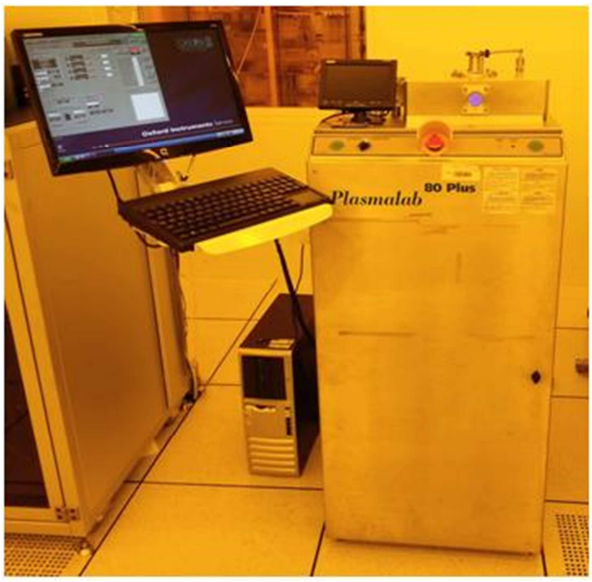

Fig. 6.14: Oxford Plasmalab 80 Plus RIE machine

The general recipe form used in plasma study 2, and presented in Fig. 6.8 was used for this study. The recipe parameters used in the specific recipes in this section are given in Table 6.2. At least two films fabricated as described above were subjected to each RIE

recipe. One film of each set that was plasma treated was also annealed at 300°C for 1 hour in air, using a tube furnace, and a ramp-up rate of 3°C/min, followed by furnace cooling.

Table 6.2: Plasma treatment matrix (Plasma Study 3)

Recipe name	O_2 RIE pressure (mTorr)	O_2 RIE power (W)	Ar RIE pressure (mTorr)	No. of cycles
Control	0	0	0	0
PS 3.01	250	40	250	2
PS 3.02	250	40	250	5
PS 3.03	250	120	250	2
PS 3.04	250	120	250	5
PS 3.05	500	40	500	5
PS 3.06	500	120	500	5
PS 3.07	800	40	800	2
PS 3.08	800	40	800	5
PS 3.09	800	120	800	2
PS 3.10	800	120	800	5

6.4.1 Characterization

The characterization of the films fabricated and processed in the manner described above was done by XPS depth profile scans and by impedance spectroscopy. These techniques and the method for the calculation of sheet resistance of the films from the impedance data have been described in previous chapters. XPS characterization was done as described in chapter 4, with the exception that a 400 μm spot size was used instead of 200 μm, which was used in the characterization described in chapter 4. Going to a larger spot size was done to obtain a more intense signal, and a higher signal to noise ratio could be achieved. For quantitative comparison, the atomic percent of carbon and oxygen was

determined based on the integral of the respective XPS signals [100], and presented as a ratio of indium content, as discussed in chapter 5.

6.4.2 Results and Discussion

6.4.2.1 Appearance

The as-spin coated films were very transparent and clear. The appearance did not change significantly after any of the plasma treatments.

6.4.2.2 X-ray Photoelectron Spectroscopy (XPS)

A comparison of the carbon and oxygen content in the colloidal ITO films after the various plasma treatments being studied has been done. The results are presented by comparing the XPS data for C1s and O1s for the various recipes. Since the recipes being studied had variations in the following parameters – RIE pressure, O_2 plasma power and number of cycles of alternating O_2 RIE-Ar RIE treatments; the same data, i.e. (a) carbon and (b) oxygen content measured at a depth inside the colloidal ITO film achieved by a cumulative 80 s of etching, has been presented as variation against these three parameters in Fig. 6.15, Fig. 6.16 and Fig. 6.17 respectively.

Fig. 6.15 (a) and Fig. 6.15 (b) show the variation of the carbon content and oxygen content as a ratio of indium content respectively, in the colloidal ITO films as a function of pressure during the RIE process, for the various RIE power and number of cycles combinations used in the plasma treatment recipes being studied. It can be seen in Fig. 6.15 (a) that for all of the RIE power and number of cycles combinations considered, an increase in RIE pressure resulted in a decrease in the carbon content in the films. This decrease in carbon content was also accompanied by a corresponding increase in the oxygen content, as seen in Fig. 6.15 (b). This not only indicates that higher RIE pressures result in a more efficient removal of the organics from the colloidal ITO films, the fact that the oxygen

content increased simultaneously supports the hypothesis that increasing RIE pressure during oxygen plasma results in a more chemically active oxygen plasma, which can degrade the residual organics by oxidation to a greater extent. The decrease in carbon content and the corresponding increase in the oxygen content was the most pronounced for films subjected to RIE done at 800 mTorr, at 120 W (recipe PS 3.10). For films annealed at 300°C in air, the carbon content significantly decreased even without any plasma treatment. Annealing at 300°C in air after the plasma treatment PS 3.10 further decreased the carbon content almost down to zero.

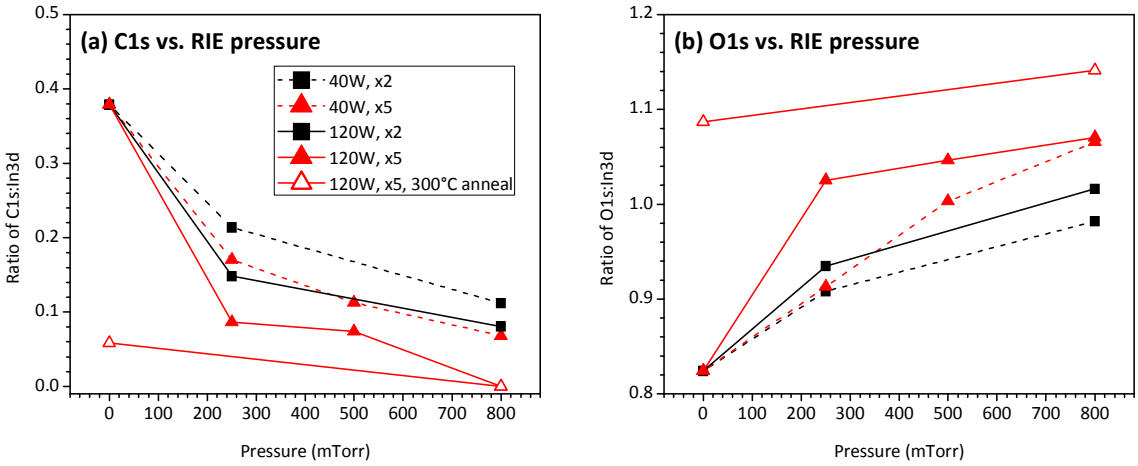

Fig. 6.15: Comparison of carbon and oxygen content inside the colloidal ITO film, after a cumulative 80 s etching, as a function of RIE pressures

Fig. 6.15 (a) also shows that in addition to RIE pressure, plasma power and the number of cycles also significantly affected the removal of residual organics from the films. This is more readily evident from Fig. 6.16 and Fig. 6.17, which are discussed below. It can be seen from Fig. 6.16 (a) and (b) that increase in RIE power also resulted in similar variations in the carbon and oxygen content of the films, i.e. the carbon content decreased and the oxygen content increased with increase in O_2 plasma power. This underscores the effect of increasing plasma power on the effectiveness of the oxidative removal of the residual organics in the colloidal ITO films.

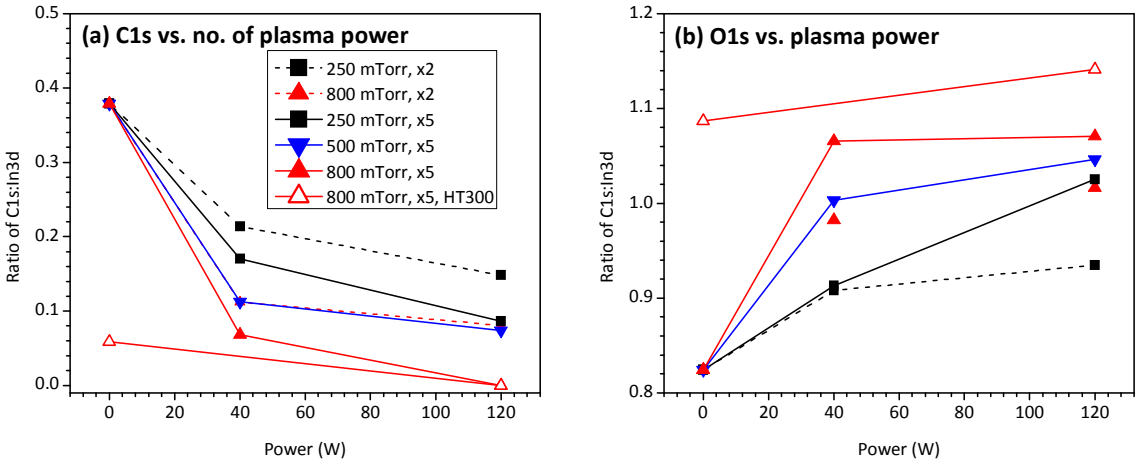

Fig. 6.16: Comparison of carbon and oxygen content inside the colloidal ITO film, after a cumulative 80 s etching, as a function of oxygen plasma power

Fig. 6.17 (a) and (b) show the variation of the carbon and oxygen content as a ratio of indium content, with the number of O_2 RIE-Ar RIE cycles. Between 2 cycles and 5 cycles, the recipes with 5 cycles resulted in decreased carbon and increased oxygen in general. Overall, it can be seen that the recipe with the highest pressure, O_2 plasma power and number of cycles, i.e. the one done with 800 mTorr RIE pressure, 120 W O_2 RIE, 5 cycles was the most effective at organics removal. After this plasma treatment, the carbon content was driven to nearly zero. This can be seen in Fig. 6.15 (a), Fig. 6.16 (a) and Fig. 6.17 (a). As mentioned earlier, on annealing after the PS 3.10 RIE treatment, the carbon content was nearly zero. This was an expected result, because this recipe had reduced carbon content to nearly zero even without any annealing.

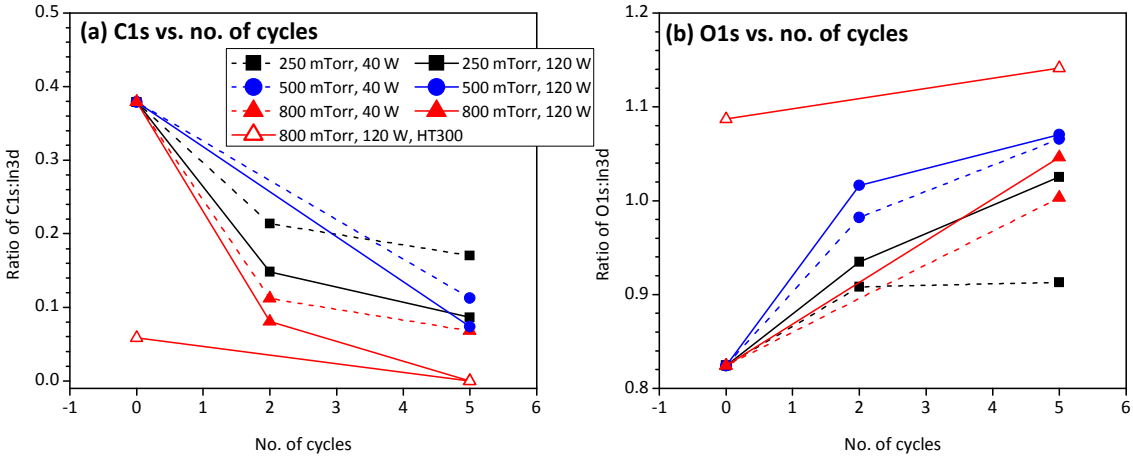

Fig. 6.17: Comparison of carbon and oxygen content inside the colloidal ITO film, after a cumulative 80 s etching, as a function of the number of (O_2 RIE→Ar RIE) cycles

6.4.2.3 Electrical Characterization

The sheet resistance of the colloidal ITO films obtained by impedance spectroscopy as described earlier has been plotted against the RIE recipe parameters – RIE pressure, O_2 plasma power, and number of O_2 RIE-Ar RIE cycles. These have been plotted against the corresponding recipe parameters in Fig. 6.18, Fig. 6.19 and Fig. 6.20 respectively. In each of these figures, it can be seen that the sheet resistance of any of the plasma treated films was at least 6-7 orders of magnitude lower than the sheet resistance of the as coated colloidal ITO film. Even for the films annealed at 300°C, any of the plasma treatments in this study, done prior to annealing, resulted in additional 1-2 orders of magnitude decrease in the sheet resistance of the colloidal ITO films.

It can be seen from Fig. 6.18 (a), (b) and Fig. 6.19 (a), (b) that either increase in the RIE pressure or increase in the RIE power dis not significantly affect the sheet resistance of the ITO films – both for non-annealed ITO films as well as for ITO films annealed in air at 300°C after the plasma treatment. It can be seen from Fig. 6.20 that while the number of cycles did not change the sheet resistance significantly for recipes with RIE gas pressure as 250 mTorr, the sheet resistance of non-annealed and annealed films were slightly lower for

recipes with 5 plasma cycles as opposed to recipes with 2 plasma cycles for recipes with RIE gas pressure as 800 mTorr. Thus, Fig. 6.18 – Fig. 6.20 showed that overall, the variation of the sheet resistance as a function of the RIE recipe parameters was not very significant, within the parameter ranges studied. The little or even insignificant variation of the measured sheet resistance in spite of the significant variation in the removal of the insulating carbonaceous phases could be explained by recognizing that the electrical behavior of these films is essentially that of a composite consisting of conductive nanoparticles in an insulating matrix. Its electrical behavior as a function of changing fractions of these two phases is determined by the percolation behavior [114] for that particular composite. The maximum rate of change of the resistivity of a composite material with change in the relative amounts of the phases occurs during the transition phase when percolation sets in. Well beyond the onset of percolation, increase in the amount of conducting phase may decrease the resistivity by only a small amount. In addition, it is possible that the more aggressive O_2 plasma used could have changed the oxygen stoichiometry in the ITO films. Thus, the reduction of the oxygen vacancy concentration may have decreased the charge carrier concentration, and thus may have counteracted the reduction in scattering by removal of the insulating phases.

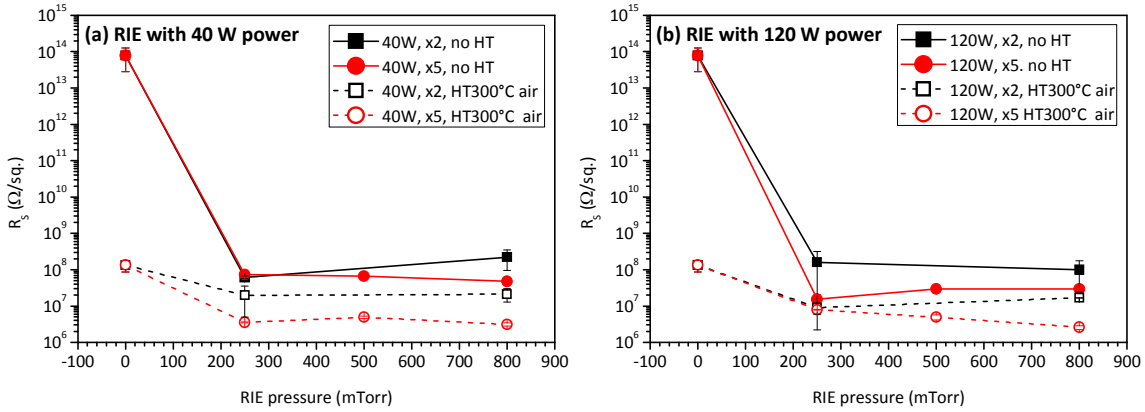

Fig. 6.18: Comparison of the sheet after a cumulative 80 s etching, as a function of RIE pressure, for RIE recipes having O2 plasma at:(a) 40 W power, (b) 120 W power

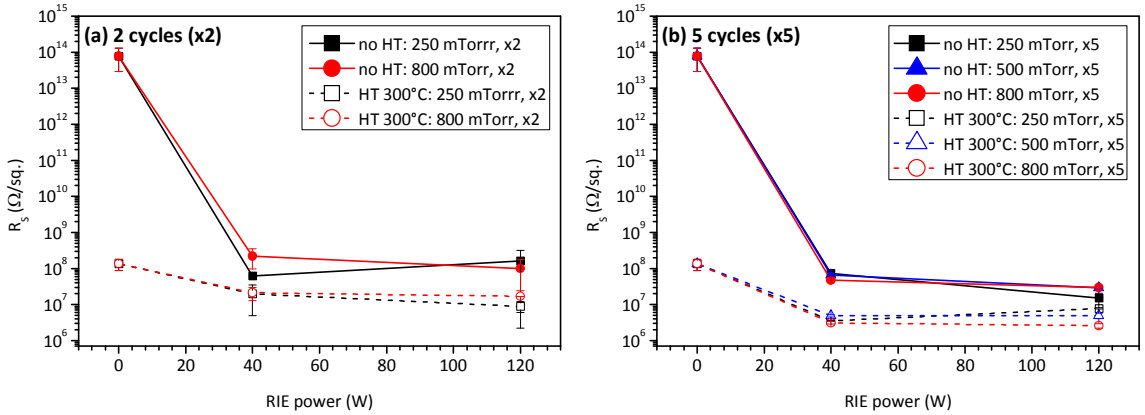

Fig. 6.19: Comparison of the sheet after a cumulative 80 s etching, as a function plasma power, for RIE recipes with (a) 2 cycles, (b) 5 cycles of alternate O2 and Ar RIE

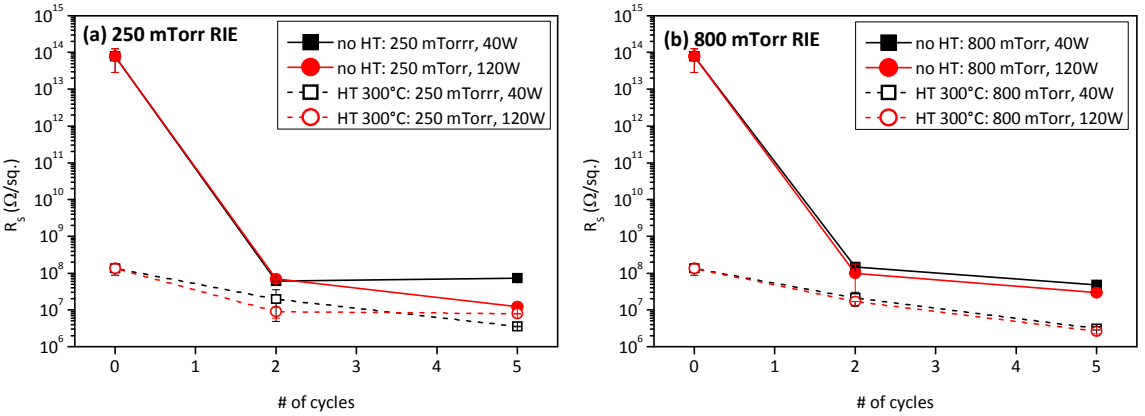

Fig. 6.20: Comparison of the sheet resistance after a cumulative 80 s etching, as a function of the number of cycles for RIE recipes done at (a) 250 mTorr, (b) 800 mTorr

6.5 Conclusions

Plasma treatments were shown to cause a very significant reduction in the sheet resistance of colloidal ITO films. The primary mechanism of sheet resistance reduction is the removal of the insulating organic/carbonaceous phases. A composite plasma treatment consisting of alternating O_2 RIE and a short Ar RIE was found to be very effective in this respect. While one study underscored the importance of RIE pressure, based on electrical characterization; a combination of electrical characterization and XPS characterization showed that both, the RIE pressure and O_2 power were also significant parameters that determined the efficiency of removal of organics and reduction of colloidal ITO film sheet resistance. It is thought that the fact that electrical sheet resistance did not decrease as significantly as the carbon content decreased with increase in the RIE pressure and O_2 RIE power could be attributed to a possible mobile charge carrier reduction due to increase in the oxygen stoichiometry; as well as the diminishing rate of increase of the conductivity, as the film, behaving like a percolating composite that is in a regime well beyond the onset of percolation. In addition, the nanocrystalline nature of the colloidal ITO film results in an inherent high degree of scattering, which may prevent a reduction of sheet resistances to levels which may be comparable with microcrystalline sputter-deposited ITO films.

Chapter 7:
Analysis of Impedance Spectroscopy

The bulk of electrical characterization done all over the world is based on dc based measurements. These characterization methods are indeed useful in providing information about the steady state electrical behavior of a material under a constant voltage. However, the majority of the electrical phenomena in nature and in industry are dynamic and transient. DC characterization methods are insufficient to probe and understand them. Impedance spectroscopy can fulfill this need by characterizing the behavior of a system at various frequencies of electrical stimulation. Impedance spectroscopy is the measurement of the complex impedance of a sample or of a system, by measuring the current response and the phase lag of a system in response to an applied ac voltage, frequency and dc bias. Impedance spectroscopy was introduced and discussed in chapter 2 [74, 75, 117]. Some impedance data was presented in chapters 4-6. In this chapter, generalized trends across all sample sets and assignment of possible equivalent circuits that fit the measured response will be presented.

7.1 Bode and Nyquist plots

Fig. 7.1 (a)-(d) show the Nyquist plots of the averaged impedance of ITO films subjected to O_2-Ar RIE x5 plasma treatment after being annealed at various temperatures in air. Although all the complex impedance curves are plotted on the same graph, they are presented in different scales going from Fig. 7.1 (a) through Fig. 7.1 (d). This was done because the size of each plot varies from the others by orders of magnitude, making it impossible to show all of them using the same linear scale. The prominent feature of the plots shown in Fig. 7.1 is a semicircle in the first quadrant, which extends into a smaller

semicircle in the fourth quadrant. A semicircle in the first quadrant is one of the most common forms that the Nyquist plot of impedance might take. It represents a resistive-capacitive behavior, whose ideal behavior may be represented by a circuit consisting of a resistor and a capacitor in parallel [75]. A semicircle in the fourth quadrant, on the other hand indicates a resistive-inductive behavior [75]. A visual inspection of the impedance curves hence suggests the manifestation of parallel RC and parallel RL behavior.

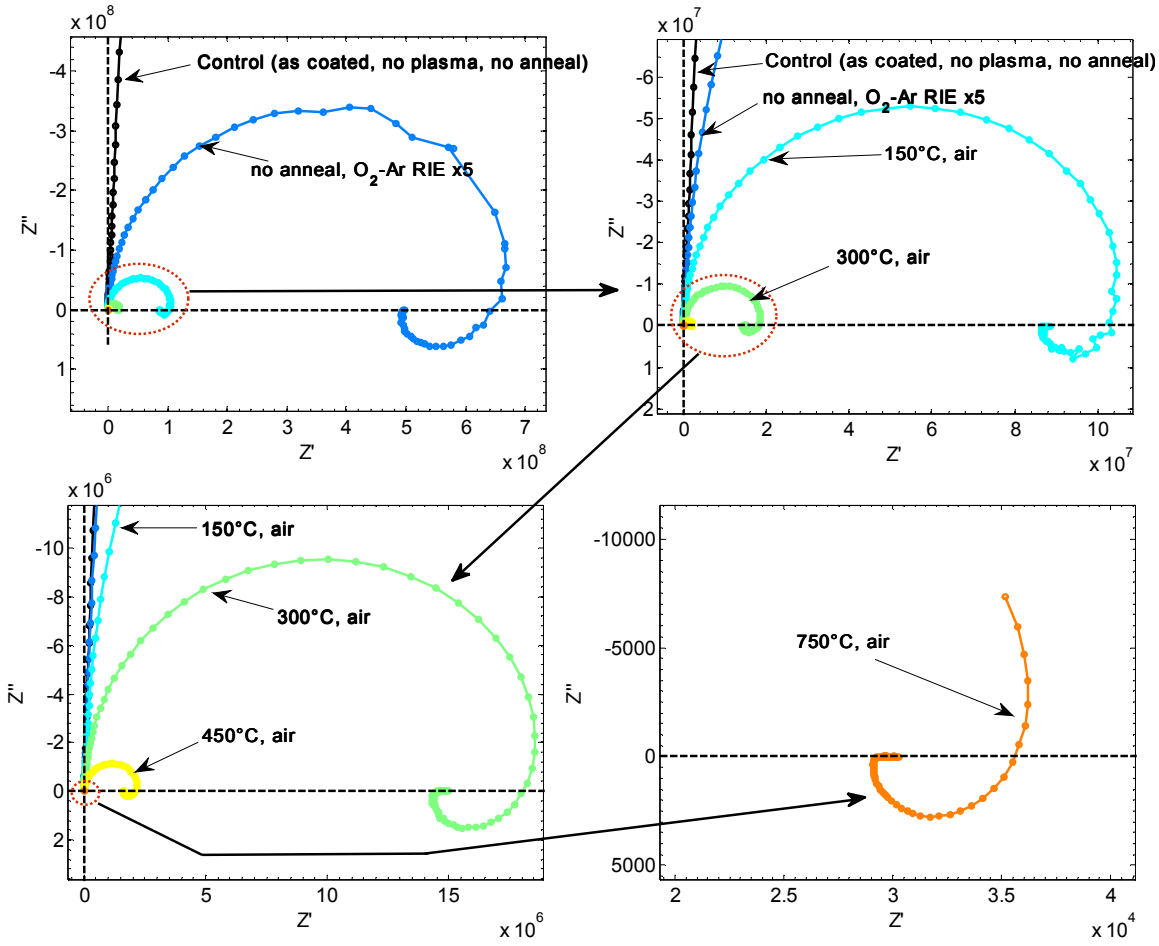

Fig. 7.1: Nyquist plots of averaged impedance curves of colloidal ITO deposited on fused quartz substrates, after O_2–Ar RIE x5 plasma treatment, as a function of annealing temperature in air

This Nyquist plot is plotted in the log-log scale in Fig. 7.2, after converting the real and imaginary part of impedance to their absolute values, because negative values cannot

be represented on a log-log plot. The spread of the curves across the log-log scaled chart clearly shows the huge differences in magnitude of the impedance curves that resulted from the plasma and annealing treatments discussed in the earlier chapters.

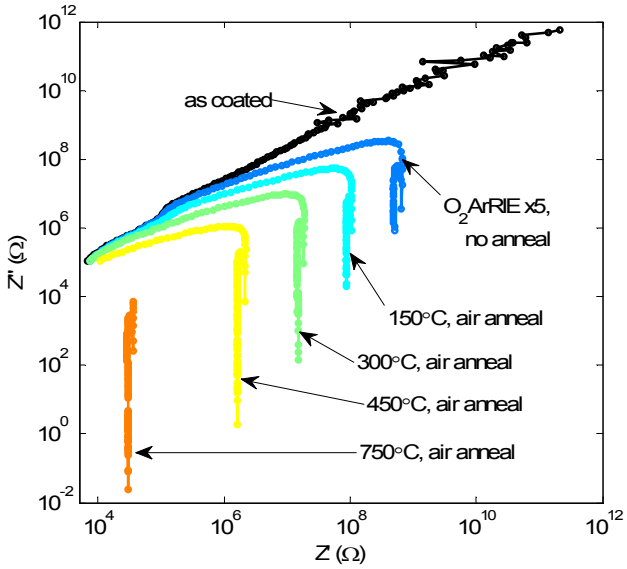

Fig. 7.2: Nyquist plots of averaged impedance curves of colloidal ITO deposited on fused quartz substrates, after O_2–Ar RIE x5 plasma treatment as a function of annealing temperature in air plotted on a log-log scale

Fig. 7.3 shows the Bode plots of the impedance magnitude, phase angle, as well as the real and imaginary parts of impedance for colloidal ITO films annealed at various temperatures in air, after O_2-Ar RIE x5 plasma treatment. These are also compared with the corresponding Bode curves for the as-coated colloidal ITO film. It can be seen that as the annealing temperature increased, the impedance magnitude curves plateaued off at lower and lower values, thus indicating that the films were more and more conducting. The Bode plots of the real part of impedance, plotted in Fig. 7.3 (b), are very similar to the magnitude plots, except that they also show a hump before transitioning from the capacitive behavior to resistive behavior, as we go down in frequency. Since the plots are in the log scale along both the axes the shape of the hump is not immediately apparent. This hump suggests the manifestation of resistive-inductive (RL) behavior in this frequency window.

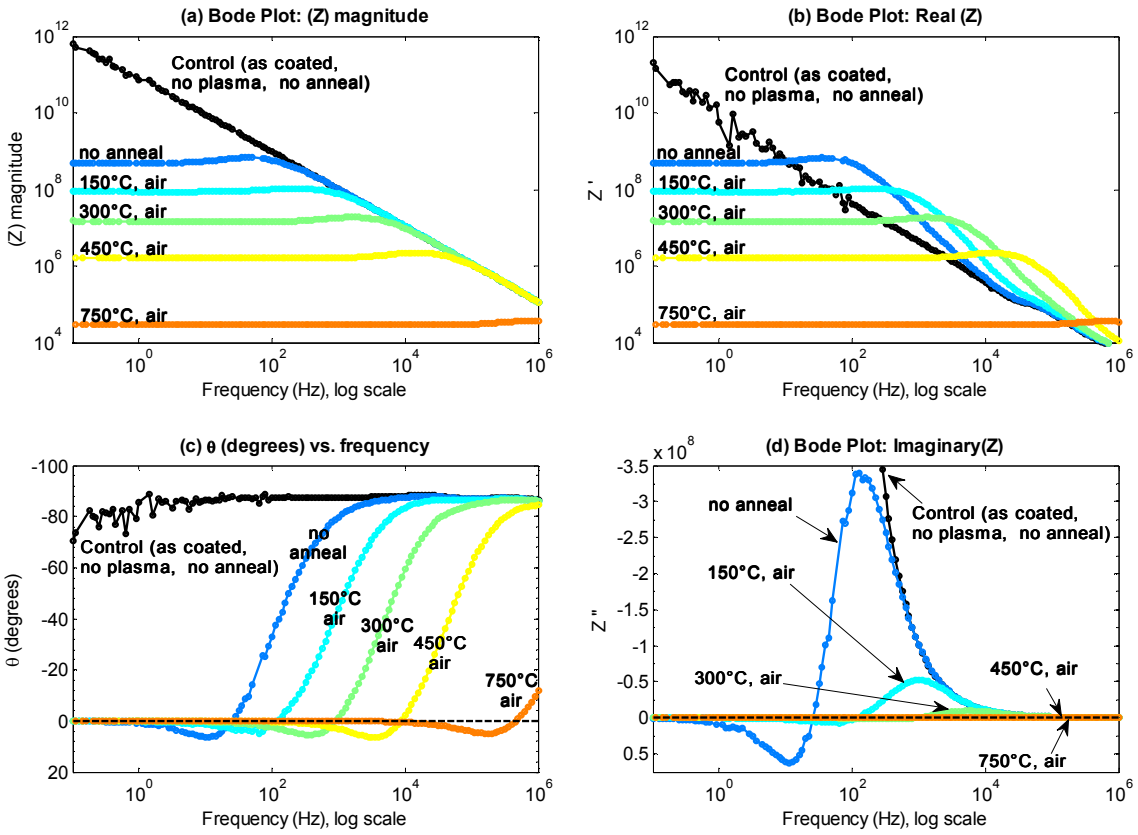

Fig. 7.3: Bode plots of averaged impedance curves of colloidal ITO deposited on fused quartz substrates, after O_2-Ar RIE x5 for various annealing temperatures in air, showing (a) impedance magnitude, (b) real part of impedance, (c) impedance phase angle, (d) imaginary part of impedance

The nature of impedance behavior can also be seen clearly in the Bode plots of the impedance phase angle which is shown in Fig. 7.3 (c), and in the Bode plots of the imaginary part of impedance, shown in Fig. 7.3 (d). Fig. 7.3 (c) shows that the phase angle increases from –90°, while going from higher to lower frequencies, increases beyond zero and relaxes to zero at low frequencies. The frequency range measured and presented in Fig. 7.3 is not sufficient to capture in entirety the features mentioned above for the impedance curves of the as-coated, no plasma treated films, as well as the films annealed at 750°C in air. As with the impedance magnitude and imaginary impedance curves, this indicates that the electrical behavior of the films in general transitions from an RC behavior to a purely resistive

behavior, with a brief window of RL behavior in between. As described in chapter 2, this transition is manifested a relaxation peak in the Bode plot of the imaginary part of impedance, shown in Fig. 7.3 (d). Since the peak heights vary by orders of magnitude, relaxation peaks for all the curves cannot be seen. Hence, normalized curves for the imaginary part of impedance are plotted in Fig. 7.4. At least two relaxations and corresponding frequencies of relaxation can be observed for most of the curves. The Z'' peaks above the X-axis represent RC relaxation, which is commonly observed in polycrystalline samples. The Z'' peaks below the X-axis have appearance similar to those arising from RL relaxations. It will be discussed later in the chapter that RL relaxation leading to these peaks seems unlikely. It can be seen that the frequency of relaxation for both the types of relaxations in Fig. 7.4 steadily increases with increase in the annealing temperature. In other words, the relaxation time constant becomes smaller and smaller with increase in annealing temperature, as shown in Fig. 7.5. The frequency range used for impedance spectroscopy was not high enough to observe the RC relaxation in films annealed at 750°C. Hence, that time constant was extrapolated based on the trend; and it is indicated by an unfilled data point in Fig. 7.5. As discussed in chapter 6 (Fig. 6.7 (d)), these films become more and more conductive with increase in annealing temperature. As a result, one might expect the transient charging and discharging at various interfaces within the film, which would naturally lead to smaller relaxation time constants.

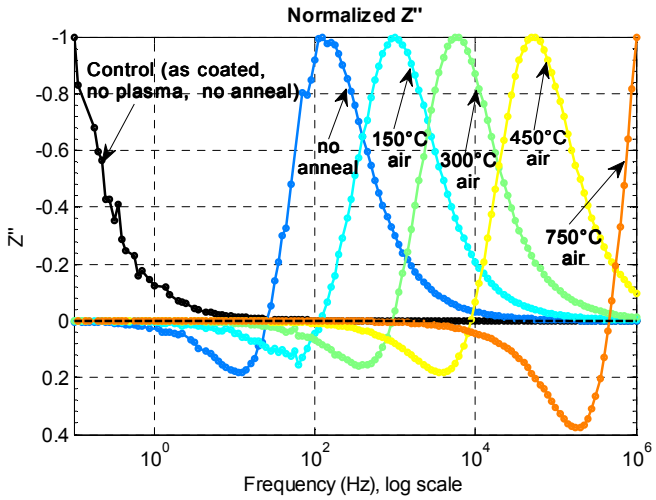

Fig. 7.4: Bode plot of normalized imaginary part of impedance of colloidal ITO on fused quartz substrates, after O_2-Ar RIE x5 for various annealing temperatures in air

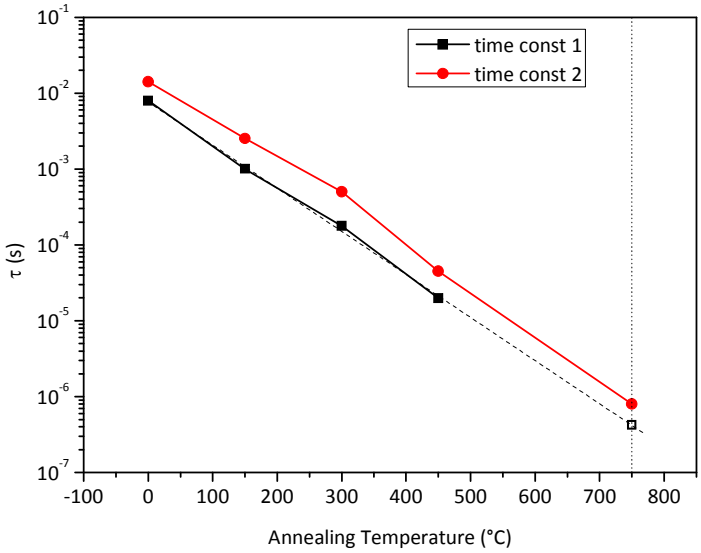

Fig. 7.5: Variation of two relaxation time constants as determined from *Z"* Bode plots as a function of annealing temperature (Unfilled point indicates extrapolated point)

Representative Bode plots of the impedance magnitude and phase angles of non-plasma treated ITO films annealed at various temperatures in air and in argon were presented in chapter 5, in Fig. 5.14. These curves show features similar features to the plots described above, and in general, the electrical behavior can be described along the same lines. Bode plots of the magnitude, phase angle; and the real and imaginary parts of the

averaged impedance of ITO films annealed at various temperatures for other combinations of plasma treatment and annealing atmosphere are presented in Appendix B.

A better understanding of the electrical processes occurring in the sample, which leads to the observed impedance behavior, can be obtained by modeling and fitting equivalent circuits containing discrete electrical components like resistors, capacitors, and inductors; such that the impedance behavior of the equivalent circuit matches the observed impedance behavior as closely as possible.

7.2 Equivalent Circuits

As described in the previous section, the impedance curves being discussed show RC and RL aspects to their behavior. Simulations and fitting of the equivalent circuits to the observed data was done using ZView™ software [118]. The general form of one of the equivalent circuits which was able to fit the impedance data, shown in Fig. 7.6 (a), consists of a parallel RL element nested within a parallel RC (Voigt) element. A similar impedance behavior has been observed elsewhere in the literature for conductor-insulator composite systems like carbon nanotubes deposited on paper [119]. Such a nested RCRL circuit could explain the electrical behavior very well.

However, it is possible for two or more different circuits to have the same exact impedance at all frequencies [74, 117]. Another equivalent circuit, which could be fitted to the same observed data, is shown in Fig. 7.6 (b). It consists of a parallel RC element containing negative R and negative C nested within a regular parallel RC element. Both the equivalent circuits fit the data equally well.

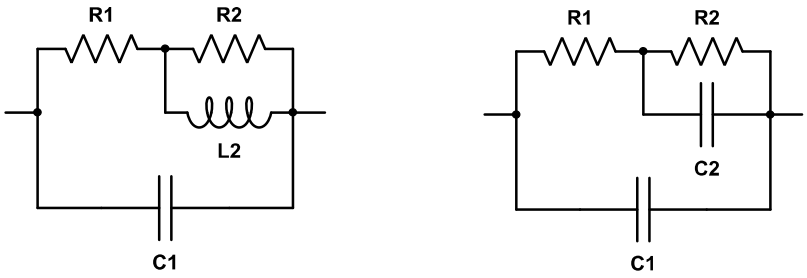

Fig. 7.6: Equivalent circuits: (a) Nested RCRL, (b) Nested RCRC

Fig. 7.7 and Fig. 7.8 show the Bode and Nyquist plots of a representative dataset, overlaid with the fitted impedances of the two equivalent circuits. A good fit can be seen. Some mismatch may be observed at the very high frequencies and the very low frequencies. This is commonly observed in experimental data.

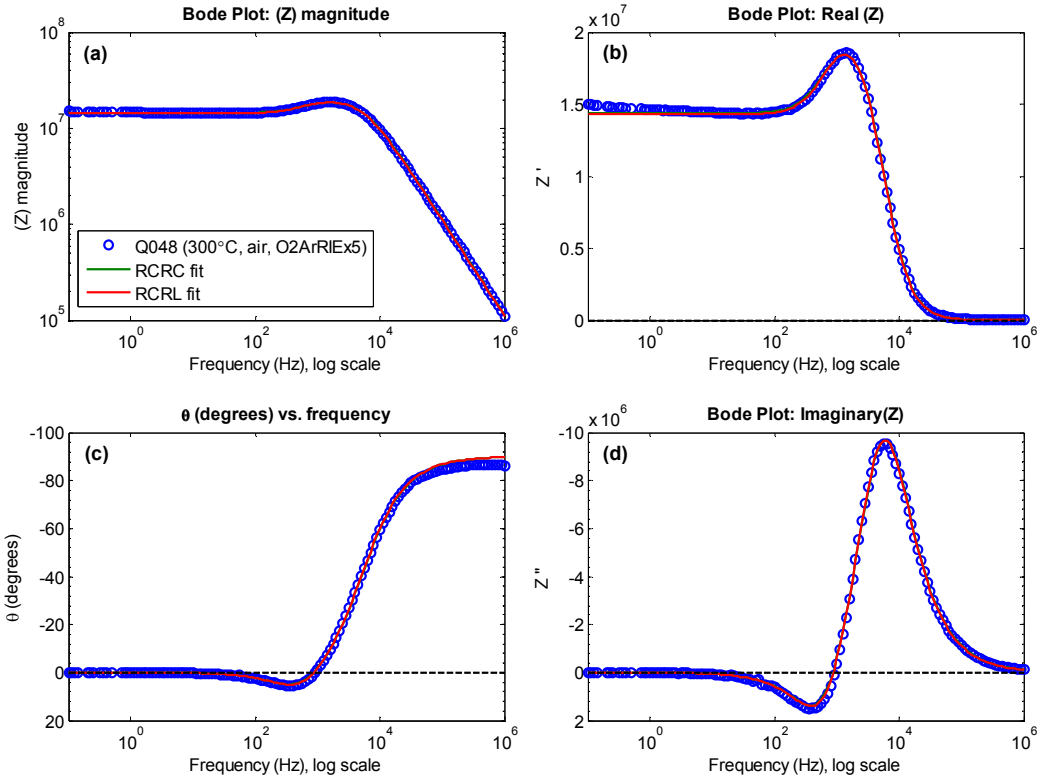

Fig. 7.7: Bode plots of the averaged impedance spectrum of a colloidal ITO film deposited on fused quartz, annealed at 300°C in air after O_2 –Ar RIE x5 plasma treatment. This is overlaid with the corresponding Bode plots of the fitted nested RCRL and RCRC circuits to demonstrate the closeness of fit.

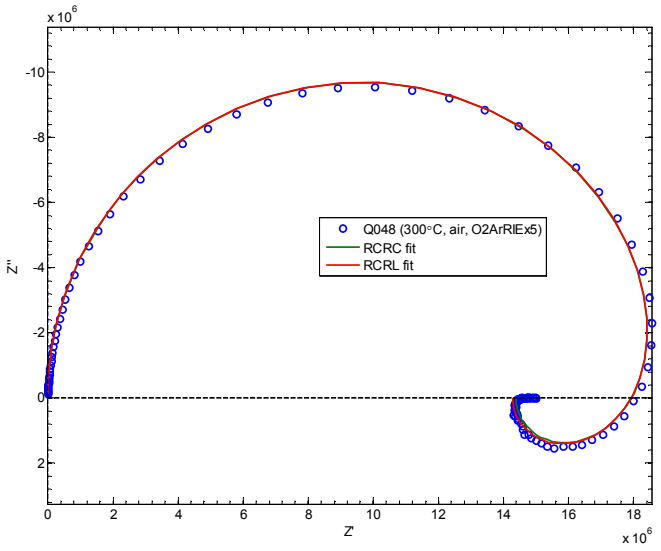

Fig. 7.8: Nyquist plot of the averaged impedance spectrum of a colloidal ITO film deposited on fused quartz, annealed at 300°C in air after O_2 –Ar RIE x5 plasma treatment. This is overlaid with the Nyquist plot of impedance of the fitted nested RCRL and RCRC circuits

Fig. 7.9 (a) and (b) show the variation of the equivalent circuit elements of the nested RCRL circuit (R1, C1, R2, L2) and the nested RCRC circuit (R1, C1, –R2, –C2), fitted for the impedance spectra of ITO films subjected to O_2-Ar RIE x5 treatment, as a function of the annealing temperature in air. Since the values of R2 and C2 are negative, –R2 and –C2 are plotted in Fig. 7.9 (b) instead of R2 and C2 to enable comparison and optimize the Y-scale. On comparing the variation of the values of the resistors R1 and R2 in Fig. 7.9 (a) and (b), with the variation of the sheet resistance of the same films, i.e. ITO films on fused quartz subjected to O_2-Ar RIE x5, and annealed in air; which was shown in Fig. 6.7 (d) in the previous chapter, it can be seen that R1 and R2 follow the variation of the low frequency resistance very closely. Fig. 7.9 (a) and (b) also show that the value of the capacitor C1 stays fairly constant irrespective of the annealing temperature. The geometric capacitance, C_0, which is present due to the measurement set-up and the electrode configuration, was determined to be very close to the values of C1 shown in Fig. 7.9. Thus, one can conclude that the major contribution to C1 comes from the geometric capacitance. However, this does

not rule out contributions from the sample being included in C1. The sample capacitance will be in parallel to C_0; and hence, if it is one or more orders of magnitude smaller than C_0, its value will be essentially buried under the dominant C_0. The fact that Fig. 7.9 (a) and (b) seems to suggest that the value of C1 monotonically decreases with an increase in the annealing temperature, however small the decrease may be, suggests that changes in the sample contribution to C1 may be manifested here. The microstructural characterizations presented in chapter 5 suggest that there is no appreciable change in the grain size with annealing in the range of annealing temperatures studied. It is thought that the intra-grain capacitance may be remaining constant because of no grain growth, but the inter-grain capacitance across grain boundaries and nano-voids might be decreasing with increase in annealing temperature due to some grain consolidation and void shrinkage.

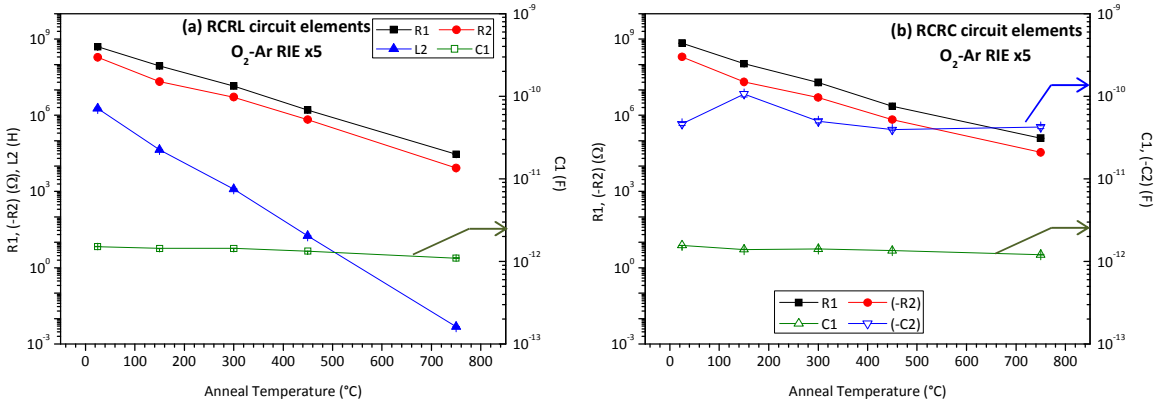

Fig. 7.9: Variation of the discrete electrical circuit elements with annealing temperature, for colloidal ITO films annealed in air after O_2-Ar RIE x5 treatment (arrows indicate use of secondary axis for that curve)

Fig. 7.9 (a) also shows that the value of the inductor in the nested RCRL circuit changes very widely with the annealing temperature. It attains enormous values for films that are not annealed at a very high temperature. While the huge variation of the resistance aspects of the equivalent circuits was expected, considering that the size of the impedance plots, and the measured sheet resistance varied by several orders of magnitude; it is very

difficult to imagine a physical cause that might be able to explain the several orders of magnitude variation in the inductance seen in the fitted data. In addition, the very large values of the inductances of the non-annealed samples, and those annealed at lower temperatures seem outright impossible, especially considering that ITO is not known to be ferromagnetic, and the size of the films was fairly small, about 1" × 1" each. The only possible hypothesis that could even remotely support these huge inductances was the possibility that the nanoparticle form may have somehow induced ferromagnetic behavior in the ITO nanoparticles. This was easily proved to not be the case by placing a vial of the blue-green colored ITO colloidal solution between the poles of strong permanent magnets. No color separation or gradation was observed either immediately, or after letting the vial sit between the magnet poles for several hours.

Let us now consider the second equivalent circuit consisting of nested RCRC elements. The variation of the equivalent circuit elements is shown in Fig. 7.6 (b). As in the nested RCRL circuit discussed earlier, the resistor elements vary over several orders of magnitude, almost in sync with the low frequency resistance of the films. As with the nested RCRL circuit, capacitor C1 does not change much with annealing temperature. R2 and C2 in the nested Voigt element (parallel RC element) are both negative as mentioned earlier. Negative resistance [120-122] and negative capacitance [123-129] have been widely reported in the literature. Hence, the fact that this equivalent circuit contains negative resistance and negative capacitance cannot be ruled out on that basis alone.

Negative capacitance has been reported in systems such as solid-state structures [127], polyaniline films [124], metal-semiconductor interfaces [129], conductor-non-conductor composites such as alumina-SiC whisker composites [130], PbS nanocrystals in polymer [123], metallic Ga nanoparticles in a dielectric matrix [131], and also organic

semiconductor devices [125]. It has been attributed to various phenomena such as impact ionization, injection of minority carriers, imaginary component of mobility etc. According to Bakueva et al., negative capacitance always coexists with high dc conductivity [123]. El Kamel et al. attributed the negative capacitance observed in amorphous $BaTiO_3$:H to charge injection through intermediate surface states, and a sudden charge transfer at the electrodes above a critical charge density [126]. Negative resistance has also been widely reported in the literature [120-122, 132-134]. Differential negative resistance is the basis of the operation of Gunn diodes [132-134], which are widely used to generate microwaves. The Gunn effect, which causes differential negative resistance occurs essentially due to trapping of charge carriers at intermediate energy states with increasing potential difference. Traps states and charge injection can thus give rise to both negative resistance and negative capacitance. The nanocrystalline and nanocomposite nature of the colloidal ITO films that were studied is expected to give rise to such phenomena in the films. As seen in the HRTEM image shown in Fig. 4.5, ITO nanoparticles used in this study are highly crystalline; and therefore should be expected to be highly conducting. However, since the interface between the ITO nanoparticles is highly non-optimal – ranging from very insulating in case of completely ligand covered particles to partially touching nanoparticles interspersed with nanoporosity and insulating phases, it is likely that charge trapping must be occurring at the nanoparticle interfaces.

Fig. 7.10 (a)-(d) shows Bode plots of the complex capacitance of colloidal ITO films. This was calculated from the complex impedance plots shown in Fig. 7.3, using Eqn. 7.2.

$$C^* = \frac{1}{j\omega Z^*} \qquad \text{Eqn. 7.1}$$

It can be clearly seen that the real part of complex capacitance does become negative at lower frequencies, which further supports the validity of the equivalent circuit containing negative capacitance.

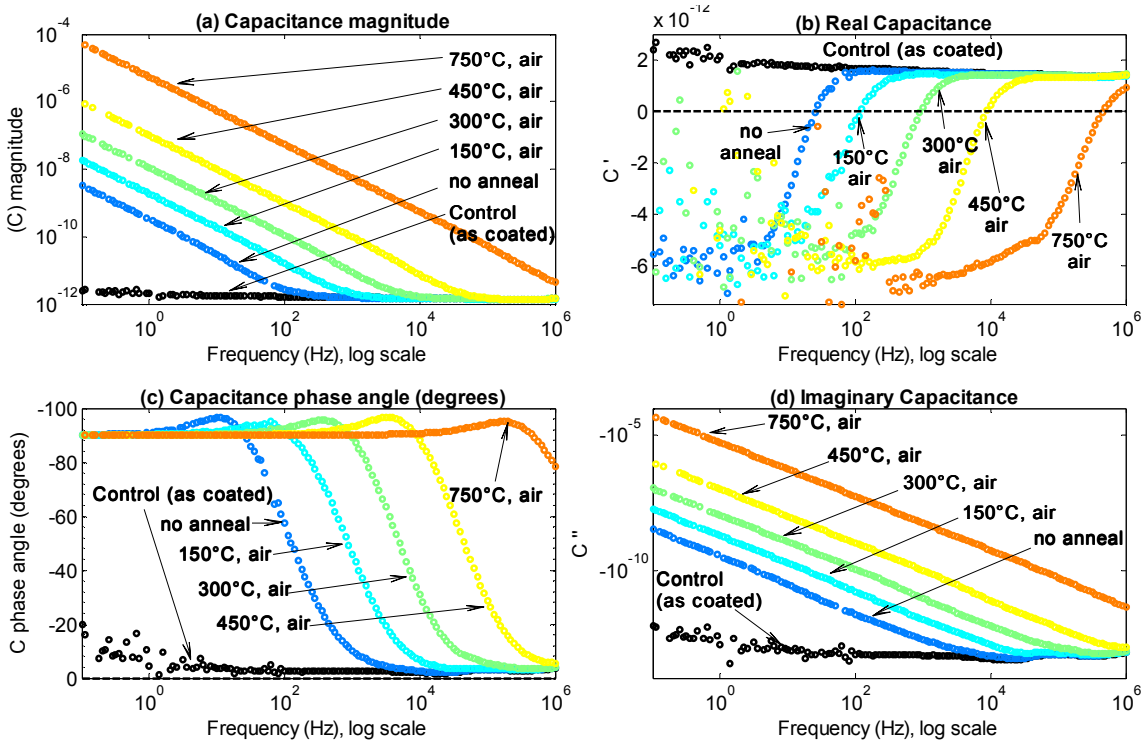

Fig. 7.10: Bode plots of complex capacitance of colloidal ITO deposited on fused quartz substrates, after O_2-Ar RIE x5 for various temperatures of annealing in air, showing (a) capacitance magnitude, (b) real part of complex capacitance, (c) capacitance phase angle, (d) imaginary part of complex capacitance

Such behavior has also been reported to occur in metallic conducting systems as reported by Jonscher [135]. Furthermore, the fact that both the elements of the nested Voigt element, i.e. R and C are negative essentially also means that the time constant, $\tau_{\text{parallel RC}}$, given by Eqn. 7.2, is positive, and makes physical sense.

$$\tau_{\text{parallel RC}} = RC \qquad \text{Eqn. 7.2}$$

The variation of the equivalent circuit elements of the corresponding equivalent circuits fitted to the impedance spectra of colloidal ITO films after O_2 plasma treatment and for those without any plasma treatment are shown in Appendix B. These variations are very similar to the variation of the equivalent circuit components for the films subjected to O_2-Ar RIE x5 plasma treatment; and the following discussion about Fig. 7.9 also apply to the equivalent circuit elements described in the appendix.

The various electrical transport processes occurring within the ITO films are shown schematically in Fig. 7.11 (a)–(e). Some or all of these are thought to occur in the ITO films to various extents during electrical stimulation. The extent to which any or all of these processes may occur depends on the microstructure of the film and the film properties due to the kind of processing the film may have undergone. The schematic of the microstructure of the ITO films after various processing steps was shown in Fig. 5.16. In as-coated films, or those films which have most of the organic coating intact after processing, the microstructure will resemble Fig. 5.16 (a). Capacitive charge transport, which is schematically shown in Fig. 7.11 (a), dominates the electrical transport processes in such films. In addition, there is expected to be a tiny proportion of some leakage current resulting from charge transport across the insulating interfaces. This very high interface resistance results in the very large values for R1 in the equivalent circuit discussed above. Since the distance between two nanoparticle surfaces separated by two organic passivating layers (one on each nanoparticle) is very small – estimated to be 3 nm or less; there could also be some tunneling component to the charge transport between the coated nanoparticles (shown in Fig. 7.11 (b)). For films with the organic coating completely removed either due to thermal degradation or plasma treatment, we have a microstructure resembling Fig. 5.16 (c). In such a case, the proportion of conductive charge transport is higher because the nanoparticles are in direct contact with each other. This is shown in Fig. 7.11 (c). However, with the nanoparticles pretty much only touching each other partially, the quality of electrical contact between them cannot be said to be optimal. As a result, the interface resistance R1 is still moderately high, though lower than in the case of as-coated films. For films that have the organics layer only partially removed, the electrical transport situation is expected to be between the two situations described above. For ITO films which have not only had most of the organics layers removed, but also have had some degree of

grain consolidation though necking between grains as shown in Fig. 5.16 (d), the electrical contact between the neighboring particles is improved, resulting in decreased interface resistance R1.

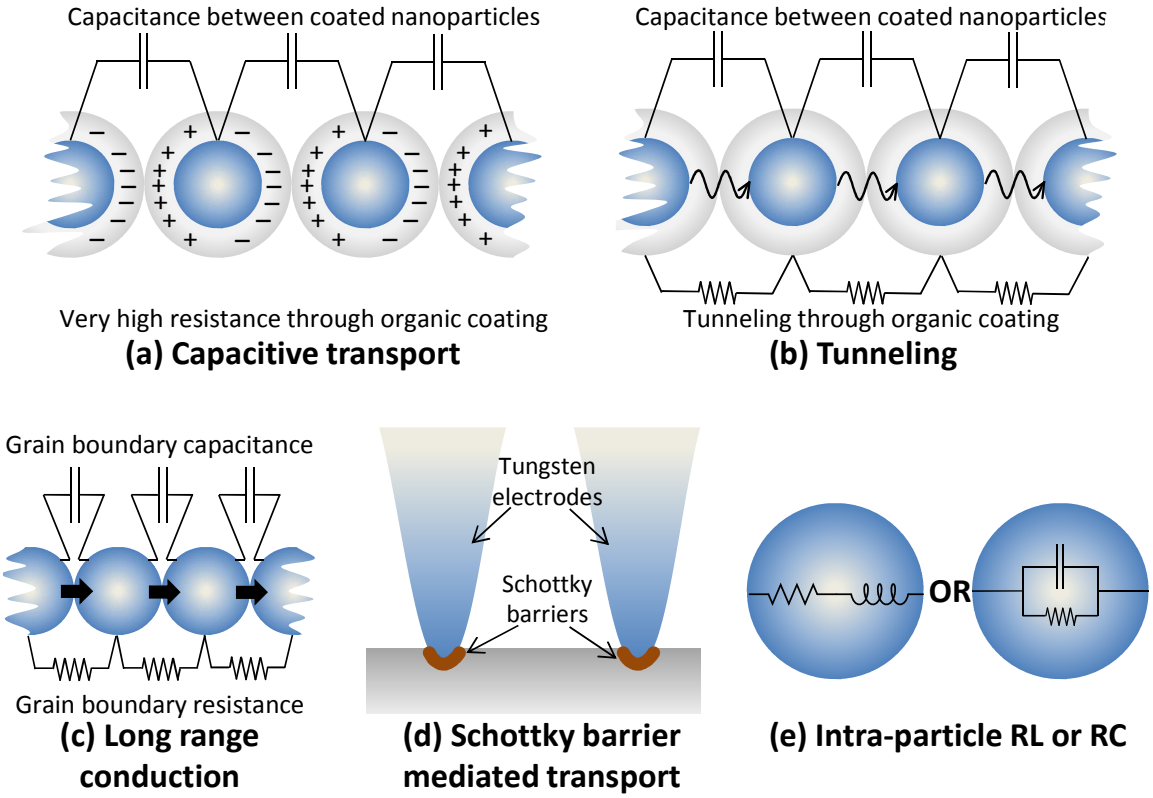

Fig. 7.11: Schematic of some of the various electrical phenomena that may be occurring in the colloidal ITO films: (a) capacitive transport between ITO nanoparticles coated with insulating organics, (b) electron conduction between ITO nanoparticles in electrical contact with each other, (c) tunneling across insulating organic coating in the nanoparticles, (d) Schottky barrier mediated electrical transport between the probes and colloidal ITO film, (e) intra-particle impedance: metallic (resistive-inductive) or resistive-capacitive behavior

In addition to these electrical phenomena discussed above, the nanoparticles, there are other processes that may be taking place. There are a number of surface defects and intermediate states on the exposed surface of the nanoparticles, as well as on the interfaces. These can act as charge traps. It has been shown in the literature that such trap states and interfaces can result in negative values of differential resistance and capacitance [120-129].

For example, intermediate states that are just above the conduction band could potentially trap conduction electrons as the applied electric field is increased. This essentially locally decreases the available charge carriers, and thus reduces the current density with an increase in electric field. This behavior is similar to what occurs in Gunn diodes [132], and it results in a negative value for (dj/dE) or (dI/dV), where j = current density, E = electric field, I = current and V = potential difference; thus resulting in a negative differential resistance. Trap states may also affect the capacitance behavior. It is possible that some of the intermediate states trap charge carriers during the initial part of the ac cycle; and they suddenly release them in a torrent on going above a certain threshold electric field. This could result in a perceived negative capacitance due to the instantaneous negative value of (dQ/dV). In addition, Schottky barriers formed between the ITO film and the metal probes (Fig. 7.11 (d)) could result in a similar trap and release of charge with increasing voltage during the ac cycle, which can result in negative differential capacitance as detected by impedance spectroscopy.

The above discussion focused on the aspects of the electrical transport in the colloidal ITO films occurring primarily at the interfaces. The electrical transport processes that occur within the ITO nano-crystallites themselves may not be manifested in the impedance spectra being discussed. The impedance behavior of the nano-crystallites could be either similar to series RL or parallel RC. If we were to consider parallel RC behavior, for example, its relaxation frequency, f_{relax}, (with a corresponding time constant τ), is given by:

$$f_{\text{relax}} = \frac{\omega}{2\pi} = \frac{1}{2\pi\tau} \qquad \text{Eqn. 7.3}$$

Since the frequency range used in the impedance spectroscopy scans was from 100 mHz to 1 MHz, the characterization could potentially only detect relaxations with time constants between 1.59 s and 159 ns. Bulk crystalline ITO has almost metallic conductivity.

Let us use an often quoted value for the resistivity of optimized ITO films of $\sim 10^{-4}\Omega$.cm [136] for the purpose of estimating the resistance of an ITO nanoparticle. Since they have been determined to be spheroids of diameter $\approx$ 6 nm, let us consider a cube of side 6 nm for simplifying the calculation. This gives us a resistance R = 166.67 Ω. Even if we were to assume a capacitance as high as 1 pF, to be in the range observed, this will give us a time constant $\tau = RC = 0.1667$ ns, which would correspond to a relaxation of 0.955 GHz, which falls outside the measured range by a significant extent. The actual nanoparticle capacitances would probably be orders of magnitude lower than 1 pF as assumed here, which would mean much higher relaxation frequencies. Although the impedance spectrum of the ITO films can be expected to have contribution from intra-grain conduction and intra-grain capacitance, the above exercise in estimation of the relaxation frequency shows us that it would not be manifested in the impedance spectra discussed in this document. Hence, although not deducible directly from the impedance data, the equivalent circuit of the colloidal ITO films would be more accurately described by including an additional parallel RC element, schematically shown in Fig. 7.11 (e), corresponding to the intra-grain resistance and capacitance of the ITO nanoparticles.

7.3 Determination of sheet resistance of films of ITO films

The set-up for the measurement of electrical properties of ITO films was presented in chapter 4. Impedance spectroscopy scans were done in the 2-electrode mode, between adjacent pairs of probes on the four probe set-up. A schematic of this set-up is shown in Fig. 7.12. The size of the electrical contact from each probe on the film has a radius r, and the probe tips are separated by a distance s. The film has a thickness $t \ll s$, and it is made from a material having electrical resistivity ρ.

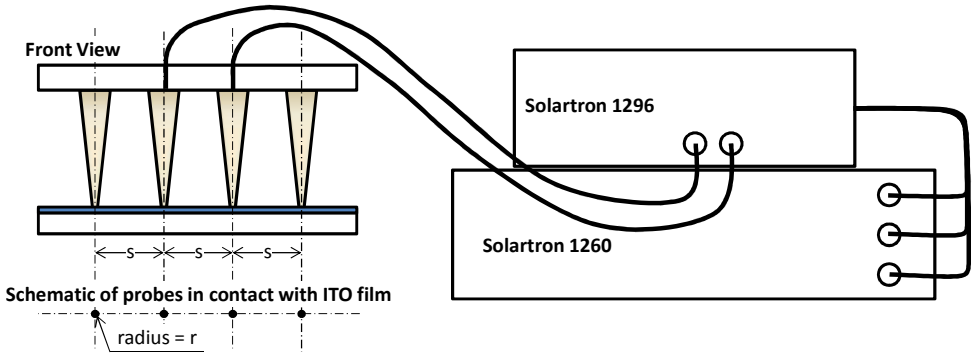

Fig. 7.12: Schematic of 2 probes impedance spectroscopy set-up

We can assume the current to be emanating in a circular shape from the probe tips being used. The differential resistance, dR, of the annular region of width dx, at a distance x from the center of one of the probe tips is given by:

$$dR = \rho\left(\frac{dx}{A}\right), \text{where } A = 2\pi xt \qquad \text{Eqn. 7.4}$$

$$dR = \rho\left(\frac{dx}{2\pi xt}\right) = \frac{R_S}{2\pi}\left(\frac{dx}{x}\right), \text{where } R_S = \frac{\rho}{t} = \text{ sheet resistance} \qquad \text{Eqn. 7.5}$$

The resistance between two adjacent probe tips may be determined by integrating dR between the boundaries of the corresponding electrical contacts of the adjacent probes.

$$R = \int_r^{s-r} dR = \frac{R_S}{2\pi}\int_r^{s-r}\left(\frac{dx}{x}\right) = \frac{R_S}{2\pi}\ln\left(\frac{s-r}{r}\right) \qquad \text{Eqn. 7.6}$$

$$\text{This gives us: } R_s = \frac{\pi R}{\ln\left(\frac{s-r}{r}\right)} \qquad \text{Eqn. 4.1}$$

This expression was used in the chapters 4-6 to calculate the sheet resistance of ITO films.

Fig. 7.13 shows a comparison of the values of sheet resistances calculated using the above expression from impedance spectroscopy with the sheet resistance, R_S, determined from dc 4-point probe measurements. The expression used to calculate the sheet resistance in 4-point probe was derived similar to Eqn. 4.1; except that since in the dc 4-probe method, the voltage is measured between the middle two probes, the integration is done between

the limits s and $2s$. This gives us the following expression [137, 138], which is widely used to determine the sheet resistance of thin films reported in the literature.

$$R_S = \frac{\pi R}{\ln 2} \qquad \text{Eqn. 7.7}$$

The dc measurements could only be done for the relatively more conducting films because of instrument limitations. As Fig. 7.13 indicates, the values agree fairly well. This helps to confirm that the methodology used to determine the sheet resistance using 2-point probe impedance spectroscopy measurement, as described above, is correct within reasonable limits. In addition, the correspondence also suggests that the contact resistance is not significant in this case, as compared to the measured values.

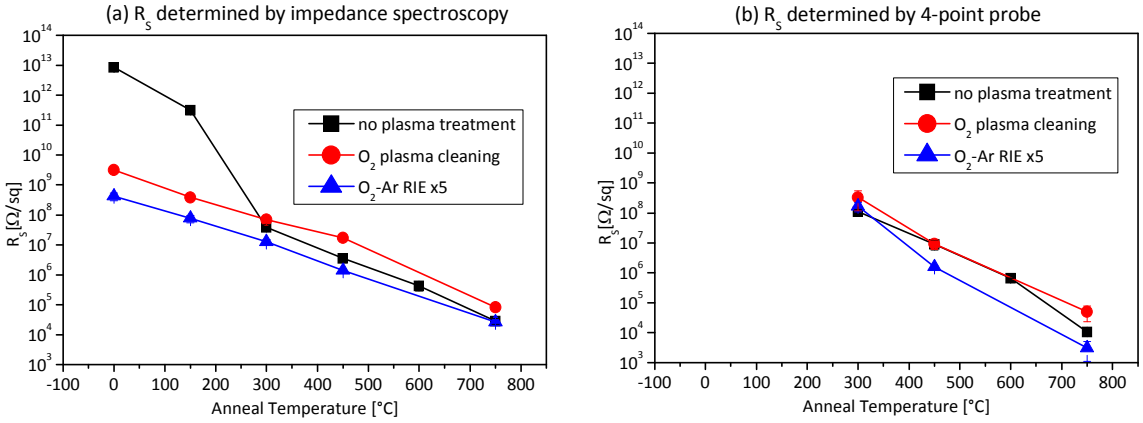

Fig. 7.13: Comparison of sheet resistances determined by (a) impedance spectroscopy at low frequency, and (b) dc 4-point probe method

7.4 Conclusions

Impedance Spectroscopy can be used to get more information about the electrical properties and microstructure of the samples than may be possible by dc measurements alone. The potential for being able to fit semicircles and equivalent circuits to impedance spectra also allows for a reasonable estimation of electrical quantities that may be outside of commonly available dc characterization systems. Impedance spectroscopy analysis of the

colloidal ITO films that were studied suggests a dominant role of interfacial charge transport between ITO nanoparticles in determining the electrical behavior of the ITO films. It also indicated the possibility of intermediate states acting as charge traps and Schottky barriers being manifested in the overall electrical behavior at intermediate frequencies.

Chapter 8:
Conclusions and Future Work

8.1 Conclusions

The dissertation research presented here explored the potential of colloidal ITO nanoparticle-based inks for use in fabricating transparent conducting coatings, patterns and circuits. A non-aqueous synthesis technique was used to synthesize colloidal ITO nanoparticles that were fully crystalline, spheroidal, and had a narrow size distribution between 5-7 nm. ITO films were fabricated from ITO nanoparticle dispersions by spin coating on glass and fused quartz substrates. Although the as-coated films were very transparent, and the ITO nanoparticles themselves are very good conductors, the as-deposited ITO films had poor electrical properties because the passivating ligands on their surface and the inter-particle porosity resulted in poor electrical contacts between the nanoparticles. Annealing at various temperatures was shown to be a simple way to significantly improve the electrical properties of the films, either by burning off the ligands (air annealing) or by thermal decomposition (argon annealing). Annealing at high temperatures (750°C) was shown to decrease the sheet resistance over 8-9 orders of magnitude, from about $10^{13}\,\Omega/\text{sq}$ for as coated films, to almost $10\,\text{k}\Omega/\text{sq}$, which is equivalent to bulk resistivity of $\sim 0.67\ \Omega.\text{cm}$, by establishing electrical percolating paths between the nanoparticles and also by reducing electron scattering via inter-particle necking and densification.

These high temperature annealing treatments are not suitable for non-heat resistant substrates like PET and PEN, which are useful for making flexible panels and displays. Plasma treatments were investigated with the aim of degrading the passivating coatings and improving electrical properties while avoiding very high temperature annealing. A

composite plasma treatment consisting of alternating O_2 RIE and a short Ar RIE was found to be very effective in reducing the sheet resistance of as spin coated ITO films by 4-5 orders of magnitude, from about $10^{13}\Omega$/sq in as-coated films to about $3 \times 10^{8}\Omega$/sq for films that had undergone the composite O_2-Ar RIE x5 plasma treatment, without any annealing. Additional studies were done to investigate the effectiveness of various RIE parameters in removing residual organics and in reducing the sheet resistance of colloidal ITO films. While RIE pressure was observed to be a key parameter, RIE parameters like power, number of alternating O_2-Ar RIE cycles were also effective in reducing the residual organic content. The combination of plasma treatment and annealing over the range of parameters discussed in this dissertation was not able to reduce the sheet resistance of the colloidal ITO films down to the values obtained for sputtered ITO films, likely due to increased scattering from insufficient sintering and nano-scale grain sizes. Nevertheless, in addition to its high transparency, the sheet resistance is approaching 10 kΩ/sq, which is only about an order of magnitude higher than the upper limit of the range of sheet resistance which could be used in the manufacture of capacitive touchscreens (See Fig. 2.2 [12]). If the film thickness is taken into consideration, the lowest resistivity achieved was 0.67 Ω.cm.

Analysis of the impedance spectroscopy data of the colloidal ITO films primarily reflected the behavior of the various interfaces in the measurement system, such as grain boundaries, insulating secondary phases, charge traps, and others. The annealing and plasma treatments were shown to be effective in improving the electrical properties of the colloidal ITO films by over eight orders of magnitude. Efforts to decrease the resistivity to values closer to those achieved by sputtering will need to focus mainly at improving the electrical contact between the particles. This could include novel methods of sintering, or by filling the inter-particle porosity by secondary deposition of ITO by methods such as atomic layer deposition (ALD) [139], or by infiltration in the nanoporosities using an appropriate

solution or sol-gel in an appropriately wetting solvent. Deposition of this additional very thin layer, either from ALD or from solution or sol/gel in areas not desired, could be prevented either by masking or by an appropriate de-wetting pretreatment of those areas. Alternatively a short etching post-treatment all over the substrate can effectively remove the excess ITO deposited elsewhere, while not significantly affecting the TCC thickness (etching of a few angstroms to nanometers on TCCs of around a hundred nanometers, or multiple hundreds of nanometers thick).

8.2 Suggestions for Future Work

(i) The characterization of the microstructure of the colloidal ITO films, and its evolution with processing treatments could not be done in much detail because the very small features (smaller than 10 nm) made characterization by SEM and AFM very difficult. This characterization may be better approached by using electron and neutron scattering methods. Some preliminary results from GISAXS scans on a set of ITO films, shown in Appendix C, suggest that scattering studies like this may prove useful. Detailed microstructural information obtained as a result could be tied in with the electrical and chemical characterization data to better optimize the processing treatments.

(ii) More detailed impedance spectroscopy characterization studies could be done on these films, which could include expanded frequency range, variation of dc bias and ac amplitude, as well as variation of electrode geometry and material. Measuring impedance spectroscopy at various temperatures would also be very useful to get a more detailed picture of the electrical transport processes in these films.

(iii) The plasma processing and annealing techniques discussed in this dissertation can also be applied to other non-ITO materials – especially p-type TCO's like $CuAlO_2$, etc.,

as well as cheaper n-type TCOs like AZO, IGZO, etc. An investigation into how the parameters might affect the properties differently for these materials would be useful.

(iv) Photonic sintering of colloidal ITO films, i.e. sintering using intense light flashes as the source of energy, is a promising technique to achieve film consolidation with minimal heat damage to the substrate. An investigation into the combined use of plasma treatments and photonic sintering could help in the development of an effective technique to attaining good quality transparent conducting films, even on non-heat resistant substrates like polymers.

(v) While the nano-scale size of the ITO nanoparticles is very useful to help with consolidation at lower temperatures, it also tends to increase the sheet resistance by increasing grain boundary scattering. Use of larger ITO particles could help reduce the scattering, but it may be more difficult to consolidate them. A bimodal or even a multimodal size distribution, such that smaller nanoparticles could sit in interstices of larger particles could not only lead to better consolidation, but it could help lower sheet resistances through less grain boundary scattering.

(vi) It may be possible to combine ITO nanoparticles with end-functionalized carbon nanotubes, using appropriately designed/selected ligands on both ITO and CNT, to create a hub and spoke style conducting network, which consists of carbon nanotubes stretched between ITO nanoparticle nodes. This could lead to highly transparent as well as conducting films because of an efficient use of conducting media.

(vii) Printable flexible composites consisting of functionalized nanoparticles of latex (or other polymer like PDMS, PAN, PET) with ITO nanoparticles could be developed.

Appendix A:
Effect of Annealing on Sputtered Films

As discussed in chapter 2, current ITO deposition techniques require the substrates to be heated to a relatively high temperature during deposition in order to achieve crystallization and conductivity enhancement in the ITO films [44, 45]. If sputter deposition of ITO is done on unheated substrates, as in the case of done roll-to-roll sputtering of ITO on polymer films, the resulting ITO films have inferior electro-optical properties [46, 140]. The study [112] presented in this appendix investigates the properties of ITO films sputtered without any substrate heating (cold-sputtering), and the effect of post-deposition heat treatment on these cold-sputtered ITO films.

A.1 Fabrication

ITO films were fabricated by cold-sputtering at radio frequencies (RF-sputtering) onto cleaned glass substrates (0.5" × 0.5" pieces of borosilicate glass microscope slides from VWR) and quartz substrates (0.5" × 0.5" pieces of quartz microscope slides from Quartz Scientific). The sputtering was done using a Kurt Lesker PVD 75 sputter coater in an atmosphere of 50% O2 + 50% Ar at a pressure of 5 mTorr, using 150W of power. No external substrate heating was used. However, it is estimated that the substrates may have been heated to a temperature in the vicinity of 65°C due to the heat generated by the sputtering process. An ITO sputter target with a tin content equivalent to 10 weight% of SnO_2 was used.

Fig. A.1: PVD-75 sputter coater

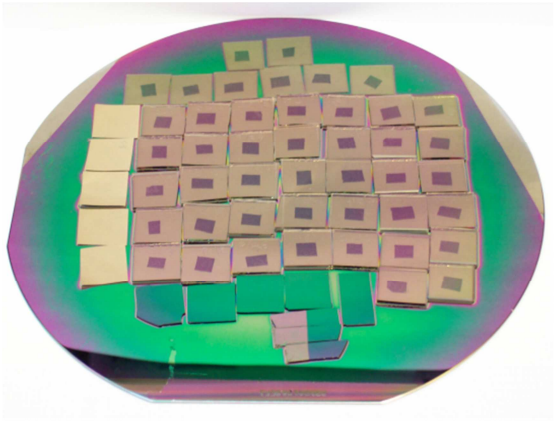

Fig. A.2: Cold-sputtered ITO films mounted on Si wafer

A.2 Heat Treatment

These sputtered ITO films were annealed in an atmosphere of ultra-high purity (UHP) grade argon (Airgas) or Ultra-zero grade commercial air (Airgas) at three different temperatures – 150°C, 300°C and 450°C, for 48 minutes. The two gas atmospheres were chosen in order to have heat treatments done in different oxygen partial pressures.

A.3 Characterization

The film thickness was determined using non-contact atomic force microscopy (NC-AFM) to be around 400 nm. The as-deposited ITO films were subjected to in situ X-ray diffraction scans while being heated to various temperatures to monitor the changes from the amorphous to the crystalline state. Topography characterization of the cold-sputtered ITO films was done using a Zeiss Ultra60 scanning electron microscope. The DC resistance of sputtered ITO films was determined using the delta mode measurements[141] using a four-point probe set-up, a Keithley 2182A nanovoltmeter and a Keithley 6221 AC-DC current source.

A.4 Results and Discussion

Fig. A.3 shows the variation of the visible light transmittance in the sputtered ITO films deposited on glass and quartz substrates. The visual appearance of the sputtered films with heat treatment can be seen in the inset.

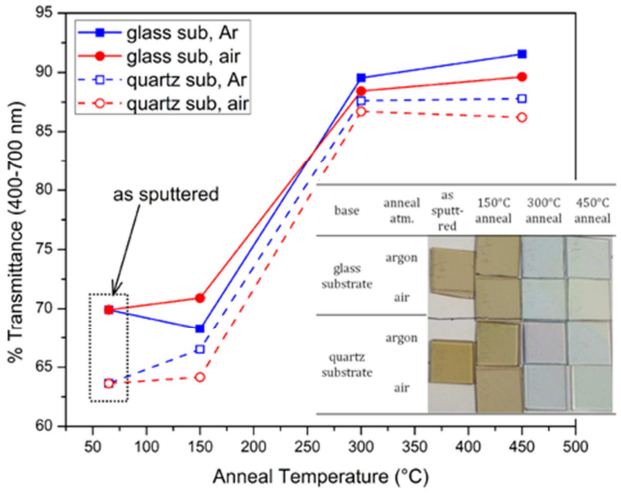

Fig. A.3: Transmittance of cold-sputtered ITO films. Inset: Visual appearance of sputtered ITO films subjected to annealing as indicated

It can be concluded that since the as cold-sputtered ITO films and the films heat treated at 150°C were brown, they had significantly less transmittance than those heat treated at higher temperatures. Fig. A.4 (a) displays XRD patterns taken at selected temperatures for a cold-sputtered ITO film, which was heated in situ in ambient air. It can be seen that when the film was heated to temperatures less than 180°C, it remained amorphous, and that crystallization, as detected by the appearance of X-ray diffraction peaks, occurs between 180 and 200°C. Fig. A.4 (b) shows the variation of crystallite size with annealing temperature, as calculated using the Scherrer formula using the most intense (222) peaks. It can be seen that crystallization and crystallite growth occurs between 180°C and 220°C. The as-sputtered ITO films and those heat treated at 150°C were thus determined to be amorphous. This explains their dark appearance, because amorphous ITO has a disordered structure, and has trap states, which absorb visible light [142]. The cold-sputtered films annealed at 300°C and above, were crystalline and as a result, were transparent and have high transmittance.

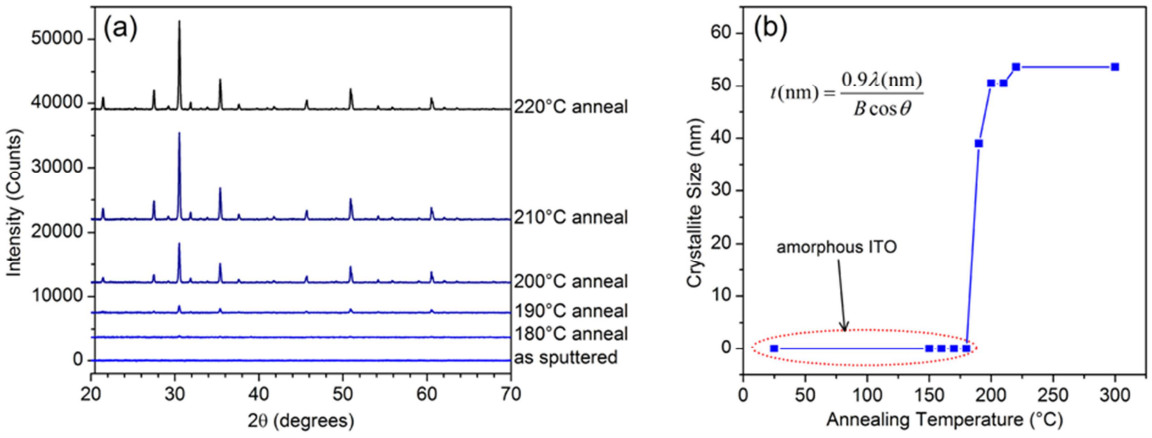

Fig. A.4: (a): XRD patterns of cold-sputtered ITO deposited on quartz substrate with in-situ heating to various temperatures. Appearance of X-ray peaks, indicating crystallization occurs at 190°C. (b): Variation of grain size of cold-sputtered ITO with heating,

Fig. A.5 (a) and (b) show the variation of the DC resistivity as a function of the annealing temperatures, for the cold-sputtered ITO films deposited on glass and quartz substrates, respectively. The resistivity of ITO films, deposited on glass substrate and annealed in argon, decreased with an increase in the annealing temperature. In contrast, the resistivity of ITO films annealed in air increased with an increase in the annealing temperature. This agrees well with the current understanding of the defect structure of ITO, which has been studied and modeled by Frank and Köstlin [18], González et al. [19] and others [17, 21-24]. When the In_2O_3 lattice is doped with SnO_2, Sn^{4+} ions substitute for In^{3+} ions, to form various Sn-O clusters, which can be either reducible or non-reducible. The reducible cluster, $(2SnIn^{\bullet} Oi")^{\times}$, is a loosely bound cluster [19]. Reduction of these reducible clusters is the dominant charge carrier generation mechanism in ITO [17]. This may also be thought of as the "activation" of the donor species. As a result, oxidizing conditions normally decrease the carrier concentration [17], and conversely, low oxygen partial pressure conditions can be expected to result in an increase in the carrier concentration in ITO.

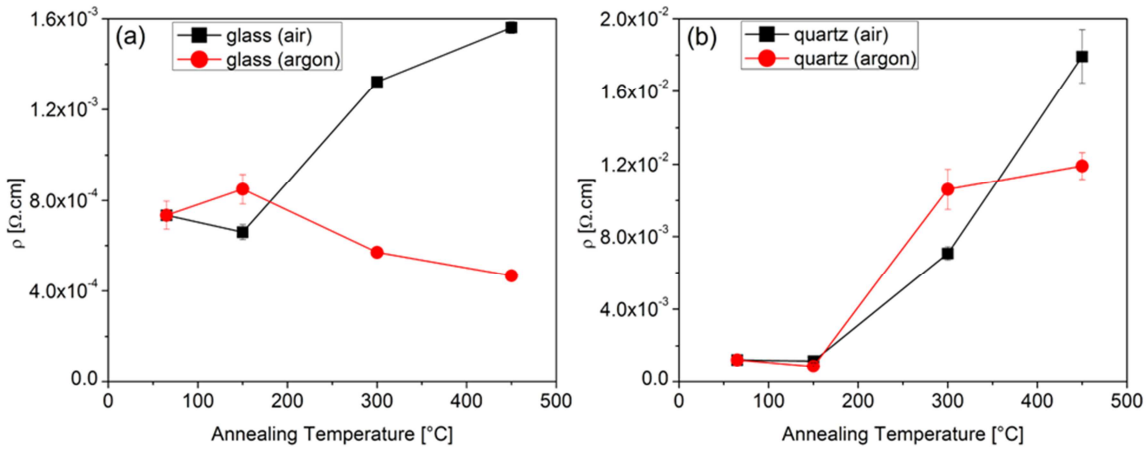

Fig. A.5: DC resistivity of sputtered ITO films vs. heat treatment: (a) Sputtered ITO on glass substrates, annealed in argon / air, (b) Sputtered ITO on quartz substrates, annealed in argon/air [90]

However, the films annealed at 150°C did not obey the general trend (Fig. A.5 (a)). This seemingly anomalous behavior was seen to be reproducible, as was observed with a separate set of cold-sputtered films subject to identical annealing treatments. Morikawa et al. [143] have reported that cold-sputtered ITO films are essentially amorphous with some crystalline nuclei, which grow upon annealing until the film is completely crystallized. Since the ITO films annealed at 150°C have been heated to temperatures just below the crystallization temperature (180-220°C) as described earlier and shown in Fig. A.4 (a)), it is thought that the microstructure may have islands of crystalline phases in the amorphous matrix thus causing the unexpected trend. The presence of two phases can be expected to increase the scattering and reduce the mobility. At the same time, the onset of crystallization activates the tin dopants and increases the carrier concentration. It is thought that this interplay of changes in the carrier concentration and mobility just before complete crystallization could be a reason for the anomalous behavior of films annealed at 150°C.

The variation of electrical resistivity with annealing of ITO films sputter deposited on quartz substrates was quite different from that of ITO films on glass substrates (see Fig. A.5 (b)). Films annealed at 300°C and 450°C were observed to increase in resistivity by over an order of magnitude. The variation in carrier concentration with annealing cannot explain this. Fig. A.6 (a)-(d) and (e)-(h) show SEM images of ITO films sputtered on glass and quartz substrates, respectively. It can be seen that the films annealed at 300°C and 450°C have developed cracks, while those deposited on glass substrates do not show any sign of fracture after identical annealing treatments. This is a consequence of thermal expansion mismatch between ITO, which has an expansion coefficient of 8.5×10^{-6}/°C [110] and fused quartz, which has an expansion coefficient of 0.55×10^{-6}/°C [111].

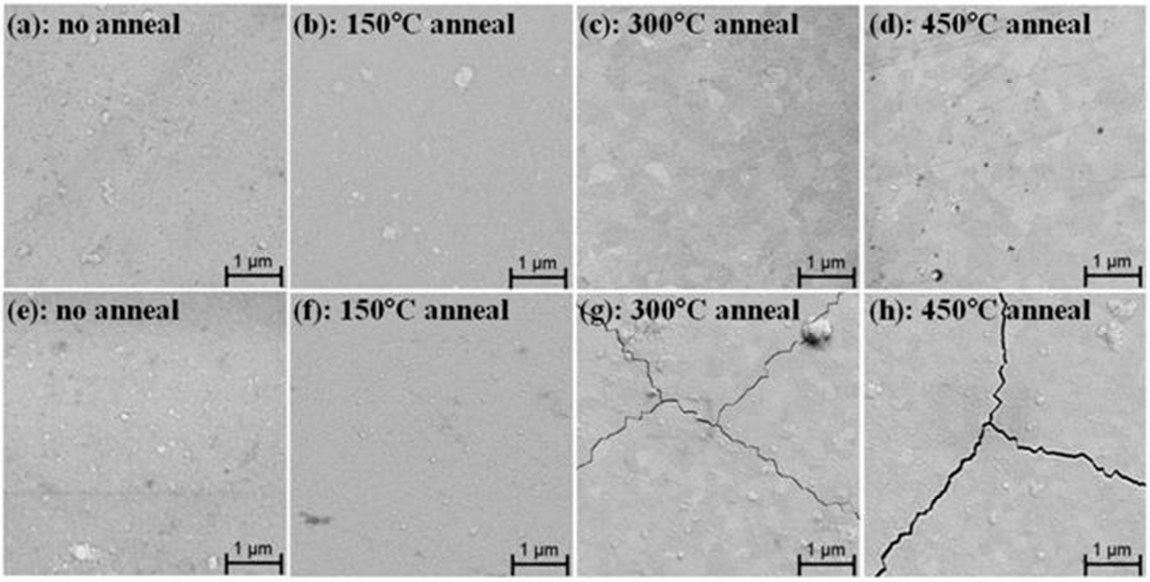

Fig. A.6: SEM images of cold-sputtered ITO on glass (a-d) and quartz (e-h) substrates after annealing at various temperatures in UHP argon [90]

Appendix B:
Additional Impedance Spectroscopy Plots

The impedance spectra of the colloidal ITO films studied in plasma study 1 are presented in this appendix, for various annealing temperatures in air and argon atmospheres in the form of Bode plots (magnitude, phase angle, real, imaginary), and Nyquist plots (traditional Nyquist plots, and log-log plots of absolute impedance).

B.1 Bode Plots

In the Bode plots in Fig. B.1 to Fig. B.6, (a) *Z* magnitude, (b) real *Z*, (c) phase angle of *Z*, and (d) imaginary *Z* are presented against frequency for various annealing temperatures.

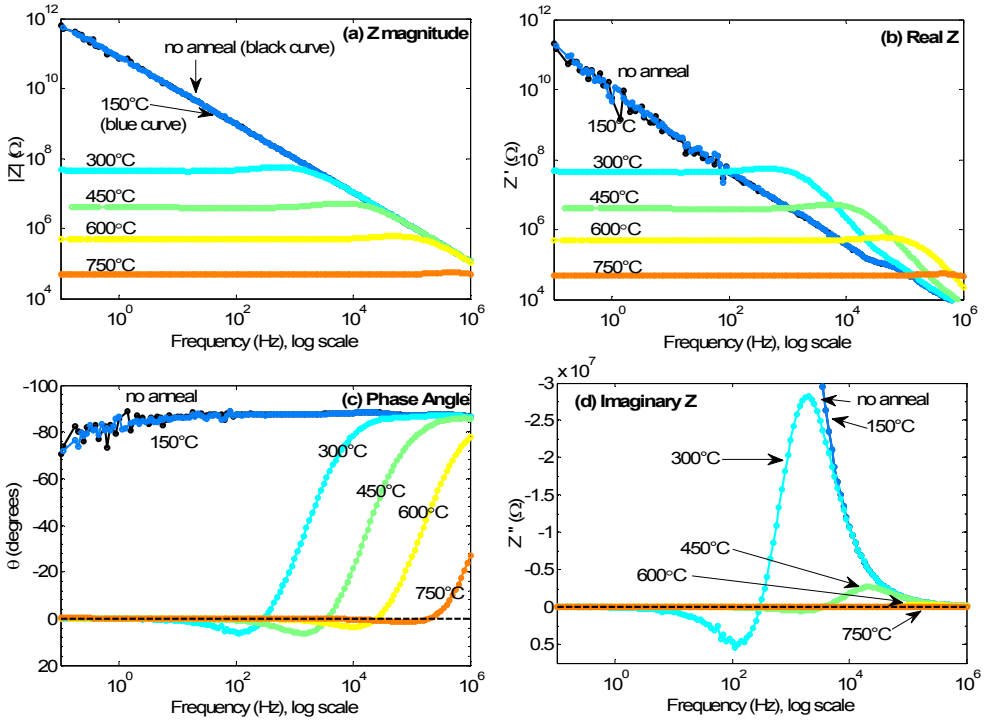

Fig. B.1: Bode plots: No plasma, air anneal

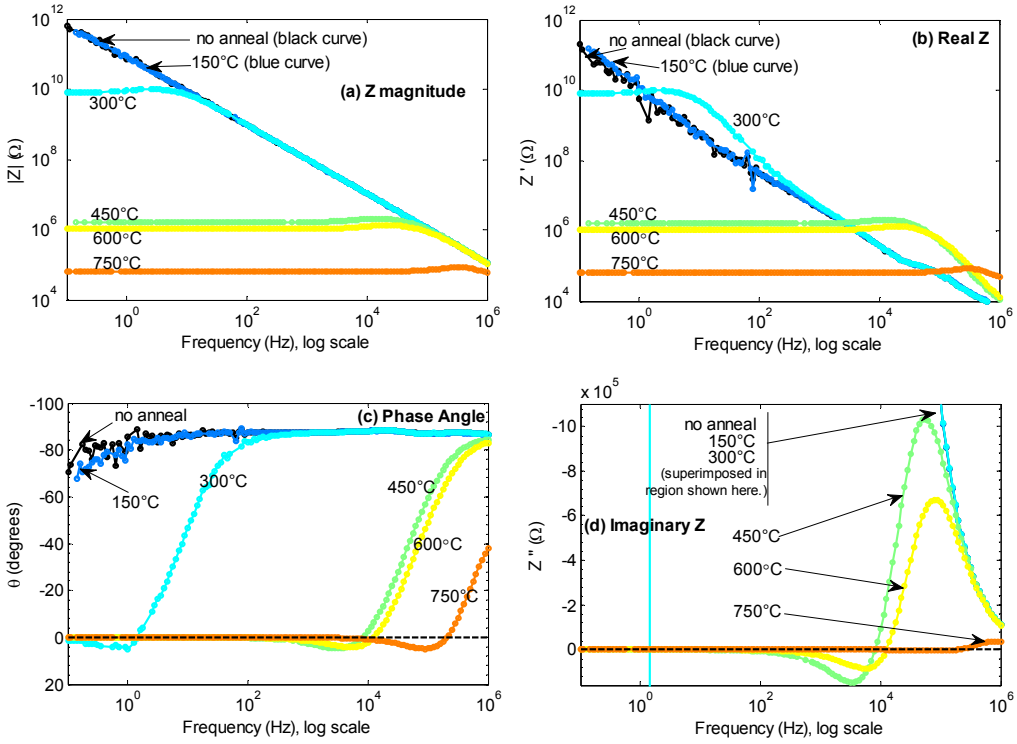

Fig. B.2: Bode plots: No plasma, argon anneal

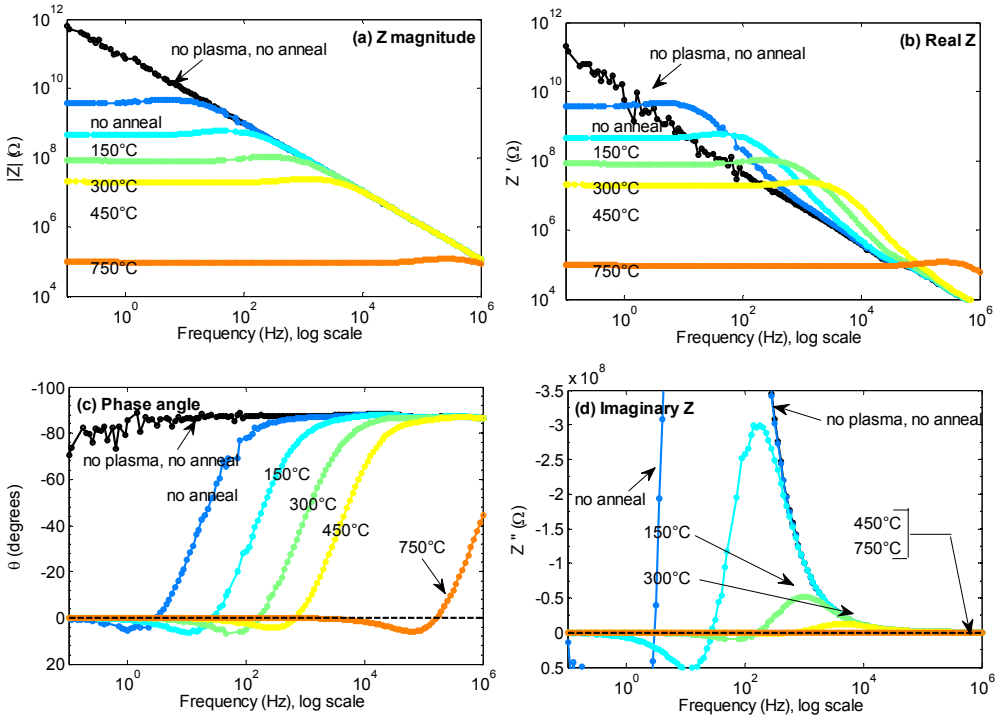

Fig. B.3: Bode plots: O_2 plasma cleaning, air anneal

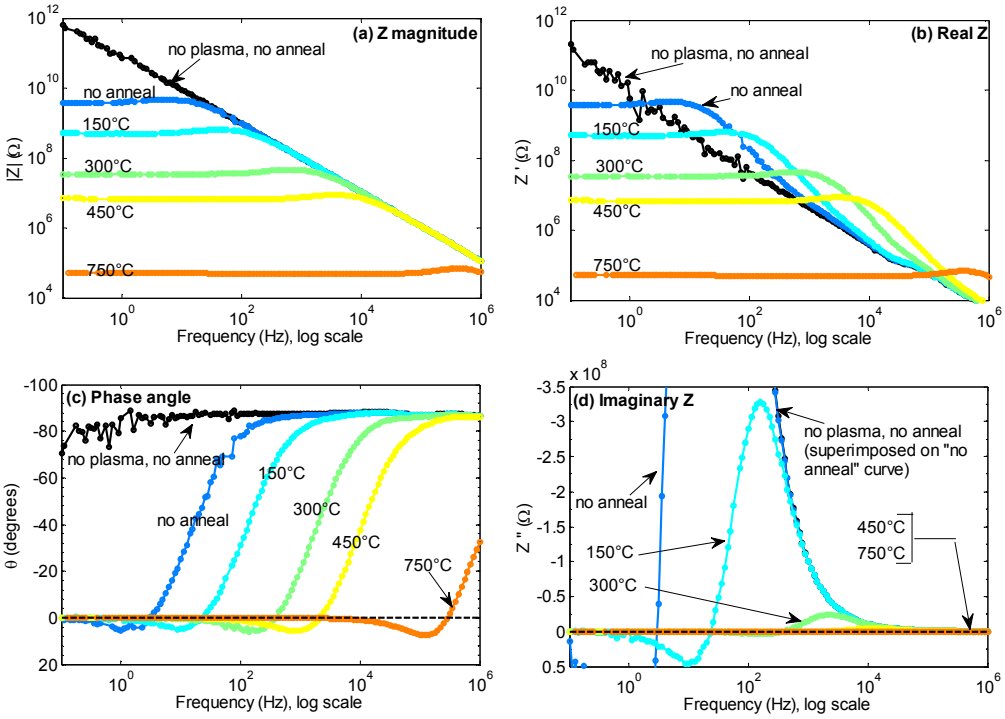

Fig. B.4: Bode plots: O_2 plasma cleaning, argon anneal

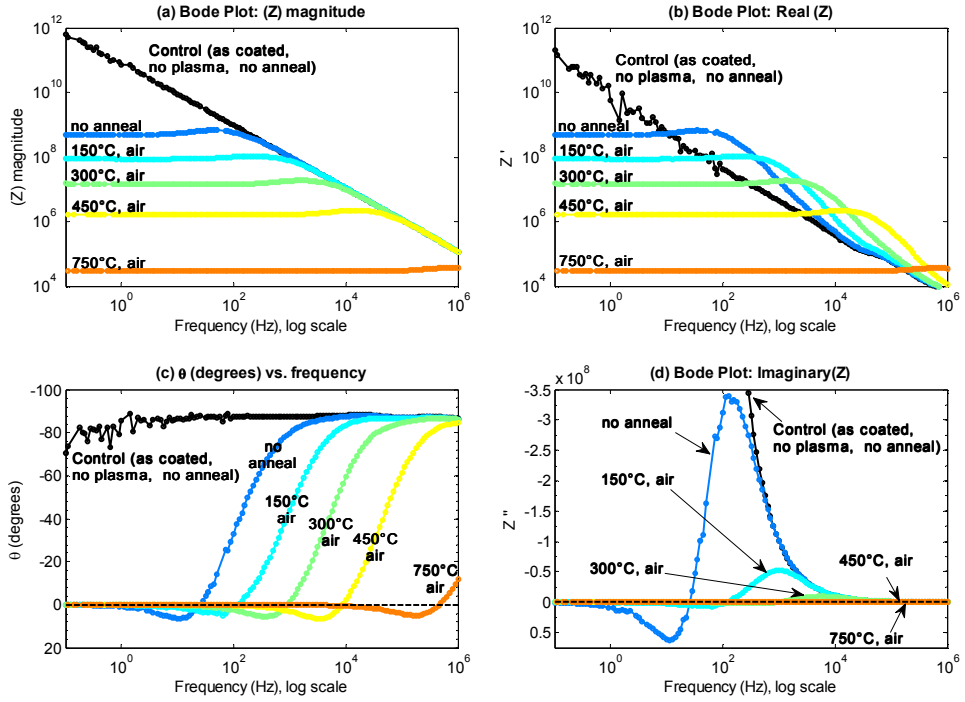

Fig. B.5: (Same as Fig. 7.3) Bode plots: O_2-Ar RIE x5, air anneal

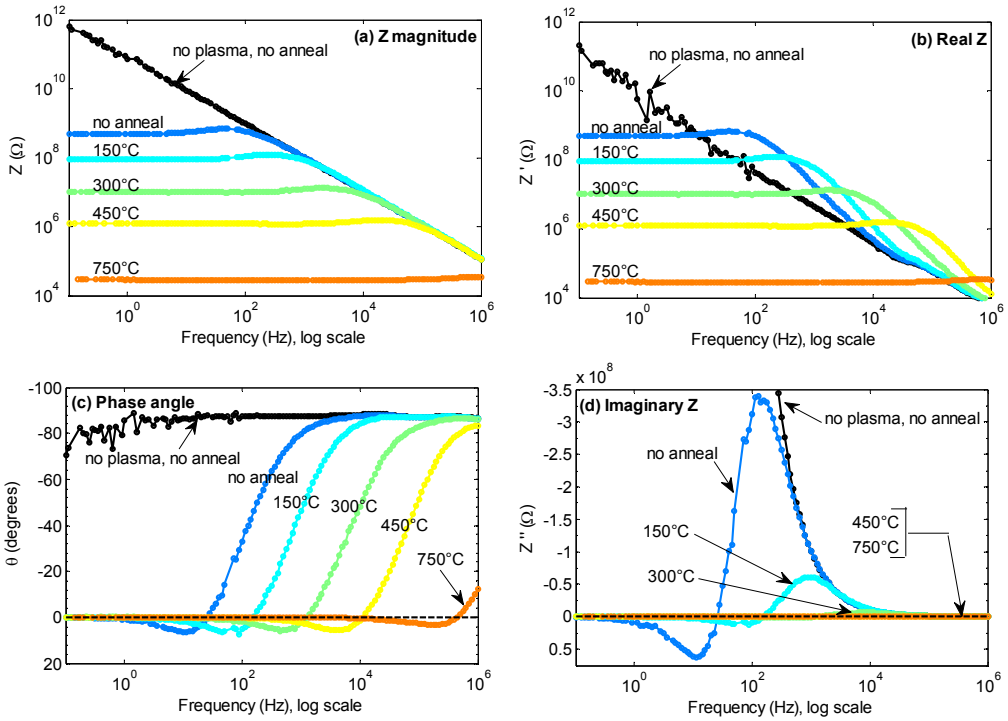

Fig. B.6: Bode plots: O_2-Ar RIE x5, argon anneal

B.2 Nyquist Plots

The Nyquist plots of impedance have been presented below from Fig. B.7 to Fig. B.12. Each plot is presented at four different scales in order to show all the curves, which vary by orders of magnitude. These are followed by presenting the Nyquist plots in log-log scale, obtained by plotting the absolute values of the real and imaginary parts of impedance, from Fig. B.13 to Fig. B.15.

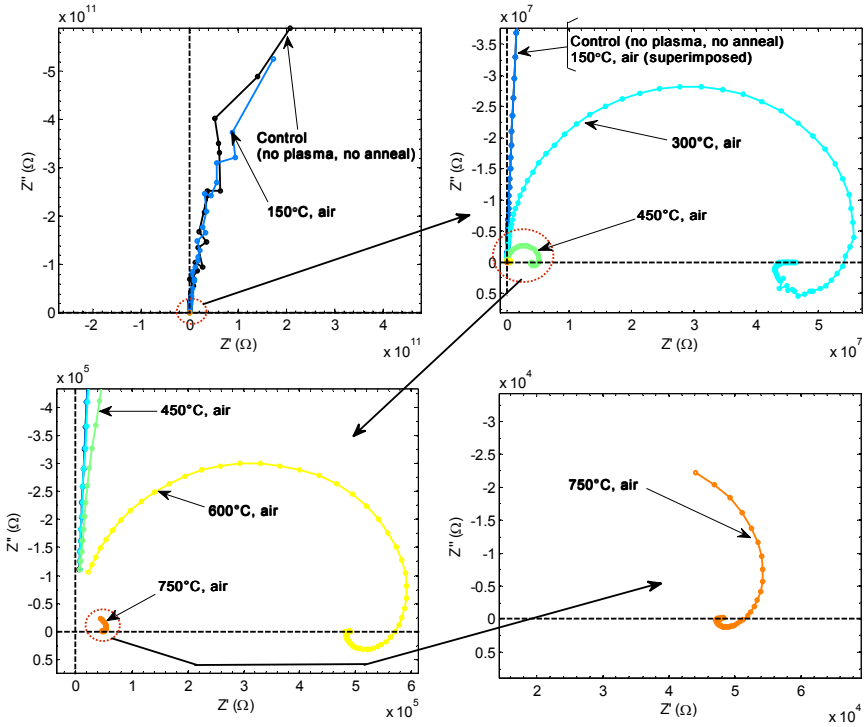

Fig. B.7: Nyquist plots: no plasma, air anneal

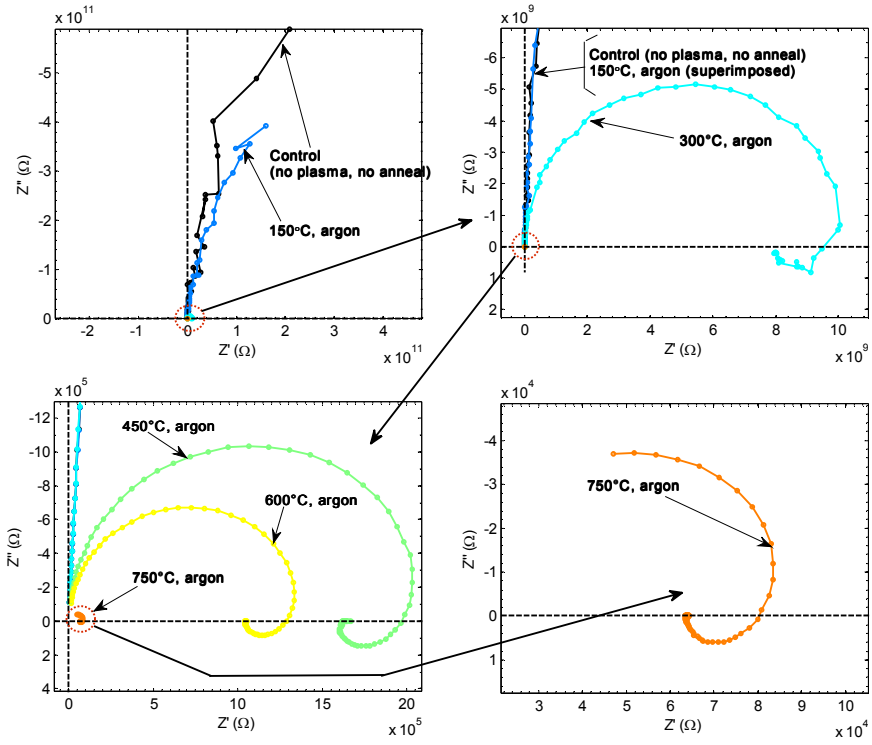

Fig. B.8: Nyquist plots: no plasma, argon anneal

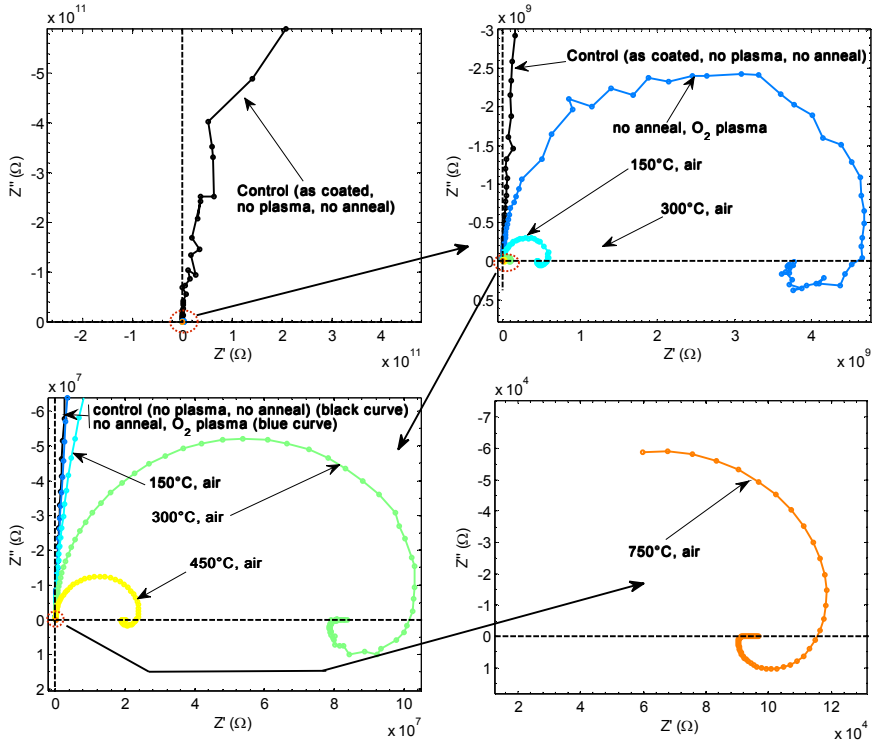

Fig. B.9: Nyquist plots: O_2 plasma cleaning, air anneal

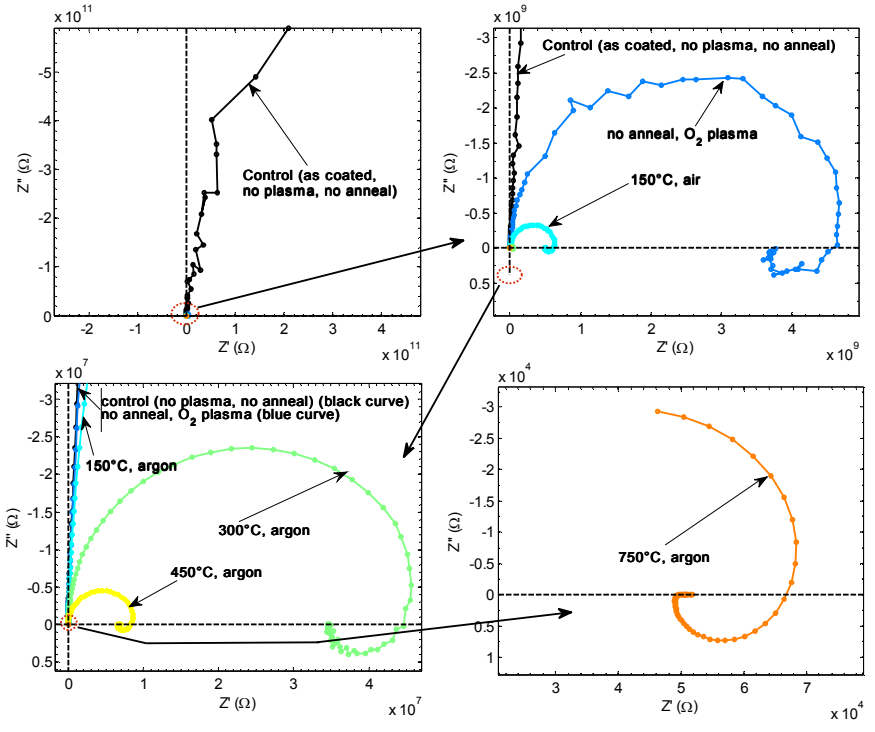

Fig. B.10: Nyquist plots: O_2 plasma cleaning, argon anneal

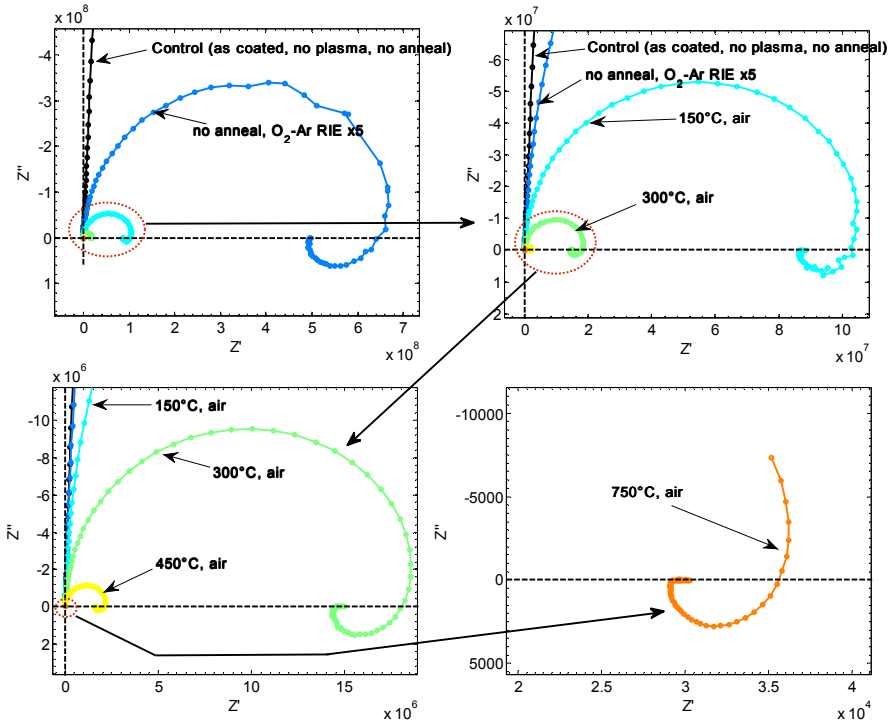

Fig. B.11: (Same as Fig. 7.1) Nyquist plots: O_2–Ar RIE x5, air anneal

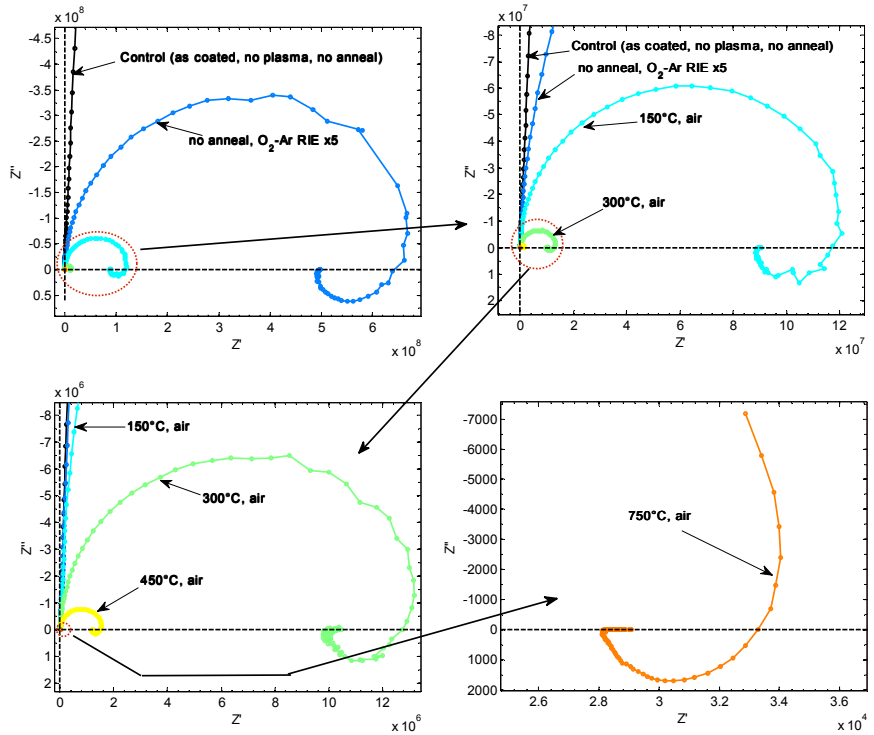

Fig. B.12: Nyquist plots: O_2–Ar RIE x5, argon anneal

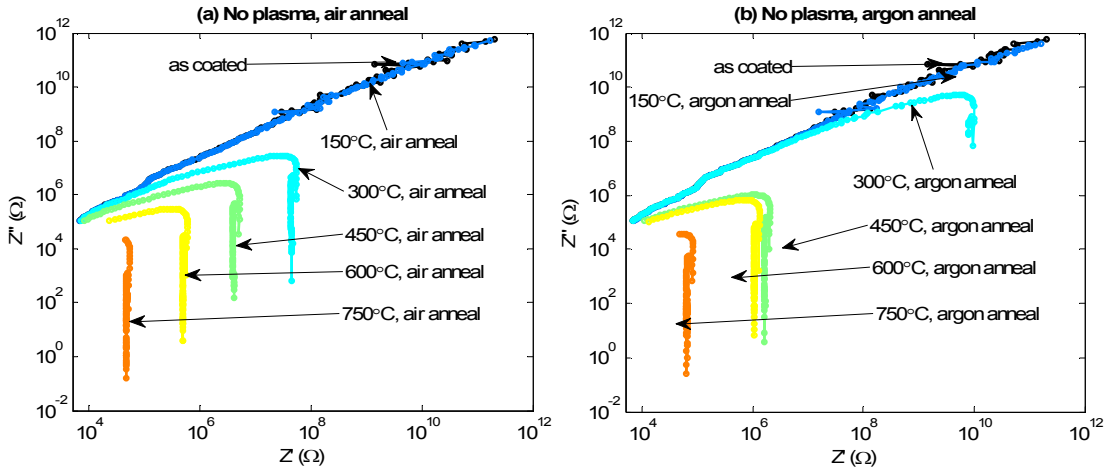

Fig. B.13: Nyquist plots on log-log scale: no plasma, (a) air anneal, (b) argon anneal

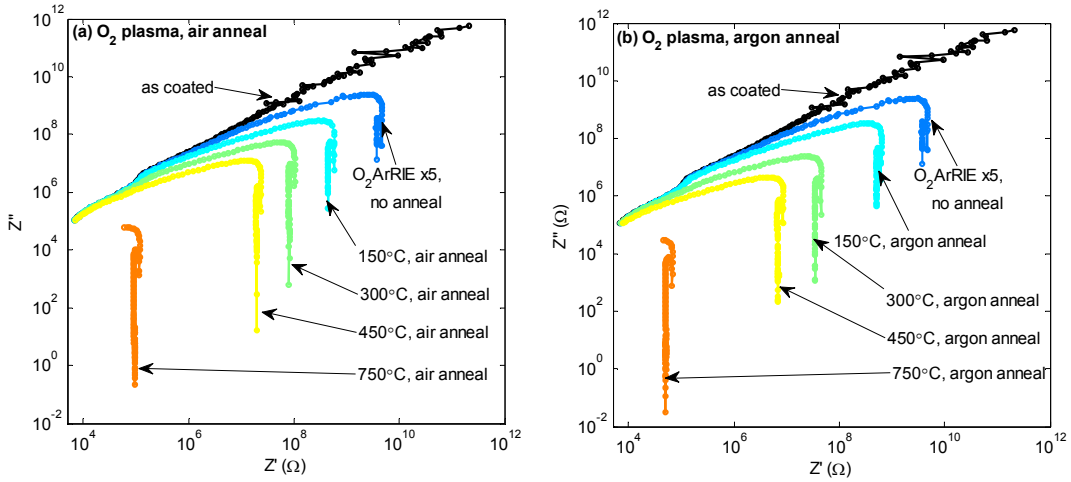

Fig. B.14: Nyquist plots on log-log scale: O_2 plasma, (a) air anneal, (b) argon anneal

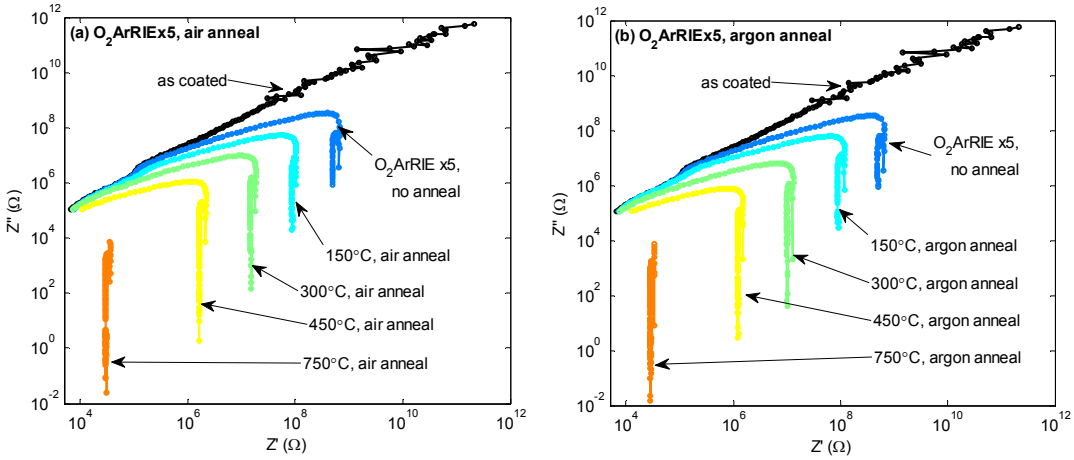

Fig. B.15: Nyquist plots on log-log scale: O_2-Ar RIE x5, (a) air anneal, (b) argon anneal

B.3 Fitted equivalent circuits

The variation of the discrete elements for the nested RCRL and RCRC circuits shown in Fig. 7.6, for the colloidal ITO films in plasma study 1, as a function of the temperature of annealing in air or argon after the plasma treatment under consideration, are presented in Fig. B.16 (a) to (f). The dashed curves indicate that they are plotted against the secondary Y-axis to the right of the plot. The frequency range of the impedance spectra of the non-plasma treated films without annealing, and for the film annealed at 150°C in air is not enough to allow a good circuit fitting. Hence the $R1$ in the equivalent circuits has been represented by the low frequency resistance for those films.

The variation of the time constants with annealing temperature in air, as calculated by the expressions:

$$\tau_i = R_i C_i \text{ (for RC element) or } \tau_i = \frac{L_i}{R_i} \text{ (for RL element)}$$

for the RC and RL elements in the nested RCRL and nested RCRC equivalent circuits are presented in Fig. B.17, for colloidal films (a) with no plasma treatment, (b) with O_2 plasma cleaning, (c) with O_2-Ar RIE x5 treatment.

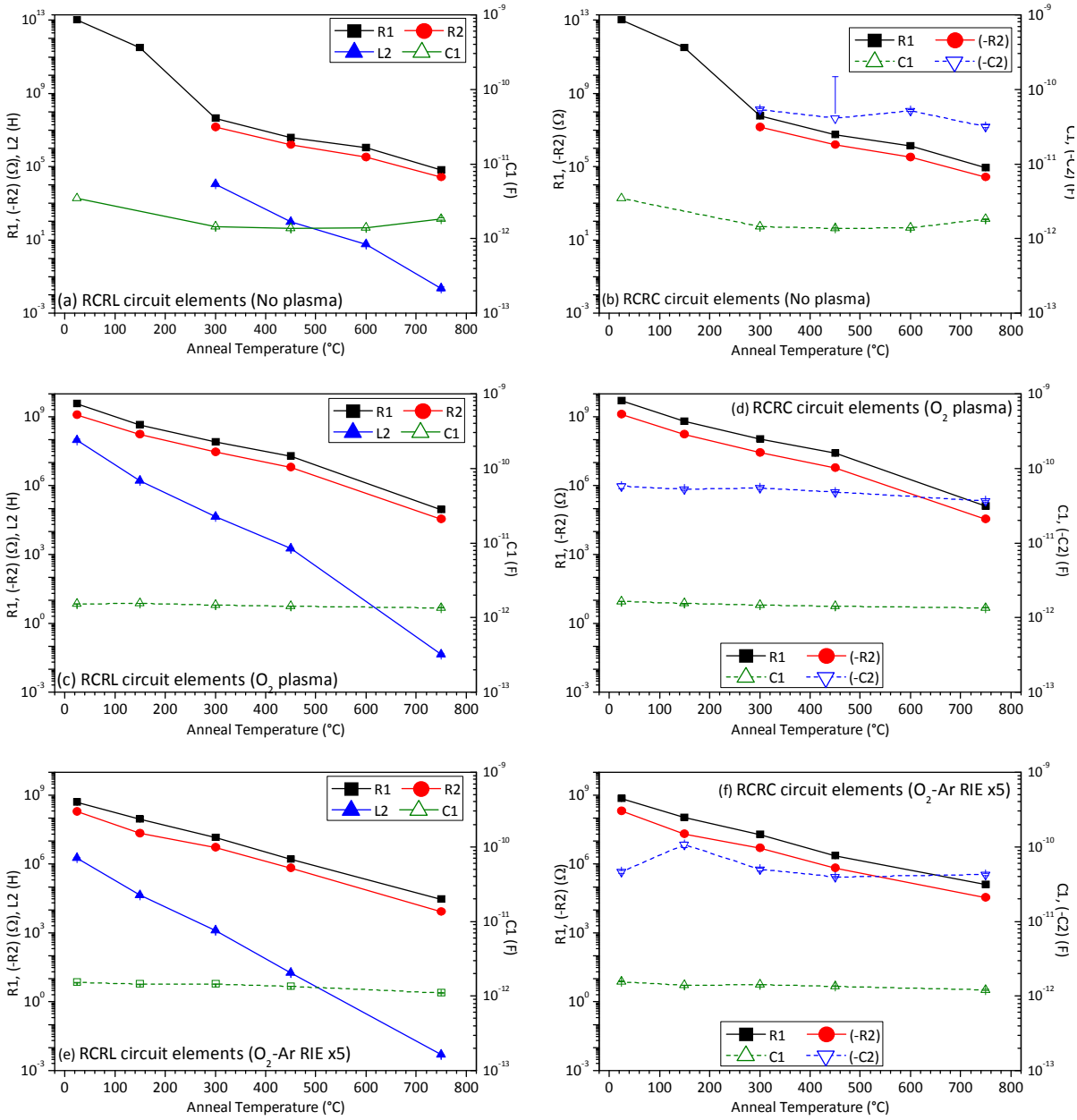

Fig. B.16: Variation of the discrete electrical circuit elements.
No plasma: (a) nested RCRL eq ckt, (b) nested RCRC eq ckt
O_2 plasma cleaning: (c) nested RCRL eq ckt, (d) nested RCRC eq ckt
O_2-Ar RIE x5: (e) nested RCRL eq ckt, (f) nested RCRC eq ckt

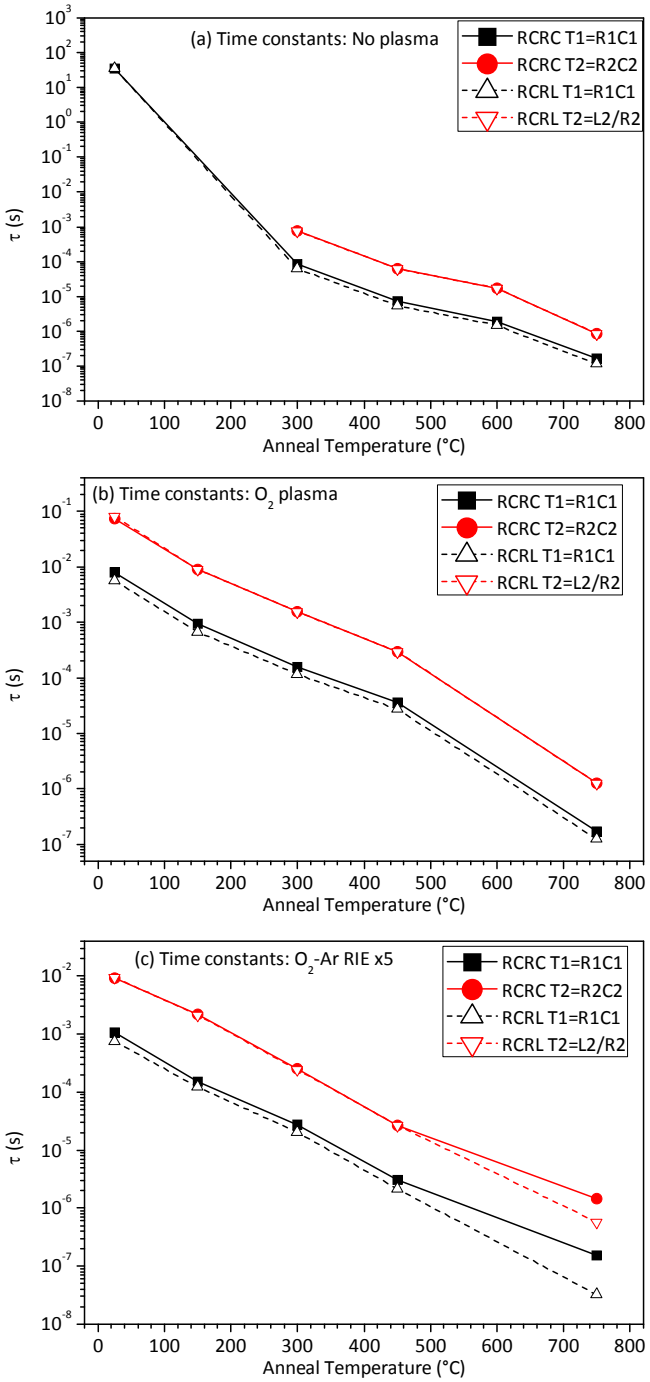

Fig. B.17: Variation of the time constants, calculated by $\tau_i = R_i C_i$ or $\tau_i = L_i/R_i$ for the RC and RL elements in the nested RCRL and nested RCRC equivalent circuits, with annealing temperature in air, for ITO films annealed in air after (a) no plasma, (b) O_2 plasma cleaning, (c) O_2-Ar RIE x5 treatment

Appendix C:
GISAXS results

GISAXS characterization was done on colloidal ITO films deposited on fused quartz and glass substrates in order to understand the microstructural evolution of the colloidal ITO films. The characterization was done on a Anton-Parr SAXS machine, using Cu Kα radiation, of wavelength 1.5418Å. A point focus was used, in order to obtain information from non-specular scattering, as opposed to a line focus, which may be used for a pure reflectivity measurement. An angle of incidence of 0.35° was used. The 2-D scattered intensity patterns as collected on the sensor plate are shown in Fig. C.1 to Fig. C.4. The analysis of these results was not completed at the time of writing this dissertation.

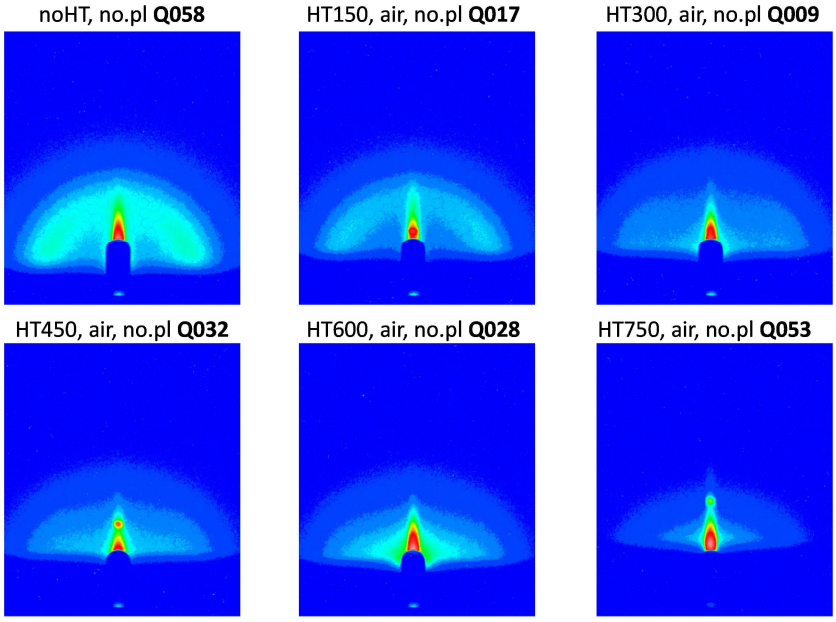

Fig. C.1: GISAXS patterns of colloidal ITO on fused quartz without any plasma treatment, for various annealing temperatures in air. (1st row, L-R: no anneal, 150°C anneal, 300°C anneal. 2nd row, L-R: 450°C anneal, 600°C anneal, 750°C anneal)

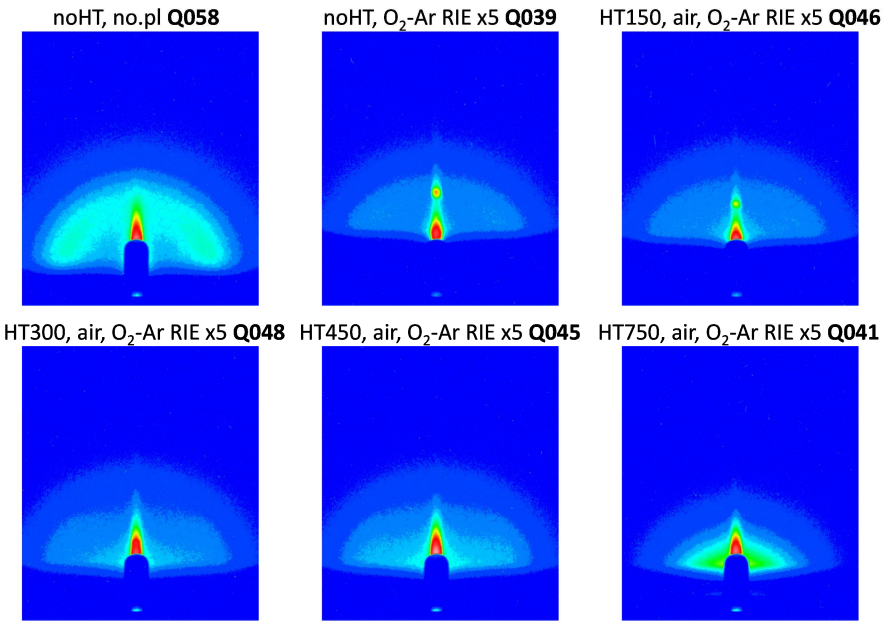

Fig. C.2: GISAXS patterns of colloidal ITO on fused quartz after O_2-Ar RIE x5 plasma treatment, for various annealing temperatures in air. (1st row, L-R: no anneal, 150°C anneal, 300°C anneal. 2nd row, L-R: 450°C anneal, 600°C anneal, 750°C anneal)

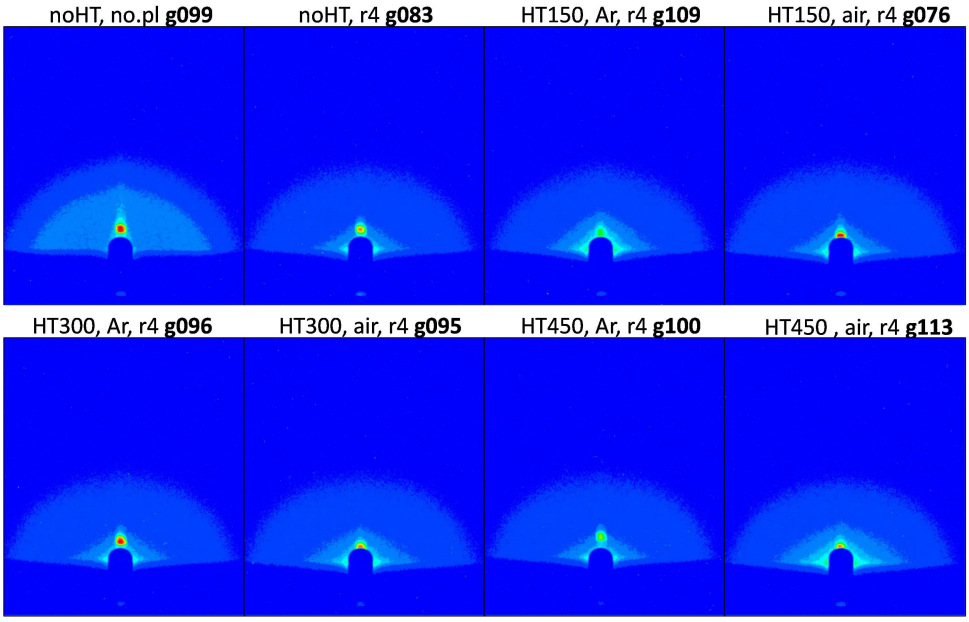

Fig. C.3: GISAXS patterns of colloidal ITO on glass, after the recipe 4 (r4) plasma treatment from plasma study 2, for various annealing temperatures (1st row, L-R: no anneal and no plasma, r4+no anneal, r4+150°C argon, r4+150°C air. 2nd row, L-R: r4+300°C argon, r4+300°C air, r4+450°C argon, r4+450°C air)

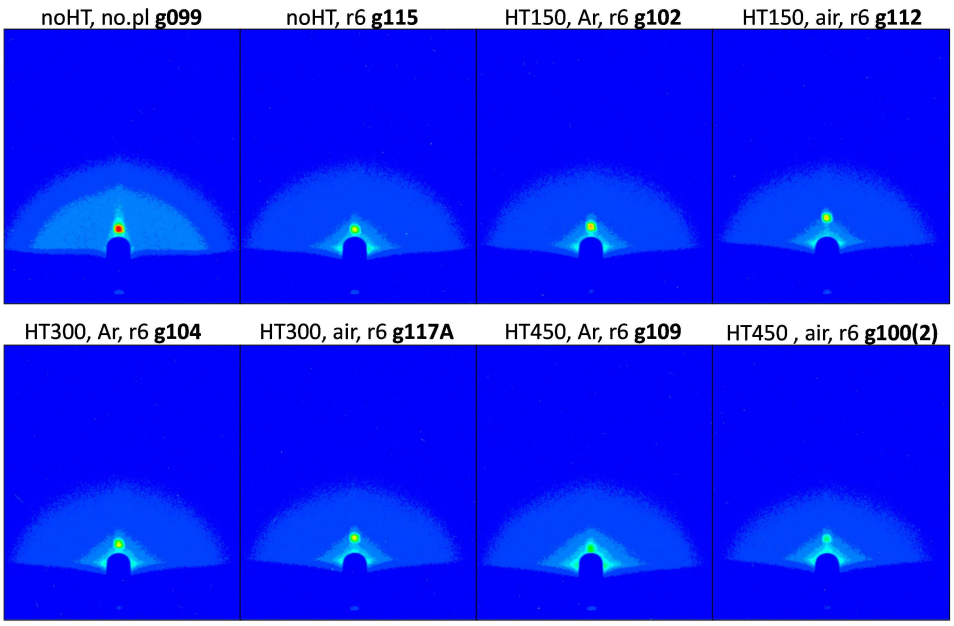

Fig. C.4: GISAXS patterns of colloidal ITO on glass, after the recipe 6 (r6) plasma treatment from plasma study 2, for various annealing temperatures (1st row, L-R: no anneal and no plasma, r6+no anneal, r6+150°C argon, r6+150°C air. 2nd row, L-R: r6+300°C argon, r6+300°C air, r6+450°C argon, r6+450°C air)

References

[1] R. G. Gordon, "Criteria for choosing transparent conductors", MRS Bulletin, vol. 25, no. 8, pp. 52-57, 2000.

[2] B. G. Lewis and D. C. Paine, "Applications and Processing of Transparent Conducting Oxides", MRS Bulletin, vol. 25, no. 8, pp. 22-27, 2000.

[3] J. K. Fink, "Poly(naphthalates)", in High Performance Polymers Norwich NY: William Andrew Publishing, 2008.

[4] C. J. Capozzi, I. N. Ivanov, S. Joshi, and R. A. Gerhardt, "The effect of the atmosphere on the optical properties of as-synthesized colloidal indium tin oxide", Nanotechnology, vol. 20, no. 14, p. 145701, 2009.

[5] X. C. Wu, L. F. Chi, and H. Fuchs, "Patterning of Semiconductor Nanoparticles via Microcontact Printing", European Journal of Inorganic Chemistry, vol. 2005, no. 18, pp. 3729-3733, 2005.

[6] S. Y. Chou, P. R. Krauss, and P. J. Renstrom, "Nanoimprint lithography", in 40th International Conference on Electron, Ion, Photon Beam Tech and Nanofabrication, Atlanta, GA, USA, 1996, pp. 4129-4133.

[7] C. A. Bulthaup, E. J. Wilhelm, B. N. Hubert, B. A. Ridley, and J. M. Jacobson, "All-additive fabrication of inorganic logic elements by liquid embossing", Applied Physics Letters, vol. 79, no. 10, pp. 1525-1527, 2001.

[8] S. B. Fuller, E. J. Wilhelm, and J. M. Jacobson, "Ink-jet printed nanoparticle microelectromechanical systems", Journal of Microelectromechanical Systems, vol. 11, no. 1, pp. 54-60, 2002.

[9] B. A. Ridley, B. Nivi, and J. M. Jacobson, "All-inorganic field effect transistors fabricated by printing", Science, vol. 286, no. 5440, pp. 746-749, 1999.

[10] K. L. Chopra, S. Major, and D. K. Pandya, "Transparent conductors-a status review", Thin Solid Films, vol. 102, pp. 1-46, 1983.

[11] K. Badekar, Annals of Physics (Leipzig), vol. 22, p. 749, 1907.

[12] I. N. Ivanov, M. P. Garrett, and R. A. Gerhardt, "Carbon Nanotube Assemblies for Transparent Conducting Electrodes", in Nanoscale Applications for Information and Energy Systems, A. Korkin and D. J. Lockwood, Eds.: Springer New York, 2013, pp. 117-148.

[13] D. B. Fraser and H. D. Cook, " Highly Conductive, Transparent Films of Sputtered $In_{2-x}SnxO_{3-y}$", Journal of the Electrochemical Society, vol. 119, no. 10, pp. 1368-1374, 1972.

[14] G. Haacke, "Transparent Conducting Coatings", Annual Review of Materials Science, vol. 7, pp. 73-93, 1977.

[15] S. Nudelman and S. S. Mitra, in Optical Properties of Solids New York: Plenum Press, 1969.

[16] S. H. Brewer and S. Franzen, "Calculation of the electronic and optical properties of indium tin oxide by density functional theory", Chemical Physics, vol. 300, no. 1-3, pp. 285-293, 2004.

[17] N. Nadaud, N. Lequeux, M. Nanot, J. Jove, and T. Roisnel, "Structural Studies of Tin-Doped Indium Oxide (ITO) and $In_4Sn_3O_{12}$", Journal of Solid State Chemistry, vol. 135, no. 1, pp. 140-148, 1998.

[18] G. Frank and H. Köstlin, "Electrical properties and defect model of tin-doped indium oxide layers", Applied Physics A: Materials Science & Processing, vol. 27, no. 4, pp. 197-206, 1982.

[19] G. B. Gonzalez, T. O. Mason, J. P. Quintana, O. Warschkow, D. E. Ellis, J. H. Hwang, J. P. Hodges, and J. D. Jorgensen, "Defect structure studies of bulk and nano-indium-tin oxide", Journal of Applied Physics, vol. 96, no. 7, pp. 3912-3920, 2004.

[20] K. E. Gonsalves, S. P. Rangarajan, and J. Wang, "Chemical Synthesis of Nanostructured Metals, Metal Alloys and Semiconductors", in Nanostructured Materials and Nanotechnology. vol. 1: Synthesis and Processing, H. S. Nalwa, Ed.: Academic Press, 2000, pp. 1-52.

[21] I. Hamberg, C. G. Granqvist, K. F. Berggren, B. E. Sernelius, and L. Engström, "Band-gap widening in heavily Sn-doped In_2O_3", Physical Review B, vol. 30, no. 6, pp. 3240-3249, 1984.

[22] O. Warschkow, D. E. Ellis, G. B. Gonzalez, and T. O. Mason, "Defect Structures of Tin-Doped Indium Oxide", Journal of the American Ceramic Society, vol. 86, no. 10, pp. 1700-1706, 2003.

[23] O. Warschkow, D. E. Ellis, G. B. Gonzalez, and T. O. Mason, "Defect cluster aggregation and nonreducibility in tin-doped indium oxide", Journal of the American Ceramic Society, vol. 86, no. 10, pp. 1707-1711, 2003.

[24] O. Warschkow, L. Miljacic, D. E. Ellis, G. Gonzalez, and T. O. Mason, "Interstitial oxygen in tin-doped indium oxide transparent conductors", Journal of the American Ceramic Society, vol. 89, no. 2, pp. 616-619, 2006.

[25] A. J. Freeman, K. R. Poeppelmeier, T. O. Mason, R. P. H. Chang, and T. J. Marks, "Chemical and thin-film strategies for new transparent conducting oxides", MRS Bulletin, vol. 25, no. 8, pp. 45-51, 2000.

[26] O. N. Mryasov and A. J. Freeman, "Electronic band structure of indium tin oxide and criteria for transparent conducting behavior", Physical Review B (Condensed Matter and Materials Physics), vol. 64, no. 23, pp. 233111-1, 2001.

[27] P. Erhart, A. Klein, R. G. Egdell, and K. Albe, "Band structure of indium oxide: indirect versus direct band gap", Physical Review B (Condensed Matter), vol. 75, no. 15, pp. 153205-1, 2007.

[28] P. P. Edwards, A. Porch, M. O. Jones, D. V. Morgan, and R. M. Perks, "Basic Materials Physics of Transparent Conducting Oxides", Dalton Transactions, vol. 19, pp. 2995-3002, 2004.

[29] L. Gupta, A. Mansingh, and P. K. Srivastava, "Band gap narrowing and the band structure of tin-doped indium oxide films", Thin Solid Films, vol. 176, no. 1, pp. 33-44, 1989.

[30] G. Frank, L. Brock, and H. D. Bausen, "The solubilities of Sn in In_2O_3 and of In in SnO_2 crystals grown from Sn--In melts", Journal of Crystal Growth, vol. 36, no. 1, pp. 179-180, 1976.

[31] I. Isomaki, M. Hamalainen, W. Gierlotka, B. Onderka, and K. Fitzner, "Thermodynamic evaluation of the In-Sn-O system", Journal of Alloys and Compounds, vol. 422, no. 1-2, pp. 173-177, 2006.

[32] M. Mizuhashi, "Electrical properties of vacuum-deposited indium oxide and indium tin oxide films", Thin Solid Films, vol. 70, no. 1, pp. 91-100, 1980.

[33] P. Parent, H. Dexpert, G. Tourillon, and J. M. Grimal, "Structural study of tin-doped indium oxide thin films using x-ray absorption spectroscopy and x-ray diffraction. I Description of the indium site", Journal of the Electrochemical Society, vol. 139, no. 1, pp. 276-281, 1992.

[34] K. Ellmer and R. Mientus, "Carrier transport in polycrystalline ITO and ZnO : Al II: The influence of grain barriers and boundaries", Thin Solid Films, vol. 516, no. 17, pp. 5829-5835, 2008.

[35] K. Ellmer and R. Mientus, "Carrier transport in polycrystalline transparent conductive oxides: A comparative study of zinc oxide and indium oxide", Thin Solid Films, vol. 516, no. 14, pp. 4620-4627, 2008.

[36] X. Guo, W. Sigle, J. Fleig, and J. Maier, "Role of space charge in the grain boundary blocking effect in doped zirconia", Solid State Ionics, vol. 154-155, pp. 555-561, 2002.

[37] R. Gerhardt and A. S. Nowick, "Grain-boundary effect in ceria doped with trivalent cations. I. Electrical measurements", Journal of the American Ceramic Society, vol. 69, no. 9, pp. 641-646, 1986.

[38] J. E. Bauerle, "Study of solid electrolyte polarization by a complex admittance method", Journal of the Physics and Chemistry of Solids, vol. 30, no. 12, pp. 2657-2670, 1969.

[39] R. Gerhardt, A. S. Nowick, M. E. Mochel, and I. Dumler, "Grain-boundary effect in ceria doped with trivalent cations. II. Microstructure and microanalysis", Journal of the American Ceramic Society, vol. 69, no. 9, pp. 647-651, 1986.

[40] L. Jong-Sook and K. Doh-Yeon, "Space-charge concepts on grain boundary impedance of a high-purity yttria-stabilized tetragonal zirconia polycrystal", Journal of Materials Research, vol. 16, no. 9, pp. 2739-2751, 2001.

[41] H. Y. Lee and L. C. Burton, "Effect of grain size on the grain boundary resistance of undoped barium titanate ceramics", in Proceedings of the Eighth IEEE International Symposium on Applications of Ferroelectrics, New York, NY, USA, 1992, pp. 98-102.

[42] K. L. Chopra, Thin Film Phenomena. New York: McGraw-Hill Book Company, 1969.

[43] M. Batzill and U. Diebold, "The surface and materials science of tin oxide", Progress in Surface Science, vol. 79, no. 2-4, pp. 47-154, 2005.

[44] Y. Shigesato and D. C. Paine, "Study of the effect of Sn doping on the electronic transport properties of thin film indium oxide", Applied Physics Letters, vol. 62, no. 11, pp. 1268-70, 1993.

[45] H. Izumi, T. Ishihara, H. Yoshioka, and M. Motoyama, "Electrical properties of crystalline ITO films prepared at room temperature by pulsed laser deposition on plastic substrates", Thin Solid Films, vol. 411, no. 1, pp. 32-35, 2002.

[46] D. C. Paine, T. Whitson, D. Janiac, R. Beresford, C. O. Yang, and B. Lewis, "Study of low temperature crystallization of amorphous thin film indium-tin-oxide", Journal of Applied Physics, vol. 85, no. 12, pp. 8445-8450, 1999.

[47] B. G. Lewis and D. C. Paine, "Applications and Processing of Transparent Conducting Oxides", MRS Bulletin, pp. 22-27, 2000.

[48] F. O. Adurodija, L. Semple, and R. Bruning, "Crystallization process and electro-optical properties of In_2O_3 and ITO thin films", Journal of Materials Science, vol. 41, no. 21, pp. 7096-7102, 2006.

[49] D. R. Cairns and G. P. Crawford, "Electromechanical properties of transparent conducting substrates for flexible electronic displays", Proceedings of the IEEE, vol. 93, no. 8, pp. 1451-1458, 2005.

[50] H. Han, D. Adams, J. W. Mayer, and T. L. Alford, "Characterization of the physical and electrical properties of indium tin oxide on polyethylene napthalate", Journal of Applied Physics, vol. 98, no. 8, pp. 83705-1, 2005.

[51] S. Kundu, D. Bhattacharya, J. Ghosh, P. Das, and P. K. Biswas, "Ferromagnetism in transparent Mn(II)-doped indium tin oxide films prepared by sol-gel coating", Chemical Physics Letters, vol. 469, no. 4-6, pp. 313-317, 2009.

[52] J. Ba, D. F. Rohlfing, A. Feldhoff, T. Brezesinski, I. Djerdj, M. Wark, and M. Niederberger, "Nonaqueous synthesis of uniform indium tin oxide nanocrystals and their electrical conductivity in dependence of the tin oxide concentration", Chemistry of Materials, vol. 18, pp. 2848-2854, 2006.

[53] J. Ederth, P. Johnsson, G. A. Niklasson, A. Hoel, A. Hultaker, P. Heszler, C. G. Granqvist, A. R. v. Doorn, M. J. Jongerius, and D. Burgard, "Electrical and optical properties of

thin films consisting of tin-doped indium oxide nanoparticles", Physical Review B (Condensed Matter and Materials Physics), vol. 68, pp. 155410-1, 2003.

[54] C. Goebbert, R. Nonninger, M. A. Aegerter, and H. Schmidt, "Wet chemical deposition of ATO and ITO coatings using crystalline nanoparticles redispersable in solutions", Thin Solid Films, vol. 351, pp. 79-84, 1999.

[55] S. Reculusa and S. Ravaine, "Synthesis of colloidal crystals of controllable thickness through the Langmuir-Blodgett technique", Chemistry of Materials, vol. 15, pp. 598-605, 2003.

[56] S. Reculusa and S. Ravaine, "Colloidal photonic crystals obtained by the Langmuir-Blodgett technique", Applied Surface Science, vol. 246, pp. 409-414, 2005.

[57] C. B. Murray, S. Sun, W. Gaschler, H. Doyle, T. A. Betley, and C. R. Kagan, "Colloidal synthesis of nanocrystals and nanocrystal superlattices", IBM Journal of Research and Development, vol. 45, pp. 47-56, 2001.

[58] F. E. Kruis, H. Fissan, and A. Peled, "Synthesis of nanoparticles in the gas phase for electronic, optical and magnetic applications - a review", Journal of Aerosol Science, vol. 29, no. 5-6, pp. 511-535, 1998.

[59] W. R. Cannon, S. C. Danforth, J. H. Flint, J. S. Haggerty, and R. A. Marra, "Sinterable Ceramic Powders from Laser-Driven Reactions - 1. Process Description and Modeling", Journal of the American Ceramic Society, vol. 65, no. 7, pp. 324-330, 1982.

[60] A. L. Rogach, D. V. Talapin, and H. Weller, "Semiconductor Nanoparticles", in Colloids and Colloid Assemblies, F. Caruso, Ed., 2004, pp. 52-95.

[61] A. Eychmueller, "Structure and photophysics of semiconductor nanocrystals", Journal of Physical Chemistry B, vol. 104, no. 28, pp. 6514-6528, 2000.

[62] K. Osseo-Asare, "Microemulsion-Mediated Synthesis of Nanosize Oxide Materials", in Handbook of Microemulsion Science and Technology, P. Kumar and K. L. Mittal, Eds.: Marcel Dekker Inc., 1999, pp. 549-603.

[63] K. Osseo-Asare, "Preparation of nanoparticles: The microemulsion nanoreactor approach", in 2006 SME Annual Conference, Mar 26-29 2006, 2006, pp. 163-171.

[64] M. Niederberger, G. Garnweitner, J. Buha, J. Polleux, J. Ba, and N. Pinna, "Nonaqueous synthesis of metal oxide nanoparticles:Review and indium oxide as case study for the dependence of particle morphology on precursors and solvents", Journal of Sol-Gel Science and Technology, vol. 40, no. 2, pp. 259-266, 2006.

[65] K. Yura, K. C. Fredrikson, and E. Matijevic, "Preparation and properties of uniform colloidal indium compounds of different morphologies", Colloids and Surfaces, vol. 50, pp. 281-293, 1990.

[66] S.-G. Chen, C.-H. Li, W.-H. Xiong, L.-M. Liu, and H. Wang, "Preparation of indium-tin oxide (ITO) aciculae by a novel concentration-precipitation and post-calcination method", Materials Letters, vol. 59, pp. 1342-1346, 2005.

[67] G. Cao, Nanostructures & Nanomaterials: Synthesis, Properties & Applications, 1st ed. London: Imperial College Press, 2004.

[68] C. B. Murray, D. J. Norris, and M. G. Bawendi, "Synthesis and Characterization of Nearly Monodisperse CdE (E = S, Se, Te) Semiconductor Nanocrystallites", Journal of American Chemical Society, vol. 115, no. 19, pp. 8706-8715, 1993.

[69] C. d. M. Donegá, P. Liljeroth, and D. Vanmaekelbergh, "Physicochemical Evaluation of the Hot-Injection Method, a Synthesis Route for Monodisperse Nanocrystals", Small, vol. 1, no. 12, pp. 1152-1162, 2005.

[70] A. Narayanaswamy, H. Xu, N. Pradhan, M. Kim, and X. Peng, "Formation of Nearly Monodisperse In_2O_3 Nanodots and Oriented-Attached Nanoflowers: Hydrolysis and Alcoholysis vs Pyrolysis", Journal of American Chemical Society, vol. 128, pp. 10310-10319, 2006.

[71] X. Peng, Y. Chen, N. Jana, and A. Narayanaswamy, "Synthetic Control of Metal Oxide Nanocrystal Sizes and Shapes", United States patent number US2006/0211152 A1, 2006

[72] A. Narayanaswamy, H. Xu, N. Pradhan, and X. Peng, "Crystalline nanoflowers with different chemical compositions and physical properties grown by limited ligand protection", Angewandte Chemie - International Edition, vol. 45, pp. 5361-5364, 2006.

[73] S.-I. Choi, K. M. Nam, B. K. Park, W. S. Seo, and J. T. Park, "Preparation and optical properties of colloidal, monodisperse, and highly crystalline ITO nanoparticles", Chemistry of Materials, vol. 20, no. 8, pp. 2609-2611, 2008.

[74] E. Barsoukov and J. R. Macdonald, "Impedance Spectroscopy: Theory, Experiment, and Applications", 2nd Edition ed: Wiley-Interscience, 2005.

[75] R. A. Gerhardt, "Impedance Spectroscopy and Mobility Spectra", in Encyclopedia of Condensed Matter Physics, F. Bassani, G. L. Liedl, and P. Wyder, Eds. Oxford: Elsevier, 2005, pp. 350-363.

[76] N. J. Kidner, Z. J. Homrighaus, B. J. Ingram, T. O. Mason, and E. J. Garboczi, "Impedance/dielectric spectroscopy of electroceramics - Part 1: Evaluation of composite models for polycrystalline ceramics", Journal of Electroceramics, vol. 14, no. 3, pp. 283-91, 2005.

[77] N. J. Kidner, Z. J. Homrighaus, B. J. Ingram, T. O. Mason, and E. J. Garboczi, "Impedance/dielectric spectroscopy of electroceramics - Part 2: Shape effects and local properties of polycrystalline ceramics", Journal of Electroceramics, vol. 14, no. 3, pp. 293-301, 2005.

[78] J.-A. Jeong, J. Lee, H. Kim, H.-K. Kim, and S.-I. Na, "Ink-jet printed transparent electrode using nano-size indium tin oxide particles for organic photovoltaics", Solar Energy Materials & Solar Cells, vol. 94, no. 10, pp. 1840-1844, 2010.

[79] A. Reindl, M. Mahajeri, J. Hanft, and W. Peukert, "The influence of dispersing and stabilizing of indium tin oxide nanoparticles upon the characteristic properties of thin films", Thin Solid Films, vol. 517, no. 5, pp. 1624-1629, 2009.

[80] Y.-S. Cho, G.-R. Yi, J.-J. Hong, S. H. Jang, and S.-M. Yang, "Colloidal indium tin oxide nanoparticles for transparent and conductive films", Thin Solid Films, vol. 515, no. 4, pp. 1864-1871, 2006.

[81] M. A. Aegerter and N. Al-Dahoudi, "Wet-chemical processing of transparent and antiglare conducting ITO coating on plastic substrates", Journal of Sol-Gel Science and Technology, vol. 27, no. 1, pp. 81-89, May 2003.

[82] S.-J. Hong, J.-W. Kim, and J. I. Han, "Improvement of electrical properties of printed ITO thin films by heat-treatment conditions", Current Applied Physics, vol. 11, no. 1, pp. S202-S205, Jan 2011.

[83] A. Beaurain, D. Luxembourg, C. Dufour, V. Koncar, B. Capoen, and M. Bouazaoui, "Effects of annealing temperature and heat-treatment duration on electrical properties of sol-gel derived indium-tin-oxide thin films", Thin Solid Films, vol. 516, no. 12, pp. 4102-4106, Apr 30 2008.

[84] I. Gouskov, J. M. Saurel, C. Gril, M. Boustani, and A. Oemry, "Sprayed indium tin oxide layers: Optical parameters in the near-IR and evaluation of performance as a transparent antireflecting and conducting coating on GaSb or Ga1-xAlxSb for IR photodetection", Thin Solid Films, vol. 99, no. 4, pp. 365-369, 1983.

[85] M. M. Munir, H. Widiyandari, F. Iskandar, and K. Okuyama, "Patterned indium tin oxide nanofiber films and their electrical and optical performance", Nanotechnology, vol. 19, no. 37, p. 375601, Sep 17 2008.

[86] C. J. Capozzi and R. A. Gerhardt, "Novel percolation mechanism in PMMA matrix composites containing segregated ITO nanowire networks", Advanced Functional Materials, vol. 17, no. 14, pp. 2515-2521, 2007.

[87] S.-J. Hong, Y.-H. Kim, and J.-I. Han, "Development of Ultrafine Indium Tin Oxide (ITO) Nanoparticle for Ink-Jet Printing by Low-Temperature Synthetic Method", Nanotechnology, IEEE Transactions on, vol. 7, no. 2, pp. 172-176, 2008.

[88] K. Y. Kim and S. B. Park, "Preparation and property control of nano-sized indium tin oxide particle", Materials Chemistry and Physics, vol. 86, no. 1, pp. 210-221, Jul 15 2004.

[89] C. Goebbert, H. Bisht, N. Al-Dahoudi, R. Nonninger, M. A. Aegerter, and H. Schmidt, "Wet chemical deposition of crystalline, redispersable ATO and ITO nanoparticles", in 10th International Workshop on Glass and Ceramics, Hybrids and Nanocomposites from Gels. `SOL-GEL '99', 19-24 Sept. 1999, 2000, pp. 201-4.

[90] S. M. Joshi, G. W. Book, and R. A. Gerhardt, "A comparative study of the effect of annealing and plasma treatments on the microstructure and properties of colloidal ITO films and cold-sputtered ITO films", Thin Solid Films, vol. 520, no. 7, pp. 2723-2730, 2012.

[91] L. A. Robbins and R. W. Cusak, "Liquid-Liquid Extraction Operations and Equipment", in Perry's Chemical Engineers' Handbook (7th Edition), R. H. Perry and D. W. Green, Eds.: McGraw-Hill, 1997, pp. 15.1-15.47.

[92] R. E. Dinnebier, S. J. L. Billinge, A. L. Bail, I. Madsen, and L. M. D. Cranswick, Powder Diffraction: Theory and Practice, Royal Society of Chemistry, 2008.

[93] B. D. Cullity and S. R. Stock, Elements of X-Ray Diffraction, 3rd ed. Prentice-Hall Inc., 2001.

[94] "X-ray diffraction equipment (at MSE, Georgia Tech)", http://x-ray.gatech.edu/diffractometers.htm,

[95] A. Narayanaswamy, H. Xu, N. Pradhan, M. Kim, and X. Peng, "Formation of Nearly Monodisperse In_2O_3 Nanodots and Oriented-Attached Nanoflowers: Hydrolysis and Alcoholysis vs Pyrolysis", Journal of the American Chemical Society, vol. 128, pp. 10310-10319, 2006.

[96] S. M. Joshi and R. A. Gerhardt, "Effect of annealing atmosphere (Ar vs. air) and temperature on the electrical and optical properties of spin coated colloidal indium tin oxide films", Journal of Materials Science, vol. 48, no. 4, pp. 1465-1473, 2012.

[97] A. A. Bukharaev, N. V. Berdunov, D. V. Ovchinnikov, and K. M. Salikhov, "Three-Dimensional Probe and Surface Reconstruction for Atomic Force Microscopy Using a Deconvolution Algorithm", Scanning Microscopy, vol. 12, no. 1, pp. 225-234, 1998.

[98] D. P. Birnie, "Rational solvent selection strategies to combat striation formation during spin coating of thin films", Journal of Materials Research, vol. 16, no. 4, pp. 1145-1154, Apr 2001.

[99] "DXR Raman Microscope Thermo Scientific", http://www.thermoscientific.com/ecomm/servlet/productsdetail_11152_L10931_91245_11961705_-1,

[100] J. F. Moulder, W. F. Stickle, P. E. Sobol, and K. D. Bomben, "Handbook of x-ray photoelectron spectroscopy : a reference book of standard spectra for identification and interpretation of XPS data ", Eden Prairie, MN: Physical Electronics Division, Perkin-Elmer Corporation, 1995.

[101] "AIST:RIO-DB Spectral Database for Organic Compounds,SDBS", http://riodb01.ibase.aist.go.jp/sdbs/cgi-bin/cre_index.cgi,

[102] "Sigma-Aldrich.com", http://www.sigmaaldrich.com,

[103] "Plot Digitizer", http://plotdigitizer.sourceforge.net/,

[104] E. Smith and G. Dent, Modern Raman Spectroscopy: A Practical Approach. West Sussex, England: John Wiley & Sons, Ltd., 2006.

[105] "1-Octadecene (alpha-olefin C18)", http://www.chemicalland21.com/industrialchem/organic/1-OCTADECENE.htm,

[106] A. C. Ferrari and J. Robertson, "Interpretation of Raman spectra of disordered and amorphous carbon", Physical Review B, vol. 61, no. 20, pp. 14095-14107, 2000.

[107] J. Schwan, S. Ulrich, V. Batori, H. Ehrhardt, and S. R. P. Silva, "Raman spectroscopy on amorphous carbon films", Journal of Applied Physics, vol. 80, no. 1, pp. 440-447, 1996.

[108] G. Frank, E. Kauer, and H. Köstlin, "Transparent heat-reflecting coatings based on highly doped semiconductors", Thin Solid Films, vol. 77, no. 1-3, pp. 107-118, 1981.

[109] G. B. Gonzalez, J. S. Okasinski, T. O. Mason, T. Buslaps, and V. Honkimaki, "In situ studies on the kinetics of formation and crystal structure of $In_4Sn_3O_{12}$ using high-energy x-ray diffraction", Journal of Applied Physics, vol. 104, no. 4, pp. 043520-8, 2008.

[110] W. F. Wu and B. S. Chiou, "Mechanical properties of r.f. magnetron sputtered indium tin oxide films", Thin Solid Films, vol. 293, no. 1-2, pp. 244-250, 1997.

[111] CRC Handbook of Chemistry and Physics, 61st Edition, 61 ed. Boca Raton: CRC Press Inc., 1977.

[112] S. M. Joshi, G. W. Book, and R. A. Gerhardt, "Effect of Substrate Type on the Electrical and Optical Properties of Cold-sputtered Indium Tin Oxide Films as a function of Post-deposition Heat Treatment ", in 2010 MRS Spring Meeting, San Francisco CA, United States, 2010, pp. 1256-N16-55.

[113] "SPI Supplies® Brand Indium-Tin-Oxide (ITO) Coated Microscope Slides - Selection of Coating Resistivity - SPI Supplies.html", http://www.2spi.com/catalog/standards/ITO-coated-slides-resistivities5.html,

[114] M. Sahimi, Applications of Percolation Theory, Taylor & Francis, 1994.

[115] B. Gehl, A. Fromsdorf, V. Aleksandrovic, T. Schmidt, A. Pretorius, J. I. Flege, S. Bernstorff, A. Rosenauer, J. Falta, H. Weller, and M. Baumer, "Structural and chemical effects of plasma treatment on close-packed colloidal nanoparticle layers", Advanced Functional Materials, vol. 18, no. 16, pp. 2398-410, 2008.

[116] T. E. Sheridan, M. J. Goeckner, and J. Goree, "Pressure dependence of ionization efficiency in sputtering magnetrons", Applied Physics Letters, vol. 57, no. 20, pp. 2080-2, 1990.

[117] J. R. Macdonald, "Impedance Spectroscopy", Annals of Biomedical Engineering, vol. 20, pp. 289-305, 1992.

[118] "ZView™ for Windows", http://www.scribner.com/zview-for-windows.html,

[119] R. L. Muhlbauer, S. M. Joshi, and A. G. Rosario, "The Effect of Drying Technique on the Electrical Properties of Multiwalled Carbon Nanotube Thin Films Deposited on Paper Substrates with Different Pore Size", Journal of Materials Research (accepted), 2013.

[120] Y. Khatami, J. Kang, and K. Banerjee, "Graphene nanoribbon based negative resistance device for ultra-low voltage digital logic applications", Applied Physics Letters, vol. 102, no. 4, 2013.

[121] Y. Kim, J. H. Jang, S.-J. Park, S. Jesse, L. Donovan, A. Y. Borisevich, W. Lee, and S. V. Kalinin, "Local probing of electrochemically induced negative differential resistance in TiO2 memristive materials", Nanotechnology, vol. 24, no. 8, 2013.

[122] T. Tzung-Min and L. Yo-Sheng, "A 60-GHz double-balanced mixer with negative resistance compensation for direct up-conversion using 90-nm CMOS technology", Microwave and Optical Technology Letters, vol. 55, no. 3, pp. 536-43, 03/ 2013.

[123] L. Bakueva, G. Konstantatos, S. Musikhin, H. E. Ruda, and A. Shik, "Negative capacitance in polymer-nanocrystal composites", Applied Physics Letters, vol. 85, no. 16, pp. 3567-3569, 2004.

[124] W.-C. Chen, T.-C. Wen, and A. Gopalan, "Negative capacitance for polyaniline: an analysis via electrochemical impedance spectroscopy", Synthetic Metals, vol. 128, no. 2, pp. 179-189, 2002.

[125] E. Ehrenfreund, C. Lungenschmied, G. Dennler, H. Neugebauer, and N. S. Sariciftci, "Negative capacitance in organic semiconductor devices: Bipolar injection and charge recombination mechanism", Applied Physics Letters, vol. 91, no. 1, p. 012112, 2007.

[126] F. El Kamel, P. Gonon, F. Jomni, and B. Yangui, "Observation of negative capacitances in metal-insulator-metal devices based on a-BaTiO[sub 3]:H", Applied Physics Letters, vol. 93, no. 4, pp. 042904-3, 2008.

[127] M. Ershov, H. C. Liu, L. Li, M. Buchanan, Z. R. Wasilewski, and A. K. Jonscher, "Negative capacitance effect in semiconductor devices", IEEE Transactions on Electron Devices, vol. 45, no. 10, pp. 2196-2206, Oct 1998.

[128] Q. Ke, X. Lou, H. Yang, A. Kumar, K. Zeng, and J. Wang, "Negative capacitance induced by redistribution of oxygen vacancies in the fatigued BiFeO[sub 3]-based thin film", Applied Physics Letters, vol. 101, no. 2, pp. 022904-4, 2012.

[129] X. Wu, E. S. Yang, and H. L. Evans, "Negative Capacitance at Metal-Semiconductor Interfaces", Journal of Applied Physics, vol. 68, no. 6, pp. 2845-2848, Sep 1990.

[130] B. D. Bertram and R. A. Gerhardt, "Room temperature properties of electrical contacts to alumina composites containing silicon carbide whiskers", Journal of Applied Physics, vol. 105, no. 7, Apr 2009.

[131] G. B. Parravicini, A. Stella, M. C. Ungureanu, and R. Kofman, "Low-frequency negative capacitance effect in systems of metallic nanoparticles embedded in dielectric matrix", Applied Physics Letters, vol. 85, no. 2, pp. 302-304, 2004.

[132] R. van Zyl, W. Perold, R. Botha, S. A. S. Ieee, and S. A. S. Ieee, The Gunn-diode: Fundamentals and fabrication, 1998.

[133] E. Alekseev, D. Pavlidis, W. E. Sutton, E. Piner, and J. Redwing, "GaN-based Gunn diodes: Their frequency and power performance and experimental considerations", Ieice Transactions on Electronics, vol. E84C, no. 10, pp. 1462-1469, Oct 2001.

[134] A. Forster, M. I. Lepsa, D. Freundt, J. Stock, and S. Montanari, "Hot electron injector Gunn diode for advanced driver assistance systems", Applied Physics a-Materials Science & Processing, vol. 87, no. 3, pp. 545-558, Jun 2007.

[135] A. K. Jonscher, "The Physical Origin of Negative Capacitance", Journal of the Chemical Society-Faraday Transactions Ii, vol. 82, pp. 75-81, Jan 1986.

[136] C. G. Granqvist and A. Hultåker, "Transparent and conducting ITO films: new developments and applications", Thin Solid Films, vol. 411, no. 1, pp. 1-5, 2002.

[137] F. M. Smits, "Measurement of sheet resistivities with the four-point probe", Bell System Technical Journal, vol. 37, no. 3, pp. 711-718, 1958.

[138] L. G. Valdes, "Measurements of Sheet Resistivity with the Four-Point Probe", Proceedings of the IRE, vol. 42, pp. 420-427, 1954.

[139] S. Graham, Oral communication at School of Materials Science and Engineering, Georgia Institute of Technology, 2013.

[140] K.-H. Choi, J.-A. Jeong, J.-W. Kang, D.-G. Kim, J. K. Kim, S.-I. Na, D.-Y. Kim, S.-S. Kim, and H.-K. Kim, "Characteristics of flexible indium tin oxide electrode grown by continuous roll-to-roll sputtering process for flexible organic solar cells", Solar Energy Materials and Solar Cells, vol. 93, no. 8, pp. 1248-1255, 2009.

[141] C. Miller, "Techniques for Reducing Resistance Measurement Uncertainty: DC Current Reversals vs. Classic Offset Compensation (white paper)", Keithley Instruments, Inc., Cleveland OH 2000.

[142] R. B. H. Tahar, T. Ban, Y. Ohya, and Y. Takahashi, "Tin doped indium oxide thin films: electrical properties", Journal of Applied Physics, vol. 83, no. 5, pp. 2631-2645, 1998.

[143] H. Morikawa and M. Fujita, "Crystallization and electrical property change on the annealing of amorphous indium-oxide and indium-tin-oxide thin films", Thin Solid Films, vol. 359, no. 1, pp. 61-67, 2000.